

UC Irvine

UC Irvine Electronic Theses and Dissertations

Title

Multi-Tone Continuous-Wave Lidar

Permalink

<https://escholarship.org/uc/item/5km717gh>

Author

Bayer, Mustafa Mert

Publication Date

2022

Copyright Information

This work is made available under the terms of a Creative Commons Attribution License, available at <https://creativecommons.org/licenses/by/4.0/>

Peer reviewed|Thesis/dissertation

UNIVERSITY OF CALIFORNIA,
IRVINE

Multi-Tone Continuous-Wave Lidar

DISSERTATION

submitted in partial satisfaction of the requirements
for the degree of

DOCTOR OF PHILOSOPHY

in Electrical Engineering

by

Mustafa Mert Bayer

Dissertation Committee:
Professor Ozdal Boyraz, Chair
Professor Payam Heydari
Assistant Professor Hamidreza Aghasi

2022

A portion of Chapter 3 © 2019 IEEE & 2020 OSA

A portion of Chapter 4 © 2021 OSA

A portion of Chapter 5 © 2022 OSA & SPIE

All other materials © 2022 Mustafa Mert Bayer

DEDICATION

It is with genuine gratitude and warm regard that I dedicate my dissertation

to

my mother Feriha Bayer, my father Sefa Bayer, my brother Murat Bayer, and my sister Merve Bayer

for

their limitless love and constant support throughout my journey.

TABLE OF CONTENTS

DEDICATION.....	ii
TABLE OF CONTENTS	iii
LIST OF FIGURES.....	vi
LIST OF TABLES	viii
LIST OF ABBREVIATIONS.....	ix
ACKNOWLEDGEMENTS.....	ix
VITA	x
ABSTRACT OF THE DISSERTATION.....	xiii
Chapter 1	1
1. INTRODUCTION.....	2
1.1. Background.....	2
1.2. Dissertation Organization	4
Chapter 2	6
2. LIDAR TECHNOLOGIES.....	7
2.1. Overview of Lidar Operation.....	7
2.1.1. General operating principle of lidars	7
2.1.2. Eye safety and lidar wavelength selection	10
2.1.3. Types of lidars.....	11
2.1.4. Important lidar parameters.....	13
2.2. Pulsed Time of Flight Lidar	15
2.2.1. Working principle.....	15
2.2.2. Lidar parameters.....	16
2.2.3. Challenges.....	19
2.3. Amplitude-Modulated Continuous Wave Lidar.....	20
2.3.1. Working principle.....	20
2.3.2. Lidar parameters.....	21
2.3.3. Challenges.....	22
2.4. Frequency-Modulated Continuous Wave Lidar.....	23
2.4.1. Working principle.....	23
2.4.2. Lidar parameters.....	25
2.4.3. Challenges.....	27

Chapter 3	28
3. AMPLITUDE-BASED MULTI-TONE CONTINUOUS-WAVE LIDAR.....	29
3.1. Motivation.....	29
3.2. Working Principle	29
3.2.1. Concept.....	29
3.2.2. Theoretical model of a static target	30
3.2.3. Theoretical model of a dynamic target	33
3.3. Numerical Verification	35
3.3.1. Simulation of the numerical model.....	35
3.3.2. Scattering loss and unambiguous range characterization.....	36
3.4. Experimental Verification.....	38
3.4.1. Methodology	38
3.4.2. Static target results.....	40
3.4.3. Dynamic target results	42
3.5. Analysis	45
3.5.1. Lidar parameters.....	45
3.5.2. Challenges.....	49
Chapter 4	51
4. PHASE-ENHANCED AMPLITUDE-BASED MTCW LIDAR.....	52
4.1. Motivation.....	52
4.2. Working Principle	52
4.2.1. Theoretical model.....	52
4.2.2. Triangulation algorithm	57
4.3. Numerical Verification	58
4.3.1. Simulation parameters	58
4.3.2. Simulation results	59
4.4. Experimental Results.....	64
4.4.1. Dynamic target results	64
4.5. Analysis	66
4.5.1. Lidar parameters.....	66
4.5.2. Challenges.....	66
Chapter 5	68
5. PHASE-BASED MULTI-TONE CONTINUOUS-WAVE LIDAR.....	69
5.1. Motivation.....	69
5.2. Working Principle	70

5.2.1. Concept.....	70
5.2.2. Theoretical model of a static target	71
5.2.3. Theoretical model of a dynamic target	74
5.2.4. Post-processing.....	75
5.3. Numerical Verification	77
5.3.1. Simulation parameters	77
5.3.2. Simulation results	78
5.4. Experimental Verification.....	79
5.4.1. Methodology	79
5.4.2. Static target results.....	82
5.4.3. Dynamic target results	84
5.5. Quasi-CW integration.....	86
5.5.1. Concept.....	86
5.5.2. Experimental setup	88
5.5.3. Experimental results	89
5.6. Analysis	91
5.6.1. Lidar parameters.....	91
5.6.2. Challenges.....	95
SUMMARY AND DISCUSSION.....	96
BIBLIOGRAPHY.....	99

LIST OF FIGURES

Fig. 1 General operating principle of lidar systems.....	8
Fig. 2 The maximum permissible exposure (MPE) curves with respect to the laser wavelengths.....	11
Fig. 3 Types of lidars.....	12
Fig. 4 Range precision vs. measurement range for pulsed, AMCW, and FMCW lidars after 1990.....	14
Fig. 5 Working principle of the pulsed time of flight lidar.....	15
Fig. 6 Working principle of the amplitude-modulated continuous-wave lidar.....	20
Fig. 7 Working principle of the frequency-modulated continuous-wave lidar.....	23
Fig. 8 Working principle and schematic of AB-MTCW configuration.....	30
Fig. 9 Theoretical model parameters on the AB-MTCW configuration.....	31
Fig. 10 Simulation results of the AB-MTCW lidar.....	36
Fig. 11 Simulation of the impact of the loss in the echo signal.....	37
Fig. 12 The experimental setup used for AB-MTCW and PToF lidar ranging, and simultaneous AB-MTCW lidar ranging and velocimetry.....	38
Fig. 13 Experimental configurations of the PToF technique and AB-MTCW lidar.....	39
Fig. 14 Static target ranging results with PToF and AB-MTCW lidars.....	41
Fig. 15 Velocimetry results by using AB-MTCW lidar.....	43
Fig. 16 Simultaneous ranging and velocimetry results while the target is moving with $v=8\text{cm/s}$	44
Fig. 17 Simulation results showing the impact of SNR in AB-MTCW lidar.....	48
Fig. 18 Example of the triangulation matrix.....	58
Fig. 19 RF spectrum of the simulation result of PE-MTCW technique.....	60
Fig. 20 Measured distance by each Doppler-shifted frequency.....	62
Fig. 21 Result of the triangulation algorithm based on simulation results.....	63
Fig. 22 Measured resultant RF spectrum of the target moving with $\sim 8\text{cm/s}$	64
Fig. 23 Experimental triangulation result of the PE-MTCW lidar.....	65
Fig. 24 Working principle of the Phase-Based Multi-Tone Continuous Wave lidar.....	70

Fig. 25 Theoretical model parameters on the PB-MTCW configuration.....	71
Fig. 26 Block diagram representing the post-processing after data acquisition.	76
Fig. 27 Simulation results of stationary target ranging at $L_m = 2m$	78
Fig. 28 Numerical simulation results demonstrate the capability of the triangulation algorithm with 6 modulation tones.	78
Fig. 29 Schematic representation of the experimental test bench for PB-MTCW lidar.	79
Fig. 30 Stationary target ranging results with high and low coherence lasers via PB-MTCW technique.	82
Fig. 31 Complete stationary target ranging results with high and low coherence lasers via the PB-MTCW technique.....	83
Fig. 32 Dynamic target ranging results with high and low coherence lasers.	85
Fig. 33 Concept of multi-tone quasi-CW pulsation.....	87
Fig. 34 Experimental setup for testing the quasi-CW PB-MTCW lidar for long-range applications.....	88
Fig. 35 Experimental results for the long-range measurements with quasi-CW integration.....	90
Fig. 36 Numerical simulation results of the signal-to-noise ratio of a single modulation frequency with respect to the echo signal attenuation.	94

LIST OF TABLES

Table 1 Resultant frequencies and their corresponding amplitude, phase, and L_0 equations.....	55
Table 2 Ranging results of a stationary target with high and low coherence lasers.	83
Table 3 Simultaneous ranging and velocimetry results of a dynamic target with high and low coherence lasers.....	86

LIST OF ABBREVIATIONS

Acusto Optic Modulator	AOM
Amplified Spontaneous Emission	ASE
Amplitude-Based Multi-Tone Continuous Wave	AB-MTCW
Amplitude-Modulated Continuous Wave	AMCW
Analog-to-Digital Converter	ADC
Avalanche Photodiode	APD
Bandwidth	BW
Beamsplitter	BS
Collimator	CL
Continuous Wave	CW
Data Acquisition	DAQ
Dual-sideband Modulation	DSB
Electric Field	E-Field
Electro-optic Modulator	EOM
Erbium-Doped Fiber Amplifier	EDFA
Fast Fourier Transform	FFT
Frequency-Modulated Continuous Wave	FMCW
Indium Galium Arsenide	InGaAs
Infrared	IR
Intermediate Frequency	IF
Isolator	ISO
Light detection and ranging	Lidar
Local Oscillator	LO
Mach-Zehnder Modulator	MZM
Maximum Permissible Exposure	MPE
Mode-locked	ML
Multi-Tone Continuous Wave	MTCW
Noise-equivalent-power	NEP
Oscilloscope	OSC
Phase-Based Multi-Tone Continuous Wave	PB-MTCW
Phase-Enhanced Amplitude-Based Multi-Tone Continuous Wave	PE-MTCW
Phase-locked Loop	PLL
Photodetector	PD
Photonic Doppler Velocimetry	PDV
Polarization Controller	PC
Polarization Maintaining Fiber	PMF
Pulsed Time of Flight	PToF
Quasi Continuous Wave	quasi-CW
Radio Frequency	RF
Receiver	Rx
R-squared	R^2
Short-time Fourier Transform	STFT
Signal-to-noise Ratio	SNR
Silicon	Si
Single Mode Fiber	SMF
Single-sideband Modulation	SSB
Spur-free Dynamic Range	SFDR
Time of Flight	ToF
Transmitter	Tx

ACKNOWLEDGEMENTS

I would like to express my deepest gratitude to my mentor, advisor, and supervisor Professor Ozdal Boyraz. I could not have undertaken this journey and developed the Multi-Tone Continuous Wave technology without his guidance, mentorship, and constant support. Moreover, I would like to thank my dissertation committee members, Professor Payam Heydari and Professor Hamidreza Aghasi for their invaluable opinion and suggestions for my research. I am extremely grateful to Dr. Jose Velazco, founder of Chascii, for his guidance and contributions to the projects during the development of our lidar system. I would like to extend my sincere thanks to Professor Ali Serpenguzel, Koc University, for his support, kindness, and generous help throughout my Master of Science. Furthermore, words can not express my gratitude to my former colleague Dr. Rasul Torun, who always aided and guided me when I needed his support the most. I would like to also acknowledge the partial support of this thesis by the Office of Naval Research under grant number N00014-18-1-2845 and the National Science Foundation under grant number PAWR-5582469.

I would like to express my special thanks to my teammates, George N. Guentchev, Xun Li, and Ataberk Atalar, for creating a family-like working environment during this journey. I am also genuinely grateful for having fascinating colleagues such as Dr. Parinaz Sadri-Moshkenani, Dr. Imam-uz Zaman, Mohammad Wahiduzzaman Khan, Md Shafiqul Islam, and Ceren Babayigit who helped me in my research and personal development. Thanks should also go to my sincere friends Ahmet Aksakal, Abdullah Sahin, Mustafa Onur Onen, Esra Ozturk, Melissa Akkaya, Nilab Ismailoglu, Kutay Pekcan, Fazilet Cilli, Francisco Cerda, Matt Brand, Sam Reifsnnyder, Francesca Cecconi, Rami Hadidi, and Sharja Khan for their company, which composed unforgettable memories during this adventure.

Finally, this endeavor would not have been possible without the limitless love and continuous support of my parents. I'm also extremely grateful for having two talented siblings, who aided me whenever I asked for their support. Lastly, I offer my regards to all of those who supported me indirectly in any respect during the completion of this dissertation.

VITA

Mustafa Mert BAYER

EDUCATION

- 2017 – 2022 **University of California, Irvine, CA** - Henry Samueli School of Engineering
Ph.D. Major: Electrical Engineering and Computer Science
- 2015 – 2017 **Koc University, Istanbul, Turkey** - Grad. School of Sciences and Engineering.
MSc Major: Optoelectronics and Photonics Engineering
- 2010 – 2015 **Koc University, Istanbul, Turkey** - College of Science & College of Engineering.
Major: Physics
Double Major: Electrical and Electronics Engineering
Tracks: Optics and Electromagnetism Track

PATENTS

1. M. M. Bayer and O. Boyraz, "Multi-tone continuous wave detection and ranging," US patent US20210382164A1 (Dec. 9, 2021).

PUBLICATIONS

1. M. M. Bayer, X. Li, G. N. Guentchev, R. Torun, J. E. Velazco, and O. Boyraz, "Single-shot ranging and velocimetry with a CW lidar far beyond the coherence length of the CW laser," *Opt. Express* **29**, 42343–42354 (2021).
2. M. M. Bayer and O. Boyraz, "Ranging and velocimetry measurements by phase-based MTCW lidar," *Opt. Express* **29**, 13552–13562 (2021).
3. M. M. Bayer, R. Torun, X. Li, J. E. Velazco, and O. Boyraz, "Simultaneous ranging and velocimetry with multi-tone continuous wave lidar," *Opt. Express* **28**, 17241–17252 (2020).
4. N. Yavuz, M. M. Bayer, H. O. Çirkinoğlu, A. Serpengüzel, T. Le Phu, A. Giakoumaki, V. Bharadwaj, R. Ramponi, and S. M. Eaton, "Laser-Inscribed Diamond Waveguide Resonantly Coupled to Diamond Microsphere," *Molecules* **25**, 2698 (2020).
5. R. Torun, M. M. Bayer, I. U. Zaman, J. E. Velazco, and O. Boyraz, "Realization of Multitone Continuous Wave Lidar," *IEEE Photonics J.* **11**, 1–10 (2019).
6. H. O. Çirkinoğlu, M. M. Bayer, A. Serpengüzel, S. Rampini, B. Sotillo, V. Bharadwaj, R. Ramponi, and S. M. Eaton, "Femtosecond laser written diamond waveguide excitation of the whispering gallery modes in a silicon microsphere," *Opt. Mat.* **92**, 418–424 (2019).
7. M. M. Bayer, H. O. Çirkinoğlu, and A. Serpengüzel, "Observation of Whispering-Gallery Modes in a Diamond Microsphere," *IEEE Photon. Tech. L.* **30**, 3–6 (2018).
8. H. O. Çirkinoğlu, M. M. Bayer, U. S. Gökay, A. Serpengüzel, B. Sotillo, V. Bharadwaj, R. Ramponi, and S. M. Eaton, "Silicon microsphere whispering gallery modes excited by femtosecond-laser-inscribed glass waveguides," *Appl. Opt.* **57**, 3687–3692 (2018).
9. M. H. Humayun, S. S. S. Bukhari, M. Zakwan, M. M. Bayer, U. S. Gökay, A. Serpengüzel, K. Taira, E. Omura, and J. Nakata, "Spatial intensity profiling of elastic and inelastic scattering in isotropic and anisotropic liquids by immersion of a spherical silicon photocell," *Appl. Opt.* **56**, 9384–9389 (2017).
10. O. M. Öztürk, M. M. Bayer, M. S. Anwar, M. Zakwan, and A. Serpengüzel, "Spectroscopy of a Nd:YVO4 diode pumped solid state laser," *Microw. Opt. Techn. Let.* **59**, 1636–1639 (2017).

CONFERENCES

1. M. M. Bayer, X. Li, A. Atalar, and O. Boyraz, "Phase-Based Multi-Tone CW Lidar: A Technique for Ranging Beyond the Coherence Length of the CW Laser," in *Conference on Lasers and Electro-Optics (CLEO)* (2022), p. ATu4M.1.
2. M. M. Bayer, A. Atalar, X. Li, and O. Boyraz, "Photonics PNT Based on Multi-Tone Continuous Wave Ranging," in *Conference on Lasers and Electro-Optics, (CLEO)* (2022), p. JTh3A.57.
3. X. Li, M. M. Bayer, G. N. Guentchev, and O. Boyraz, "Design and Prototype of Auto-Track Long-Range Free-Space Optical Communication," in *2022 Optical Fiber Communications Conference and Exhibition (OFC)* (2022), pp. 1–3.
4. M. M. Bayer, G. N. Guentchev, X. Li, J. E. Velazco, and O. Boyraz "Enhancing the multi-tone continuous-wave lidar with phase detection", Proc. SPIE **11828**, 1182807 (2021).
5. G. N. Guentchev, M. M. Bayer, X. Li, and O. Boyraz "Mechanical design and thermal analysis of a 12U CubeSat MTCW lidar-based optical measurement system for littoral ocean dynamics", Proc. SPIE **11832**, 118320B (2021).
6. M. M. Bayer, R. Torun, I. U. Zaman, and O. Boyraz, "Multi-Tone Continuous Wave Lidar in Simultaneous Ranging and Velocimetry," in *Conference on Lasers and Electro-Optics (CLEO)* (2020), p. SM1O.6.
7. M. M. Bayer, R. Torun, I. U. Zaman, and O. Boyraz, "A Basic Approach for Speed Profiling of Alternating Targets with Photonic Doppler Velocimetry," in *Conference on Lasers and Electro-Optics (CLEO)* (2019), p. AW4K.4.
8. P. Sadri-Moshkenani, M. W. Khan, M. M. Bayer, M. S. Islam, E. Montoya, I. Krivortov, M. Nilsson, N. Bagherzadeh, and O. Boyraz, "Effect of Tantalum and MgO adhesion layers on plasmonic nanostructures," Proc. SPIE **11089**, 1108916 (2019).
9. R. Torun, M. M. Bayer, I. U. Zaman, and O. Boyraz, "Multi-tone modulated continuous-wave lidar," Proc. SPIE **10925**, 109250V (2019).
10. O. Boyraz, M. M. Bayer, R. Torun, and I. Zaman, "Multi Tone Continuous Wave Lidar," in *IEEE Photonics Society Summer Topical Meeting Series (SUM)* (2019), pp. 1–2.
11. S. Sultan Shah Bukhari, M. R. Chaudhry, M. M. Bayer, and A. Serpengüzel, "Elastic Scattering from a Sapphire Microsphere in the THz Region," in *Frontiers in Optics 2016, (FiO)(2016)*, p. JTh2A.180.
12. M. Zakwan, M. M. Bayer, M. S. Anwar, U. S. Gökay, and A. Serpengüzel, "Mid-infrared elastic scattering from germanium microspheres," in *International Conference on Transparent Optical Networks 2016, (ICTON)* (2016), pp. 1–1.

EXPERIENCE

2018 – 2020

UC Irvine, CA, Teaching Assistant

EECS 170A – Electronics I Laboratory session TA,
EECS 70A – Circuits Laboratory session and Discussion session TA,
ECPS 204 – Embedded System Software Discussion TA

2017 – 2022

UC Irvine, CA Advance Photonic Devices and Systems Laboratory Research Assistant

Research on continuous-wave and quasi-continuous wave Lidar systems, photonic Doppler velocimetry, and ranging applications for satellite and airborne systems, and GPS systems. System-level engineering in free-space optical communication, optical communication links, and networks. Numerical modeling of ultrafast lasers, solitons, nonlinear passive mode-locking techniques, optical amplification

methods, and fiber lasers. In lab hands-on experience with optical components for testing, evaluation, and design of optical systems including lasers, detectors, RF devices, and passive optics.

2016 – 2017

**Koc University Microphotonics Research Lab (KUMRL), Istanbul-Turkey
Research Assistant**

Research on the indication of nitrogen-vacancy centers in natural and synthetic diamonds. Experimenting on Optical microcavities, and spherical resonators of various materials such as diamond, silicon, and ruby.

2013 – 2017

Koc University, Istanbul - Turkey, Teaching Assistant

PHYS 206 - Modern Physics Laboratory session TA

PHYS 405/505 - Experimental Physics Laboratory session TA.

2014

TÜV NORD, Istanbul - Turkey

Industrial summer practice intern

Solar panel and wind turbine inspections and certifications according to international standards in the Industrial Services department.

2013

FORD OTOSAN, Kocaeli - Turkey

Industrial summer practice intern

Control systems in the automotive industry. Designing logic circuits using Logi.Cad software for relevant systems.

PROJECTS

2021 – 2022

ARA Wireless Living Lab for Smart and Connected Rural Communities funded by NSF PAWR-5582469.

Role: System-level engineering by leading the team members to realize the integration of all subunits. Design of the telescope unit and optical backbone of the free-space optical communication link and design and integration of the beacon signal. Characterization of the system requirements and optical parameters. Integration of motor unit with the optical telescope unit.

2018 – 2022

CubeSat based Optical Measurement System for Littoral Ocean Dynamics funded by Office of Naval Research with Award # N00014-18-1-2845

Role: System-level engineering by leading the team members to realize the integration of all subunits. Design of optical transmission and reception units for the Lidar system. Integration of the Lidar to the spacecraft. Optimization of design parameters, scanning modes, and mission metrics.

LINKS

Goole Scholar:

scholar.google.com.tr/citations?user=p-DN1psAAAAJ&hl=en&authuser=1

LinkedIn:

linkedin.com/in/mert-bayer-aa631359

ORCID:

orcid.org/my-orcid?orcid=0000-0002-6390-3544

Scopus:

www.scopus.com/authid/detail.uri?authorId=57193835561

ABSTRACT OF THE DISSERTATION

Multi-Tone Continuous Wave Lidar
by
Mustafa Mert Bayer
Doctor of Philosophy in Electrical Engineering
University of California, Irvine, 2022
Professor Ozdal Boyraz, Chair

Over the past years, light detection and ranging (lidar) systems have been vastly investigated and commercialized for various platforms such as self-driving cars, unmanned aerial vehicles, and spacecraft. A wide range of lidar applications such as topographical imaging, remote object sensing, oceanographic and atmospheric surveillance, navigation, and driver assistance mostly relies on range measurements. The majority of the lidar instrumentation used in these applications operates in a pulsed time-of-flight (PToF) mode to acquire the range information by comparing the delay between the ejection time of an optical impulse and the detection time of the pulse in flight. Inherently, this conventional approach lacks the capability of simultaneous velocimetry and fine-ranging resolution requires high-speed detection electronics. Moreover, continuous-wave (CW) laser-based lidar systems are being investigated. CW lidars are desired because they use coherent detection techniques that provide a higher signal-to-noise ratio (SNR) than the direct detection method used in PToF. Up to date, various CW lidar techniques such as amplitude-modulated continuous wave (AMCW) lidars, frequency modulated continuous wave (FMCW) lidars, and phase-based ranging have been demonstrated. Hence, to perform the measurements and to extract the precise distance of the target, the AMCW method requires sweeping of amplitude and phase, while the FMCW technique requires frequency sweeping.

As an alternative to the existing lidar technologies, Multi-Tone Continuous-Wave (MTCW) lidar is developed, which eliminates the necessity of any form of phase, frequency, or amplitude sweeping in a CW lidar configuration. In the MTCW approach, multiple fixed phase-locked radio frequencies (RF) are utilized to modulate a CW laser by using Mach-Zehnder modulators. A portion of the light is kept as a local oscillator to realize coherent detection to enhance the SNR. The modulated beam is transmitted to free space and the echo signal is collected by the receiver of the lidar. Each sideband accumulates a different phase

based on the frequency and target distance. It is possible to compute the target distance by either converting the phase differences into RF tone power variations or by exploiting the phase and frequency differences between RF tones. Three versions of the MTCW lidar are constructed based on the utilization of tone amplitudes or phases, namely amplitude-base MTCW (AB-MTCW), phase-enhanced amplitude-based MTCW (PE-MTCW), and phase-based MTCW (PB-MTCW) lidars. Theoretical modeling, numerical simulations, and experimental verifications are presented for each technique. For AB-MTCW lidar, $<1\text{cm}$ ranging precision with 0.8cm/s velocimetry resolution is demonstrated. Furthermore, the PE-MTCW approach is matured to provide a solution to fast targets ranging via AB-MTCW lidar. Finally, the PB-MTCW methodology is developed that can perform the ranging of dynamic or static targets at a range that is $\times 500$ larger than the coherence length of the CW laser with a $<1\text{cm}$ ranging resolution and precision. It is also shown that, by integrating the modulated beam with a quasi-CW pulsation, it is possible to perform ranging beyond the unambiguous range of the CW lidar, as well. Therefore, the PB-MTCW lidar can be considered an alternative long-distance remote sensing device for aerial or space-based altimetry applications.

Chapter 1

Introduction

1. INTRODUCTION

1.1. Background

Digital cameras, radars, and lidars (light detection and ranging) are considered to be three enabling technologies in autonomous terrestrial and aerial vehicles [1,2]. Lidars, the optical version of radars, operate by generating a point cloud of the environment based on the information encoded in the echoed light. The emerging need for high-resolution ranging and imaging in the areas such as terrestrial altimetry fueled the interest in lidar systems [3,4]. So far lidars have been used in military applications [5] and atmospheric sciences [6] to detect remote objects, measure distances [7], create topographical images [4], detect aerosol particles [8,9], and measure ozone layers [10,11], etc. In recent years, with the advent of self-driving cars and unmanned aerial vehicles (UAV), lidar became a topic of interest once again for proximity sensing and collision prevention [12–17].

Lidars perform ranging by either measuring the time-of-flight (ToF) of a laser pulse traveling from a laser source to a target and back to a photodetector, or by generating the so-called radio frequency (RF) beat tones through the interference of reference light and the reflected light from a target by using continuous wave (CW) laser and a coherent detection system [18–24]. These recent research activities focus on receiver architecture [25], and signal processing techniques [26,27] to achieve more robust, accurate, and sensitive measurements in a longer range. To achieve accurate timing, ToF lidars require short pulse generation and high temporal resolution, hence fast electronics are necessary. Therefore, several consecutive measurements are mandatory to utilize Monte Carlo methods to minimize the error in timing. Additionally, the precision of this approach degrades with distance and it also inherently lacks the ability to detect velocity and direction information of moving targets [20].

Recently, applications employing continuous wave (CW) lasers as amplitude modulated continuous wave (AMCW), and frequency modulated continuous wave (FMCW) lidars were demonstrated [19,28,29]. AMCW lidar systems modulate the intensity of the light while keeping the frequency constant. Depending on the desired range precision, AMCW lidars require high-speed radio frequency electronics to modulate

the light intensity. On the receiver hand, this requirement can be mitigated via demodulation or superheterodyne receivers that convert the high-frequency tones to baseband signals. The range information is either obtained by convolving the local oscillator with the time-delayed return signal as in phase shift lidars or electronic heterodyne detection to generate a beat note proportional to the target distance as in linearly chirped lidars [19,20]. By employing AMCW lidars and precision improvements techniques such as multiple signal classification and harmonic distortion cancellation, <5mm precision is reported for distances <12m [30–32].

The FMCW lidars are employing frequency sweeping of light sources such as tunable lasers or frequency modulated CW lasers with a chirped RF signal. The return signal is detected via optical heterodyning by a slow square-law detector, therefore the generated beating frequency can be recorded by slower electronics [20]. In FMCW lidars, since the same target is measured with several frequencies, the results become more robust and accurate [19]. Also, they have the potential of detecting the speed and direction information of the target simultaneously [33,34]. The FMCW lidar systems achieve sub-mm resolutions for short-range (<10m) detection, while utilizing wide-band frequency tuning via swept sources [35–37]. The resolution degrades to ~5cm at medium range (~100m) detection where at a bandwidth that is limited to 5GHz [38]. However, in the practical domain, frequency stability of the laser source and technical challenges that limit the sweeping frequency range up to a few GHz, hence range resolution to cm level, and mitigate the reliability of frequency chirped lidars [39,40]. Very recently, frequency combs are utilized to achieve more than THz bandwidth, hence demonstrating μm resolutions in a short-range measurement distance [41].

On the other hand, some frequency domain lidars previously employed multiple-wavelength techniques such as continuous time-of-flight measurements [42], multi-wavelength super-heterodyning [43,44], and multi-frequency demodulation via CMOS photonic mixer devices [45], which were used for short-range and high precision imaging and ranging. However, it is important to note that these efforts are mainly targeted for short-range measurements in applications such as Microsoft Kinect.

In addition to AMCW and FMCW, phase-based ranging is also a remarkable technique for absolute metrology systems [46]. However, the implementation of such a system is troublesome due to the requirement of multiple detectors or detector arrays, as well as heterodyne detection of two arms with different frequencies. Also, the detection in such applications requires either phase detectors or elaborates phase extraction techniques during post-processing. The lack of direct velocity measurement is another drawback of such techniques. Therefore, a less burdensome system is necessary with high-resolution capability for longer ranges that can also provide velocity information simultaneously.

1.2. Dissertation Organization

To address the challenges of sweep requirements, coherence length limits, unambiguous range constraints, the capability of simultaneous ranging and velocimetry, and achieving high-resolution results in long-range applications, three different lidar methodologies are presented in this dissertation along with the summary of the available lidar technologies, which is presented in Chapter 2.

The Multi-Tone Continuous Wave (MTCW) lidar technique is proposed and demonstrated that uses a single CW laser modulated by multiple RF tones and coherent detection for range measurements without employing any form of sweeping [47–50]. In the first technique, the range is acquired by converting the time delay between the backscattered light and the local oscillator into tone power variations via heterodyne detection. Since the detected RF tones exhibit a sinusoidal pattern based on their individually accumulated phases, and the frequency of this sinusoidal pattern is inversely proportional to the target distance, an accurate range measurement is possible from the recognition of the pattern encoded on RF tone powers. This method is named Amplitude-Based Multi-Tone Continuous Wave (AB-MTCW) lidar. The theoretical model and experimental demonstration of simultaneous ranging and velocimetry are performed. A $\sim 0.75\text{cm}$ measured distance deviation (set by the temporal resolution of the measurement system) between MTCW and PToF techniques and $\pm 0.8\text{cm/s}$ velocimetry accuracy is achieved by using the AB-MTCW lidar. The details about the AB-MTCW lidar are presented in Chapter 3.

The second technique, which is called the Phase-Enhanced Amplitude-Based Multi-Tone Continuous-Wave (PE-MTCW) lidar, is a complementary phase detection algorithm that enhances the capabilities of the AB-MTCW lidar for single-shot simultaneous ranging and velocimetry measurements. Here, the range information of the target is stored in the phases of the individual RF tones. It is shown that the phase of the Doppler-shifted RF tones and the amount of the induced Doppler frequency shift can be used to extract the range and velocity information, simultaneously. To prove the concept, a case study on simultaneous ranging and velocimetry of a fast dynamic target is performed via numerical simulations. A $<\pm 1\text{cm}$ resolution in the range is demonstrated, which is limited by the temporal resolution of the detection system. Also, a 0.4cm/s speed resolution that is limited by the linewidth of the laser and frequency resolution of the detection system is achievable by using PE-MTCW lidar. Furthermore, experimental results are presented to demonstrate the capability of the proposed methodology as explained in Chapter 4.

The final technique is a modified version of the AB-MTCW lidar. It is hypothesized that if a fraction of the source laser is used before encoding the RF tones at the amplitude modulator and proper algorithms are used in a new experimental setup, it is possible to come up with a solution that removes the common noise terms and impact of coherence length limitations. In this technique, which is called the Phase-Based Multi-Tone Continuous Wave (PB-MTCW) lidar, instead of employing any form of frequency, phase, or amplitude sweeping, a CW laser is modulated with multiple phase-locked radio-frequency tones to generate stable sidebands using a Mach-Zehnder modulator (MZM) under a linear modulation configuration. Then, the phases of individual tones, which are encoded in the echo signal after heterodyning with the unmodulated local oscillator are utilized. Since the absolute value of the phase differences between the reference, i.e. local oscillator, and the echo signal are impaired due beyond the coherence length of the laser, it is possible to acquire the phase differences between RF tones that are free from common noise terms. The phase difference of the individual sidebands reveals the target distance, while the acquired Doppler shift produces the target velocity, simultaneously. The theoretical and experimental proof of single-shot ranging and velocimetry measurements at more than $500\times$ of the coherence length of the laser are presented in Chapter 5.

Chapter 2

Lidar Technologies

2. LIDAR TECHNOLOGIES

2.1. Overview of Lidar Operation

2.1.1. General operating principle of lidars

Light detection and ranging (lidar) is an active detection technique, meaning that the lidar instrument transmits light to the surrounding media and collects back the echo signal from the environment. The working principle of the lidar systems is similar to microwave radars, whereas the shorter wavelengths of the light yield significantly better angular resolution compared to that of radars [51]. For instance, a typical L-band scanning radar operates at a frequency of 1GHz and has a 30cm wavelength, while a lidar possessing a near-infra-red (near-IR) laser has a wavelength of 1.5 μ m considering the eye-safety limits [29]. The existing 4 to 5 order of magnitude difference distinguishes the lidar and radar systems in terms of spatial angular resolution during the generation of the point cloud of the surrounding media.

The general operating principle of lidar systems is presented in Fig. 1 [51]. The transmission (Tx) source, in particular a pulsed or continuous-wave (CW) laser, is brought to free space via Tx optics and the scanning can be realized by beam steering. The optical beam propagates to a target and a portion of the light backscatters to the receiving aperture of the lidar. The light is collected via the receiver (Rx) optics and gets coupled to a detector. By utilizing various properties of light such as time of travel, phase accumulation, local oscillator beatings, etc. a lidar device can compute the distance and velocity of targets.

The technique used to extract the position information of the target determines the lidar architecture. Depending on the lidar methodology, the laser and acquisition systems can be synchronized by waveform generators, and/or the Tx source can be modulated by the waveform generator using direct modulation or electro-optic modulators (EOM), and/or the timing information from the Tx laser can be utilized by the acquisition system for time gating purposes. Similarly, a portion of the lidar techniques exploits coherent detection by keeping a portion of the optical beam as a local oscillator (LO) and coupling it to the optical detector along with the echo signal [52]. Moreover, the waveform generator can also be used as a radio-

frequency (RF) LO source to realize beatings in the RF domain as well. These options are indicated with dashed arrows in Fig. 1.

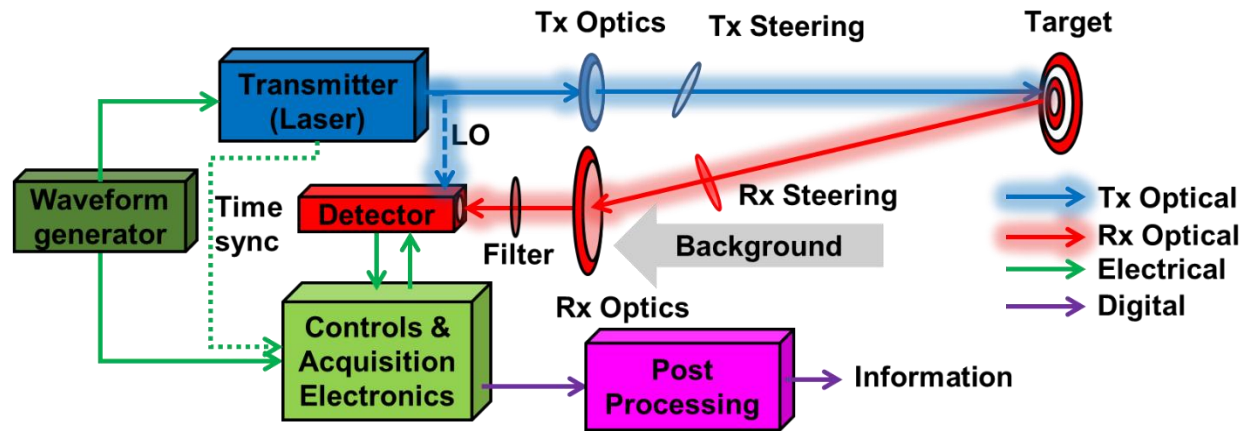


Fig. 1 | General operating principle of lidar systems. Transmission (Tx) optics are shown in blue, receiver optics are shown in red, electrical and radio-frequency (RF) components are indicated in green and digital data is presented in purple.

On the receiver side, the echo signal can be coupled to a detector via beam steering, as well. The collection optics plays a crucial role in the optimization of the signal-to-noise ratio (SNR). One should also consider that the background light is also collected along with the backscattered lidar signal. The background noise consists of sun irradiation, light from unassociated sources, the laser beam from other lidars, reflections from the environment, back reflection from intermediary transparent sources, etc. [53]. There are various techniques to reduce the impact of the background noise, but one of the most robust methods is utilizing an optical filter that is optimized for the laser wavelength to prevent distortion from other sources with different wavelengths.

The echo signal further couples to a detector employing free-space coupling or fiber coupling based on the lidar architecture. The detector type and specifications are also determined by the lidar configuration. The selection of the wavelength indicates the material of the detector. In particular, the operations in the visible spectrum (400nm - 1µm) require silicon (Si) based detector, whereas the laser above near-IR can be detected by an indium gallium arsenide (InGaAs) photodetector [19]. Considering the eye-safety limits for ground-level applications, InGaAs detectors are the prime selection in many applications such as autonomous vehicles, airborne topography lidars for forestry, precision measurement lidars, etc [54].

Besides the wavelength, the selection of the type of the photodiode to be used for the desired application is essential for satisfying the bandwidth and SNR requirements. In particular, avalanche photodiodes (APD), P-I-N (PIN) photodiodes, and balanced detectors are commonly used for lidar detection [51]. There are two types of APDs, linear mode, and Geiger mode. The APDs inherently possess the capability of multiplying the number of electrons generated by the incident photons, thus yielding an amplified photocurrent. They have high sensitivity levels to detect and amplify very weak optical signals. The APDs are commonly used in direct detection lidars for the time of flight measurements [51]. Similarly, due to the saturation levels, it is troublesome to use APDs in a coherent detection configuration with a strong optical LO [29]. Furthermore, there is a trade-off between the active area and bandwidth of the APDs for free-space coupled lidars. As the active area increases for further light collection, the integration time, hence the bandwidth increases [55]. One should also note that the precision of the ranging is proportional to the bandwidth of the timing device since the ranging is performed by measuring the time of light propagation in the time of flight approach [51]. On the other hand, PIN photodiodes within a balanced detection configuration are the prime choice to realize coherent detection with a high-power optical LO depending on the saturation levels of the detector. The bandwidth of the commercially available PIN detectors, especially the fiber-coupled PINs, is relatively wide to realize precise ranging measurements [56]. Even though APD is more sensitive compared to PIN, the inherent amplification of the APD also amplifies the noise in the system. Therefore, it is possible to state that the lidar architecture, laser wavelength, lidar methodology, system requirements, and system specifications dictate the type of detector to be used in a lidar system.

When it comes to the electronic aspect of the lidar architecture, data acquisition plays a similar role to the detectors in terms of bandwidth requirements. The speed of the acquisition electronics should match the detector specifications to realize high precision measurements. After the acquisition, the data can be converted into digital and further post-processed to extract range and/or velocity information depending on the methodology. The post-processing can be realized by conventional signal processing techniques, as well as machine learning implementation to get the desired information out of data [57]. Similarly, the speed of

the processing should also be considered while generating the point cloud information based on the desired application.

2.1.2. Eye safety and lidar wavelength selection

The human eye is capable of detecting light in the visible spectrum which is between 380nm-700nm [58]. Therefore, the selection of the wavelength in the lidar architecture plays a significant role based on the application. For instance, lidars used in autonomous vehicles are operating on the ground level and these systems try to establish a point cloud map of the environment by scanning with the laser. As a result, a portion of the scanning beam has a high probability of interfering with the people and human eyes in the proximity of the lidar system. To prevent any medical issues the wavelength and power of the laser system should be selected based on the eye safety limits [59].

The maximum permissible exposure (MPE) is a measure of the light energy per unit area (J/cm^2) that defines the limits of the interaction of the eye with laser radiation. The dependency of MPE on the wavelength of light is illustrated in Fig. 2 [29]. Here, each color represents the pulse duration of the used lidar system. For CW lidars, the MPE levels in Fig. 2 should be integrated based on the pulse duration to compute the energy limits for eye safety purposes. In addition, the visible spectrum until 1000nm has a higher impact on the human compared to the infra-red region. The light absorption of water is higher in longer wavelengths and the water in the eye prevents light from focusing on the retina for longer wavelengths. The eye absorbs the light that is closer to the, so the light is absorbed in a smaller volume of eye tissue before reaching the retina, meaning that a smaller volume of the eye will heat in a short time frame [29]. As a result, the longer wavelengths i.e. $>1.5\mu m$ is used as common practice for the majority of lidar systems. However, it is possible to utilize the other regions of the light spectrum for various applications. As an example, for space missions where there isn't any human interference, wavelengths such as 1064nm (near-IR), 532nm (visible), and 355nm (ultraviolet) have been utilized by NASA for space missions [60,61].

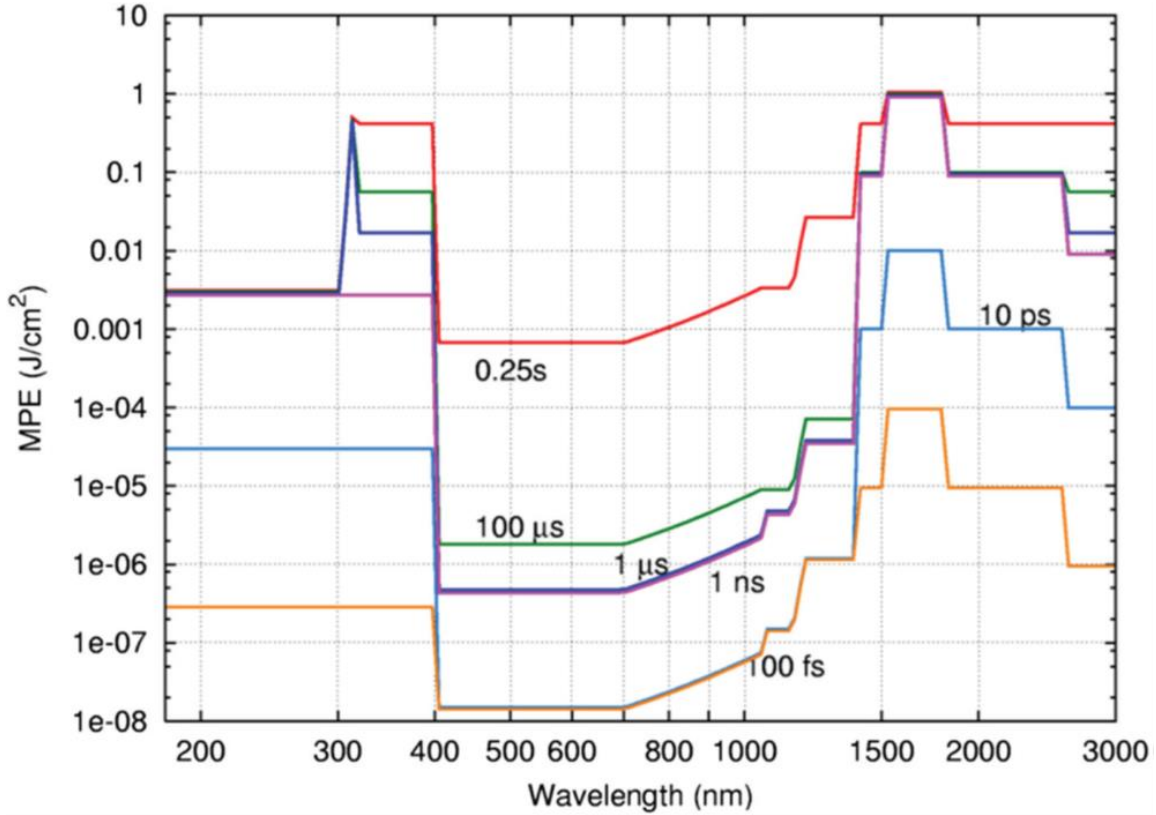


Fig. 2 | The maximum permissible exposure (MPE) curves with respect to the laser wavelengths. Each color represents the pulse duration in seconds.

2.1.3. Types of lidars

As mentioned earlier, there are numerous lidar types based on the principle of operation. For simplicity, it is possible to classify the lidars in two families based on the type of the utilized laser [53]. In particular, these are pulsed lidars and continuous-wave lidars. The overall classification of the lidars is presented in Fig. 3 along with the properties of these techniques.

Time-of-Flight (ToF) lidars operate by direct detection of a propagating laser pulse and time gating the total delay time between transmission and reception of the light [62]. Pulsed ToF (PToF) lidars are currently the most common method in numerous fields such as autonomous vehicles, forestry, etc. [63]. Moreover, pulsed mode lasers have the benefit of using high peak powers to improve the signal-to-noise ratio (SNR), which is vital when the high scattering losses of the echo signal are considered. The duration of the pulse is arranged by considering the eye safety limits as suggested in Fig. 2, peak power requirements, as well as the type of the lidar application [33]. Similarly, repetition of the pulses is selected based on the application

to determine the maximum detection range of the lidar. On the other hand, ToF measurements generally require fast electronics for detection (i.e. high-speed ADCs) and peak extraction algorithms to generate the time of flight of the pulse [64]. Similarly, the ToF lidars cannot inherently generate the speed or direction of motion of a dynamic target with a single pulse measurement. However, by utilizing multiple measurement frames with the constant repetition rate, a ToF lidar architecture can yield the target motion after post processing.

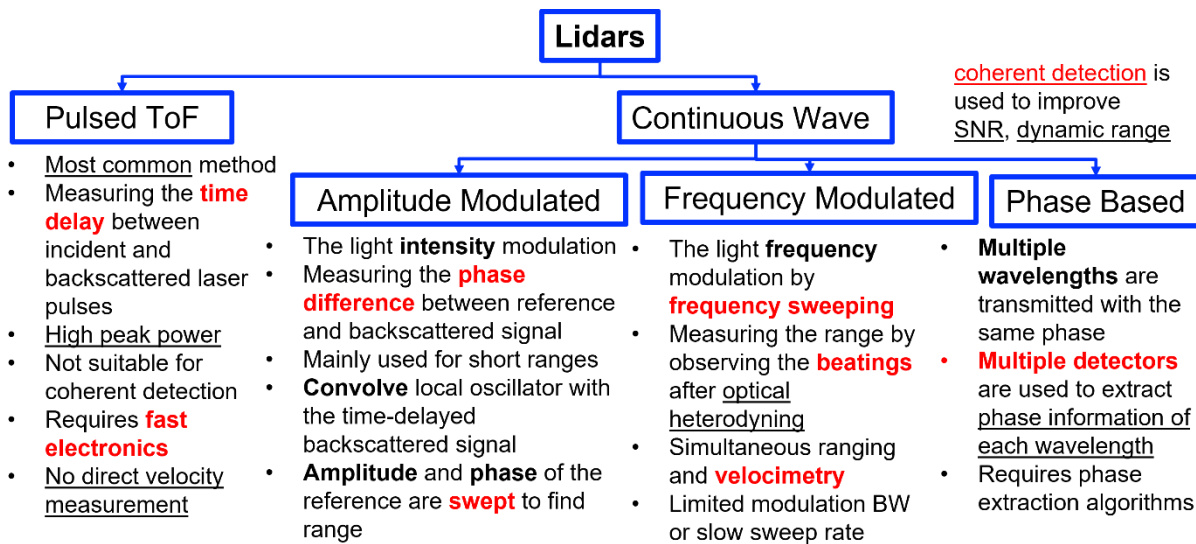


Fig. 3 | Types of lidars. The lidars can be classified as Pulsed Time of Flight (ToF) or continuous-wave, based on the lidar architecture.

Alternatively, continuous-wave (CW) lidars are vastly investigated over the years [56,21,20]. A portion of the CW lidars utilizes coherent detection. By definition, coherence of light means a fixed phase relationship between the electric field values of two laser beams at different locations or at different times [65]. In the case of lidars, temporal coherence plays a vital role in the CW lidars that employ coherent detection via optical homodyne or heterodyne detection. Coherent mode lidars keep a portion of the light within the system as a local oscillator (LO) to beat with the echo signal on the detector. There are various techniques such as amplitude-modulated continuous wave (AMCW), frequency-modulated continuous-wave (FMCW), and phase-based continuous-wave lidars that employ CW lasers. Using coherent detection yields the benefit of improving the SNR on the detection as well as increasing the dynamic range [66]. In

the case of AMCW and FMCW, the lidar architecture relies on a swept-source. Either the amplitude, phase, or frequency of the laser is swept and the phase or amplitude changes between the echo signal and the LO are measured to compute the target distance [28]. For phase-based ranging techniques, multiple lasers with different wavelengths are used with multiple photodetectors. Each wavelength gains a different phase and the target distance is computed by utilizing these phases on multiple lasers [24,67]. Since the coherent lidars employ the beating of two distinct signals (echo and LO), they inherently can capture the Doppler frequency shifts to compute the target speed without comparing it with an additional point cloud frame [68].

2.1.4. Important lidar parameters

Several parameters have been commonly used in the characterization of a lidar system. These are the unambiguous range, range resolution, range precision, range accuracy, and velocity resolution. Definitions of these parameters are stated below in a listed fashion [29].

- **Unambiguous range:** The unambiguous range is the limit within which an object can be detected while its range is still known. This parameter is defined by the pulse repetition rate for ToF lidars and by the sweep period for coherent lidars. In particular, the pulsed or the FM/AM modulated beam with a certain modulation period will be on the flight until it echos back to the detector. For pulsed mode lidars, if there is more than one pulse on the flight, there will exist an ambiguity in the determination of the actual target position during time gating. Similarly, ranging results will start to repeat themselves based on the sweep period in the coherent lidar architectures.
- **Range resolution:** The range resolution is defined as the minimum detectable distance between two objects along the same line of sight. For instance, if two pulses are echoing back to the detector from two close objects back-to-back and if the lidar instrument can distinguish the difference between two pulses in terms of time, then the lidar can resolve both targets. The distance when the two objects started to be detected as one yields the range resolution.
- **Range precision:** The precision quantifies the errors and uncertainties in the measured target distance. The precision of the lidar architecture is proportional to the SNR of the system. Reducing

the impact of the noise components such as thermal noise, shot noise, etc. will yield more certain measurements acquired from a fixed target distance during multiple trials.

- **Range accuracy:** This unit describes how correct the range measurement is compared to the absolute range of the target. This is determined by the SNR of the system (i.e. precision) as well as the systematic errors in the system such as jitter, clock rate, drifts, sweep linearities, etc.
- **Velocity resolution:** Velocity resolution is a term that is used for coherent lidars that can perform simultaneous ranging and velocimetry. The velocity resolution is defined by the frequency resolution of the system. The Doppler shifts induced by the moving target will exhibit themselves on the resultant spectrum during coherent heterodyne detection. The minimum resolvable frequency shift yields the minimum detectable speed difference, as well.

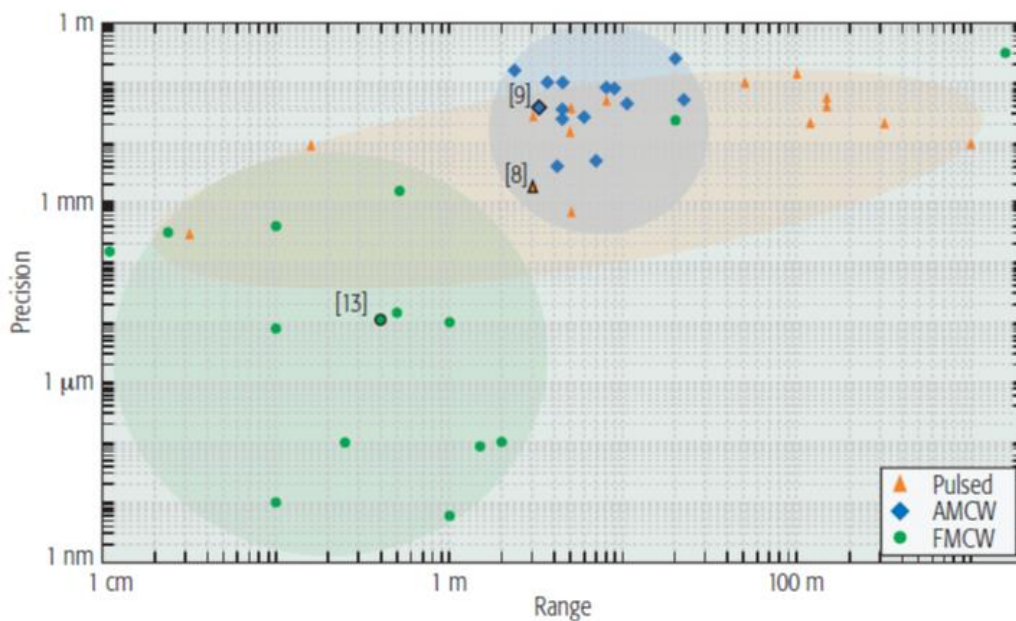


Fig. 4 | Range precision vs. measurement range for pulsed, AMCW, and FMCW lidars after 1990. FMCW lidars yield the best precision, while pulsed lidars can operate at far distances [19].

As stated above, various specifications are defined by the capabilities of the lidar. The type of lidar dictates the performance parameters. In particular, a pulsed lidar can operate at longer distances by exploiting the high peak powers. But the precision of coherent lidars is higher compared to ToF lidars, especially in short distances. The range precision of different types of lidars to the measurement range is

illustrated in Fig. 4 [19]. Therefore, these parameters should be considered while designing the lidar architecture.

2.2. Pulsed Time of Flight Lidar

2.2.1. Working principle

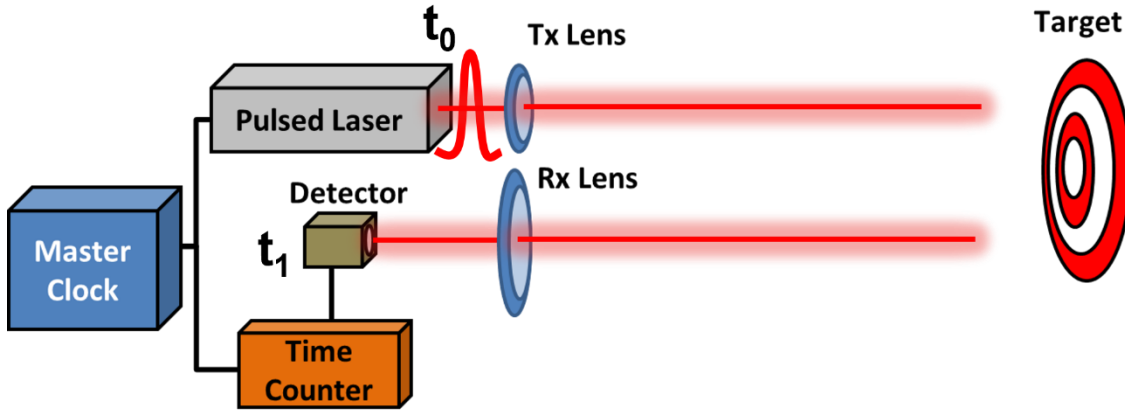


Fig. 5 | Working principle of the pulsed time of flight lidar. t_0 is the time of departure of the pulse from the lidar and t_1 is the time of arrival to the photodetector.

Pulsed time of flight (PToF) lidars operate by measuring the time delay between the transmission and reception pulses. Fig. 5 illustrates the dynamics of the PToF lidars. A master clock drives the pulsed laser and it is utilized for time gating of the pulse in flight to acquire t_0 and t_1 . Here, t_0 is the departure time of the pulse and t_1 is the time of arrival to the photodetector. The target range can be measured by Eq.(2.1), where $\Delta t = t_1 - t_0$ is the time difference, c is the speed of light as 299,792,458 m/s, n_r is the refractive index of the medium (for free-space applications $n_r = 1$), and L_m is the measurement range [51]. Division by 2 is due to the roundtrip of the propagating pulse.

$$L_m = \frac{c \times \Delta t}{2n_r} \quad (2.1)$$

Numerous lidars are operating with the PToF principle, but several examples of PToF lidars can be found in [62,69,70]. The pulsed approach has the capability of achieving high peak powers, which improves the detection range of the lidar system with respect to the detector sensitivity. The commercial PToF lidars

can resolve the objects within a 200-300m range for ground-based applications [71]. By utilizing different architectures for aerial or space-based lidars, the detection range can be enhanced up to ~40km range [60].

2.2.2. Lidar parameters

The unambiguous range of the PToF lidars is defined by the laser repetition period, T_{rep} , of the lidar. As mentioned earlier, the range can be detected if only one pulse is on the flight. The unambiguous range equation is given in Eq.(2.2) [29].

$$L_{unambiguous} = c \frac{T_{rep}}{2} \quad (2.2)$$

On the other hand, the range resolution of PToF lidars is related to the speed of the detection electronics such as the photodetector and ADC. The bandwidth (Δf) of these instruments determines the ability to resolve two objects in close proximity. The range resolution is stated in Eq.(2.3), where δL represents the range resolution.

$$\delta L = \frac{c}{2\Delta f} \quad (2.3)$$

The range precision is determined by the signal-to-noise ratio (SNR) of the lidar architecture. To resolve the target distance a certain SNR is required and the definition of SNR is $SNR = \langle i_s^2 \rangle / \langle i_n^2 \rangle$, where $\langle i_s^2 \rangle$ is the mean squared signal current and $\langle i_n^2 \rangle$ is the means squared noise current. The signal current for a direct detection scheme can be expressed as in Eq.(2.4) [29,72].

$$\langle i_s^2 \rangle = (I_{pd})^2 = R^2 P_s^2 \quad (2.4)$$

Here, R is the responsivity of the detector with A/W units and can be defined as $R = \eta_q q / hf_0$, where η_q is the quantum efficiency, q is the electron charge, h is the Planck's constant, and f_0 is the optical carrier frequency. In the case of an avalanche photodiode (APD), the responsivity is $R_{APD} = M \eta_q q / hf_0$ by considering the APD amplification factor M . The detected photocurrent, I_{pd} , can be expressed as $I_{pd} = R P_s$, where P_s represents the optical power of the signal on the detector.

The noise component includes the detector noises as well as the background noise. Some architectures may also have the optical amplifier noise based on the system requirements. The noise current is formalized in Eq.(2.5). Here shot noise, i_{shot} , thermal noise, i_{th} , and dark current, i_{dk} , are detector-dependent noises, which have different formalisms for APD and PIN diodes. The background noise current, i_{bg} , depends on the environment and may include sun noise. Similarly, amplified spontaneous emission (ASE) due to an optical amplifier can contribute to the noise current, as well.

$$\langle i_n^2 \rangle = \langle i_{shot}^2 \rangle + \langle i_{th}^2 \rangle + \langle i_{dk}^2 \rangle + \langle i_{bg}^2 \rangle + \langle i_{ase}^2 \rangle \quad (2.5)$$

The shot noise manifests when an electric current consists of a stream of electrons that are generated at random times [72]. This noise is a power-dependent noise and for APDs can be expressed as in Eq(2.6), where F_A is the excess noise factor (maximum value is 2) of the APD. Moreover, Eq.(2.7) represents the shot noise for PIN photodetectors. Based on the type of detector, the correct formalism should be used in SNR estimations.

$$\langle i_{shot}^2 \rangle_{APD} = 2qM^2F_A(RP_s + I_{dk})\Delta f \quad (2.6)$$

$$\langle i_{shot}^2 \rangle_{PIN} = 2q(RP_s + I_{dk})\Delta f \quad (2.7)$$

The random motion of electrons at a given temperature in a conductor yields the thermal noise component. In particular, the random motion in the load resistor of the detector causes current fluctuations. As a result, there exists a thermal noise as formalized in Eq. (2.8). In this equation, k_B is the Boltzmann constant ($1.3806488 \times 10^{-23} \text{ m}^2 \text{ kg s}^{-2} \text{ K}^{-1}$), T is the operating temperature in K, F_N is the amplifier noise figure that is caused by pre or main amplifiers, and R_L is the load resistance of the detector. Thermal noise has the same expression for PIN and APD photodiodes.

$$\langle i_{th}^2 \rangle = \left(\frac{4k_B T}{R_L} \right) F_N \Delta f \quad (2.8)$$

The dark current, i_{dk} , is the constant direct current generated by the detector when there is no incident light. In other words, it is the current generated without illumination, and it is dependent on the photodetector characteristics. Furthermore, background noise can be related to sun exposure. The current

generated by the background can be expressed as in Eq.(2.9) for an APD that is similar to shot noise as in Eq.(2.6) [29].

$$\langle i_{bg}^2 \rangle = 2qM^2 F_A R P_{bg} \Delta f \quad (2.9)$$

Here, P_{bg} represents the optical power on the detector due to sun radiation. The optical power of the solar radiation can be estimated by $P_{bg} = SSI \times A_{rec} \times \Delta f_{opt}$, where SSI is the solar spectral irradiance in $W/m^2/nm$, A_{rec} is the receiver aperture area and Δf_{opt} is the optical bandwidth of the solar spectrum on the input facet of the detector [53]. This can be engineered by inserting an optical bandpass filter.

SNR of the lidar architecture will give an understanding of the precision of the PToF lidar. By considering the high scattering losses, and eliminating the background noise with a narrow optical filter, it is possible to simplify the noise terms. Thermal noise will be the dominating term, which is often referred to as the noise-equivalent-power (NEP) of the detector. This indicates the limit where $SNR=1$ and yields the sensitivity of the detector. It determines the maximum distance detectable by the lidar. For an APD the thermal noise limited SNR is presented in Eq.(2.10) for direct detection of the propagating pulse. For PIN photodiode, Eq.(2.10) is still valid while $M = 1$.

$$SNR_{PToF} = \frac{\langle i_s^2 \rangle}{\langle i_{th}^2 \rangle} = \left(\frac{R_L R^2}{4k_B T F_N \Delta f} \right) M^2 P_s^2 \quad (2.10)$$

Moreover, the range accuracy is dependent on the measurement electronics. This is affected by the sampling rate of the system, deviations in the master clock, jitter, timing offset between transmission and reception, drifts, etc. The amount of timing jitter is proportional to rms noise amplitude and inversely proportional to the slope of the timing pulse at the moment of timing (du/dt) [28]. It is challenging to formalize the accuracy, hence it depends on the system specifications and should be characterized experimentally.

The velocity measurements depend on the digital processing of the acquired data in PToF lidars. It is possible to estimate the target speed by comparing multiple acquisitions and $v = dx/dt$ will yield the velocity of the object. The velocity resolution depends on the post-processing algorithms.

2.2.3.Challenges

Even though PToF lidars are being used commercially on multiple platforms, they have limitations such as resolution, lack of simultaneous velocimetry capability, and range walk error. As described in Eq.(2.3), the range resolution depends on the bandwidth of the measurement electronics. This limits the range resolution to several cm for a target stationed 100-200m away from the detector [51,71]. In particular, as the target distance increases, the impact of the noise will be enhanced on the readings, hence the measurement ambiguity will increase, too. There exists a trade-off between the range resolution and the maximum detectable target range due to the proportionality between the detector bandwidth and noise.

On the other hand, unlike coherent lidars, PToF lidar can't acquire the target speed without further post-processing of the data due to the lack of Doppler shift detection. Therefore, the velocity resolution of the PToF output is much coarser compared to that of coherent lidars.

Another important fact about the PToF lidars is the range walk error. This error occurs due to the averaging of the photons on the detector. There exists a discrepancy between the mean value of the measured photons during the integration time, t_{mean} , with respect to the actual photon arrival time t_{tof} [73,74]. The difference in time is $t_{error} = |t_{mean} - t_{tof}|$ and the corresponding ranging error is given in Eq.(2.11).

$$L_{error} = \frac{c \times t_{error}}{2} \quad (2.11)$$

Furthermore, there is an additional uncertainty that can arise from the back reflection from transparent media on the same line of sight. For instance, if the pulse propagates through a glass around 4% of the light will back reflect from the glass and will couple to the detector prior to the actual echo signal from the target [75]. In such a case, the measurement system wouldn't be able to distinguish the position of the target due to multi-path reflection.

2.3. Amplitude-Modulated Continuous Wave Lidar

2.3.1. Working principle

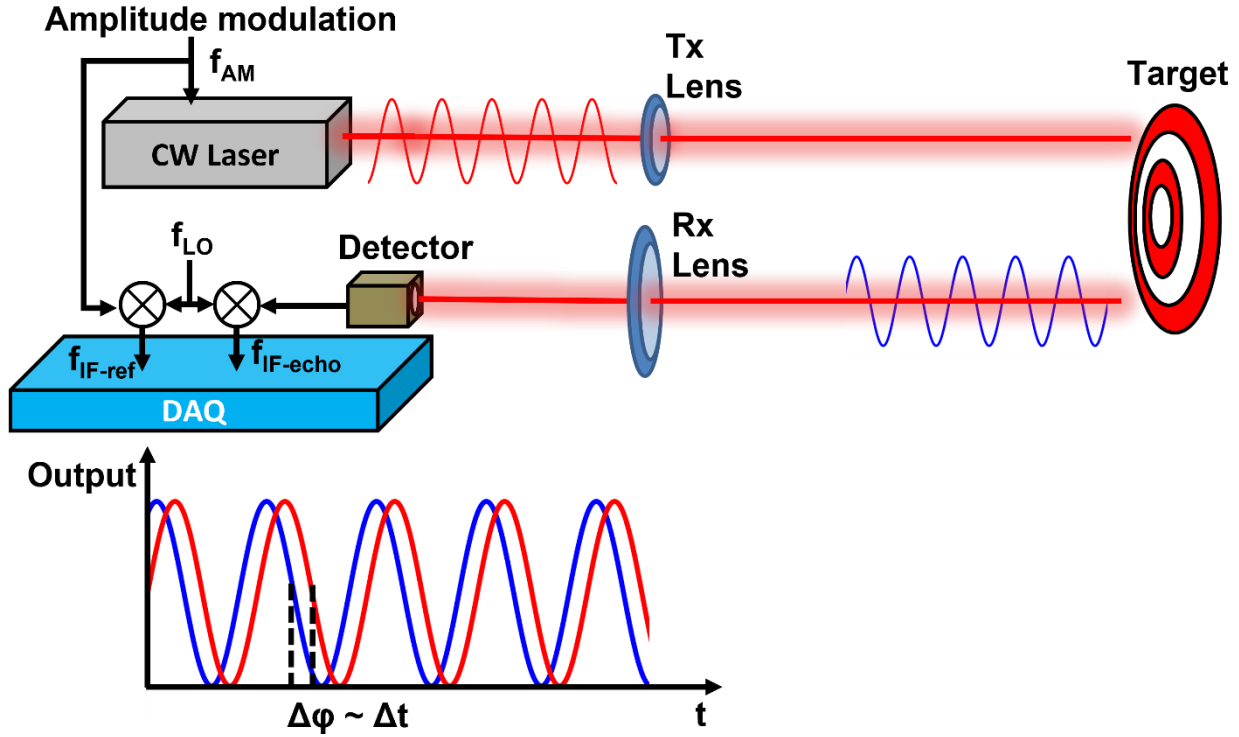


Fig. 6 | Working principle of the amplitude-modulated continuous-wave lidar. A continuous-wave laser is modulated with a fixed frequency sinusoidal (f_{AM}). The backscattered light accumulates a phase and is detected by a photodetector. The measured signal is RF mixed with a local oscillator (f_{LO}) as in a heterodyne configuration, as well as the reference signal. The intermediate frequency (f_{IF}) components are compared to acquire the target distance.

There are multiple amplitude-modulated continuous-wave (AMCW) lidar architectures. In some configurations electronic RF local oscillator (LO) is being used, while some techniques employ an optical LO for enhanced SNR [28,76]. The working principle of AMCW lidar is illustrated in Fig. 6. Here, a CW laser is modulated by a sinusoidal RF signal with f_{AM} frequency. This modulation can be achieved via an electro-optic modulator (EOM) or in some configurations, direct modulation of the CW laser with low frequencies. The transmitted beam propagates and echoes back from to target and the sinusoidal frequency accumulates a phase based on the distance traveled. Compared to the initial phase of f_{AM} , the phase difference will yield the time of flight of the modulated beam as in Eq.(2.12).

$$L_m = \frac{c}{2} \frac{\Delta\phi}{2\pi f_{AM}} \quad (2.12)$$

The phase difference can be expressed as $\Delta\phi = 2\pi f_{AM} \Delta t$, where Δt is the time delay between the reference signal and the received photocurrent. To further enhance the accuracy of the system, the phase shifts are not directly measured. The phase of the intermediate frequency (IF) component is extracted after beating both signals with a fixed RF LO with a frequency of f_{LO} . Then, the resultant f_{IF-ref} and $f_{IF-echo}$ are compared to extract the L_m .

There are numerous studies on AMCW lidar systems [26,30,31]. Due to the lack of high peak powers and dependency on SNR, it is generally preferred to use the AMCW architecture up to a 20m range, which yields resolution on the order of mm levels [28].

2.3.2. Lidar parameters

The unambiguous range of AMCW lidars is determined by the recursive behavior of the phase, meaning that the maximum known range of an object repeats itself after $\Delta\phi = 2\pi$. Therefore the unambiguous range can be expressed as in Eq.(2.13).

$$L_{unambiguous} = c \frac{f_{AM}}{2} \quad (2.13)$$

This limits the modulation frequency of the CW light based on the desired application. Hence, the RF mixing with f_{LO} will generate a low frequency IF tone, which can be utilized to improve the unambiguous range of the AMCW lidar [28]. Moreover, some AMCW architectures employ a quasi-CW configuration to improve the resultant peak power of the light to increase the SNR, as well as to improve the unambiguous range of the system via time gating of the long-duration pulses [19].

On the other hand, the range resolution of the system is determined by the modulation frequency of the CW lidar. As the modulation frequency increases, the resolution of two close objects will increase as well. Hence, Eq.(2.14) indicates the resolution of the AMCW lidars. One should also consider that the modulation frequency is limited by the capabilities of the EOM as well as the detector bandwidth [53].

$$\delta L = \frac{c}{2f_{AM}} \quad (2.14)$$

In addition, the SNR analysis of the AMCW lidar is similar to the PToF lidar configuration. However, instead of the full bandwidth, it is possible to enhance the SNR by utilizing narrow band RF filters around the $f_{IF-echo}$ signal. For instance, an AMCW architecture without an optical local oscillator will be thermal noise limited due to the optical scattering losses. If a bandpass filter is utilized with Δf_{IF} bandwidth, the expected SNR of the system with an APD will be as in Eq.(2.15). By tuning the filter bandwidth, it is possible to improve the SNR of the system.

$$SNR_{AMCW} = \frac{\langle i_s^2 \rangle}{\langle i_{th}^2 \rangle} = \left(\frac{R_L R^2}{4k_B T F_N \Delta f_{IF}} \right) M^2 P_s^2 \quad (2.15)$$

In the coherent AMCW architecture, the modulation phase or frequency is swept and multiple measurements are performed to locate the target distance. However, the SNR equation is different in these systems due to the coherent detection, which will be further explained in the frequency-modulated continuous-wave (FMCW) lidar section.

Similar to PToF lidar, the measurement accuracy is affected by the specifications of the measurement setup [77]. For AMCW lidars, the accuracy is related to the measured phase accuracy of the echo signal. This is determined by the timing jitter, frequency drift of the local oscillator resulting in the drift of f_{IF} , electronic cross-talk between the transmitter and receiver electronics, etc.

2.3.3. Challenges

The main challenge for the AMCW lidars is the relationship between resolution and bandwidth requirements. A high f_{AM} is necessary to enhance the resolution of the acquired range. However, the modulation frequency, as well as the detection bandwidth, are either limited by the specifications of the EOM, detector, and data acquisition electronics. This yields a trade-off between the resolution and SNR of the system. Moreover, the SNR is required for the precision of the measurement, especially for long-distance applications by considering the scattering losses. In addition, the unambiguous range will shorten

as the f_{AM} is increased for high-resolution measurements. Therefore, these parameters should be evaluated and carefully engineered based on the system requirements [53].

Another challenging factor is the phase measurement accuracy which results in the degradation of the range accuracy. To control this, high-speed detection electronics are necessary, especially if high f_{AM} is being utilized in the AMCW architecture. Because of the phase errors induced by jitter, IF drifts, crosstalks, etc. the measurement will deviate from the true value similar to the range walk error of the PToF lidars.

Another limitation of the AMCW lidars is the simultaneous velocimetry measurements. The configurations that don't utilize coherent detection, lack the capability of extracting the Doppler shifts, hence the detection of the speed can be realized as in the PToF lidars.

2.4. Frequency-Modulated Continuous Wave Lidar

2.4.1. Working principle

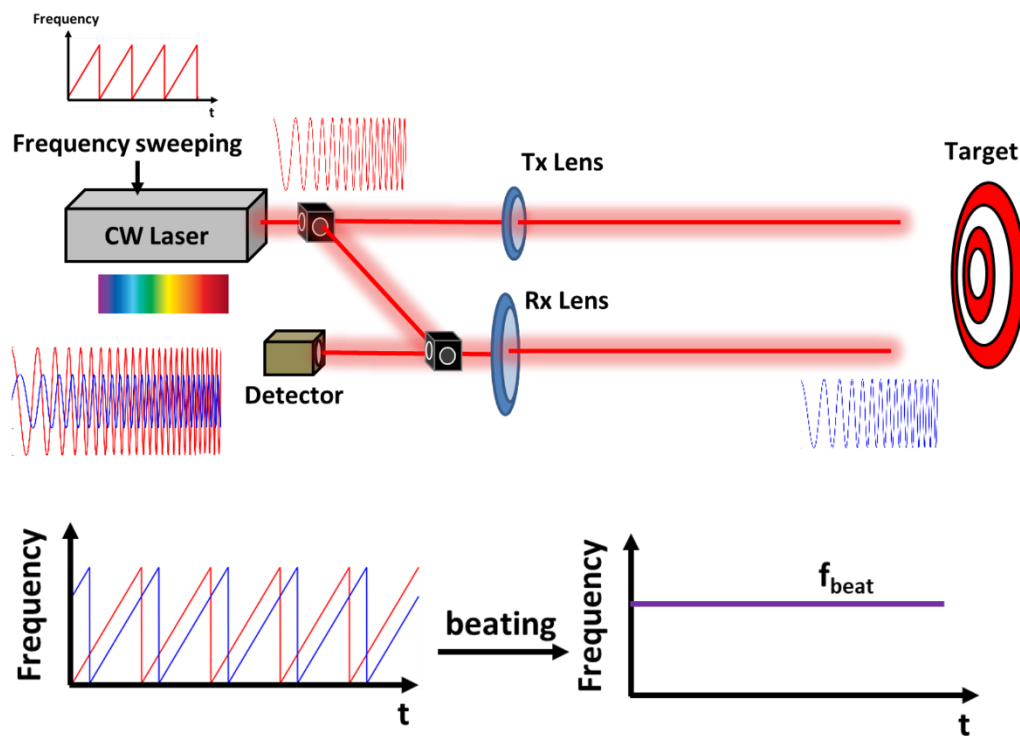


Fig. 7 | Working principle of the frequency-modulated continuous-wave lidar. A continuous-wave laser is frequency-swept for a certain period. A portion of the transmission beam is kept as an optical local oscillator. The echo signal is coherently detected along with the optical local oscillator. The interference pattern of the reference and echo signal yields a beat frequency. Using the sweep period and the resultant beat frequency, it is possible to generate the target range.

The frequency-modulated continuous-wave (FMCW) lidar configuration is presented in Fig. 7. A narrow linewidth CW laser is frequency swept with a certain period, τ , or a chirped source is used. A portion of the swept beam is kept as an optical local oscillator. The echo signal accumulates a time delay and is collected by the receiver optics. Because of this time delay, the frequency of the LO and the echo signal will be different. The optical heterodyne detection is realized on the photodetector and as a result, a frequency beat pattern can be realized. It is possible to construct the target distance by using the beat frequency, f_{beat} , maximum sweep frequency, or the bandwidth, Δf_{max} , and the sweep period. The range equation for FMCW lidar is presented in Eq.(2.16) [19].

$$L_m = \frac{c\tau}{2\Delta f_{max}} f_{beat} \quad (2.16)$$

The frequency sweep has the form of a ramp function and the optical frequency of the swept-source can be expressed as $f_{sweep}(t) = f_0 + \gamma t + f_{nl}(t)$, where f_0 is the optical carrier frequency, γ is the frequency sweep rate and can be expressed as $\gamma = \Delta f_{max} / \tau$, and f_{nl} is the nonlinear part of the frequency sweep [78]. Similarly, the time delay between the reference and echo signals can be formulated as $\Delta t = f_{beat} / \gamma$.

In the case of a dynamic target, FMCW lidar has the capability of generating the target speed due to the coherent detection. The velocity of the target will induce a Doppler frequency shift to the echo signal proportional to its speed as $v = \lambda_0 f_d / 2$, where v is the magnitude of the target velocity, λ_0 is the optical carrier wavelength and f_d is the induced Doppler shift [51]. Assuming a ramp-up sweep followed by a ramp-down sweep within a τ , it is possible to generate the target velocity by using the upwards beat frequency $f_{b,up}$ with the downwards beat frequency $f_{b,down}$ as shown in Eq. (2.17), where θ is the scanning angle with respect to the normal of the output collimator [66].

$$v = \frac{c}{2f_0 \cos \theta} \frac{f_{b,up} - f_{b,down}}{2} \quad (2.17)$$

FMCW lidar is a remarkable technique in terms of resolution and sensitivity, as well as simultaneous velocimetry capability. Utilizing coherent detection increases the dynamic range of the detection and yields

high SNR compared to direct detection. It has been demonstrated that it is possible to detect with a sub-mm resolution for short distances with certain configurations [36,37,79]. Over 100m the resolution degrades to <5cm level by using the FMCW approach [38].

2.4.2. Lidar parameters

Since the swept frequency of the LO is necessary to determine the target distance, the unambiguous range of the FMCW lidar is limited to the sweep period. It is possible to quantify the unambiguous range as in Eq.(2.18). After a complete sweep period, there will be more than one swept light period on the flight that will inhibit the distinguishment of the object.

$$L_{unambiguous} = c \frac{\tau}{2} \quad (2.18)$$

On the other hand, the maximum resolvable distance, L_{max} , by an FMCW lidar is limited to the specifications of the employed laser. Since the architecture relies on coherent detection, the temporal light coherence should be preserved to acquire the frequency beatings. The coherence length, L_{coh} , is determined by the linewidth of the laser, Δf_0 , and can be formulated as in Eq.(2.19) [28]. Therefore, narrow-linewidth single-frequency lasers are opted for FMCW applications to reduce the errors induced by the laser phase noise.

$$L_{max} = \frac{L_{coh}}{2} = \frac{c}{2\pi\Delta f_0} \quad (2.19)$$

The range resolution of the FMCW system is related to the spectral peak width of the measured beat note, δf_{beat} , as well as the sweep rate of the frequency. The range resolution is formulated in Eq.(2.20). It is possible to deduce that the resolution is dependent on the detection bandwidth as well as the linearity of the frequency sweep [78]. Similarly, the velocity resolution depends on the frequency resolution of the detection electronics as $\delta v = c \times df / 2$, where df is the frequency resolution.

$$\delta L = c \frac{\delta f_{beat}}{2\gamma} \quad (2.20)$$

The range precision depends on the measurement precision of f_{beat} , which depends on the SNR of the coherent detection configuration [19]. The coherent detection SNR is rather different compared to PToF and AMCW lidars. Since there is a constant optical LO at the input face of the detector, the system will be shot-noise limited due to the high LO power. The signal power will also be different from that of the direct detection as displayed in Eq.(2.21), where P_{LO} is the optical power of the LO.

$$\langle i_s^2 \rangle = R^2 P_s P_{LO} \quad (2.21)$$

Due to the high bandwidth requirements, PIN photodetectors or balanced photodetectors are commonly used instead of APDs. Therefore the SNR analysis will be performed using a balanced PIN photodetector for coherent detection. Overall SNR is expressed as in Eq.(2.22).

$$SNR = \frac{\langle i_s^2 \rangle}{\langle i_n^2 \rangle} = \frac{4R^2 P_{LO} P_s}{\langle i_{th}^2 \rangle + \langle i_{shot}^2 \rangle + \langle i_{dk}^2 \rangle + \langle i_{bg}^2 \rangle + \langle i_{bg} \rangle \langle i_{LO} \rangle} \quad (2.22)$$

Here, the thermal noise component is the same as Eq.(2.8). Moreover, considering the strength of the LO compared to the echo signal ($P_{LO} \gg P_s$) it is possible to formalize shot noise as in Eq.(2.23).

$$\langle i_{shot}^2 \rangle = 2q(RP_{LO} + I_{dk}) \Delta f \quad (2.23)$$

Moreover, the background noise due to solar radiation will have two components, which are the background-background beating, as well as the background-LO beating. The self-beating term is shown in Eq.(2.24), while the cross-beating term is given in Eq. (2.25) [53].

$$\langle i_{bg}^2 \rangle = 4R^2 P_{bg}^2 \Delta f \Delta f_{opt} \quad (2.24)$$

$$\langle i_{bg} \rangle \langle i_{LO} \rangle = 4R^2 P_{LO} P_{bg} \Delta f \quad (2.25)$$

The dominating term will be the shot noise in Eq.(2.22) by considering a strong P_{LO} and a convenient optical filter to block the solar radiation. Therefore the SNR equation can be simplified as in Eq.(2.26).

$$SNR = \frac{4R^2 P_{LO} P_s}{2q(RP_{LO} + I_{dk}) \Delta f} \sim \frac{4R^2 P_{LO} P_s}{2qRP_{LO} \Delta f} = \frac{2RP_s}{q \Delta f} \quad (2.26)$$

Here, it is possible to realize that the SNR is strongly dependent on the bandwidth of the detection electronics. However, the system resolution is also dependent on the bandwidth, hence yielding a trade-off between the range resolution and SNR of the system. On the other hand, the shot noise limited system generates a higher sensitivity level compared to the thermal noise limited direct detection methods.

In terms of range accuracy, the main limitation arises from the laser phase noise as well as the sweep linearity of the system [28]. The resultant phase errors on the f_{beat} as well as potential linearity deviations will deviate the measured L_m from the actual range of the target.

2.4.3. Challenges

The primary challenge for FMCW lidars is the sweep electronics, in particular the sweep linearity. As described before the frequency sweep equation is $f_{sweep}(t) = f_0 + \gamma t + f_{nl}(t)$, where the nonlinearity term impacts the accuracy of the system. In general, the frequency modulation response of a laser diode is nonuniform against the modulation frequency. Therefore an ideal linear optical frequency sweep cannot be achieved via a linear modulation of the control current. Similarly, the slew rate will limit the transition from ramp-up to ramp-down transitions [78]. Furthermore, fast electronics are required for high-resolution measurements both for frequency modulation and detection.

Another important factor is the coherence length of the narrow linewidth laser. The coherence requirement, as well as the output power requirements, will result in a high-cost single-frequency laser. In addition, there are thermal stability requirements for the laser to have a stable optical carrier frequency. In addition, the unambiguous range is limited to the sweep period and increases the measurement duration per shot.

Chapter 3

Amplitude-Based Multi-Tone

Continuous-Wave Lidar

3. AMPLITUDE-BASED MULTI-TONE CONTINUOUS-WAVE LIDAR

3.1. Motivation

There are various lidar systems, which provide different options to users for desired particular applications. However, every lidar has its own challenges and limitations. The goal of designing the amplitude-based multi-tone continuous-wave (AB-MTCW) lidar is to provide answers to some limitations such as the capability of simultaneous ranging and velocimetry of targets, with single-shot measurements, without employing any form of phase or frequency sweeping, as well as acquiring high-resolution results using a coherent system. The target application for such a device is the aerial and space-based platforms that require repeat measurement with limited sweep windows for long-range measurements. To do so, the AB-MTCW lidar is developed that utilizes multiple fixed RF frequencies on an optical carrier in an interferometric coherent detection configuration.

3.2. Working Principle

3.2.1. Concept

The multi-tone continuous wave (MTCW) lidar technique uses a single CW laser modulated by multiple RF tones and coherent detection for range measurements without employing any form of sweeping [47–50]. In this method, the range is acquired by converting the time delay between the backscattered light and the local oscillator into tone power variations via heterodyne detection. Since the detected RF tones exhibit a sinusoidal pattern based on their individually accumulated phases, and the frequency of this sinusoidal pattern is inversely proportional to the target distance, an accurate range measurement is possible from the recognition of the pattern encoded on RF tone powers.

To realize ranging in the MTCW system, a narrow-linewidth CW laser is modulated by multiple RF tones in a Lithium Niobate Mach-Zehnder modulator. RF tone frequencies are selected according to the detector bandwidth (BW). The modulated optical carrier is then brought to the free space via a collimator and a portion of the beam is separated as a local oscillator to achieve interferometric coherent detection as illustrated in Fig. 8(a). The echo signal is collected back by the detector along with multi-tone RF modulated

reference beam. The heterodyne detection on the device will yield a tone pattern with varying amplitudes based on individual accumulated phases. It is possible to acquire the target position by exploiting the amplitude differences of the tones and fitting a sinusoidal on the amplitudes. The illustration of the resultant tone pattern with the corresponding sine fitting is given in Fig. 8(b). Moreover, the beating of the echo signal and a back reflection from a dynamic target can yield the Doppler shifts near the baseband for simultaneous velocimetry as depicted in Fig. 8.

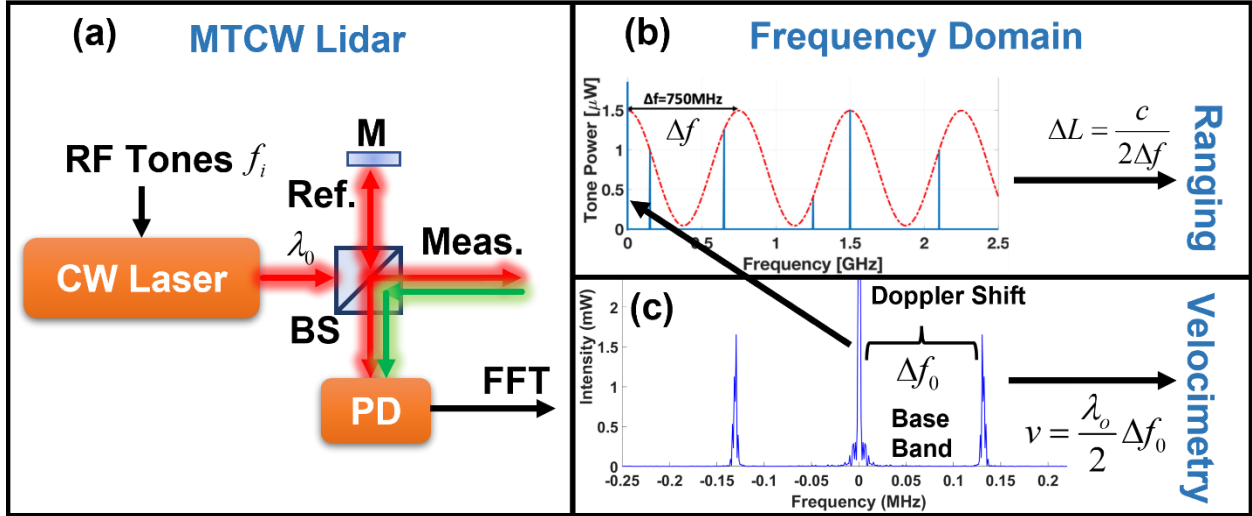


Fig. 8 | Working principle and schematic of AB-MTCW configuration. (a) MTCW Lidar configuration. (b) Ranging is performed by the detected RF modulation tones that exhibit a sinusoidal pattern, and (c) velocimetry is performed by the resultant cross beatings of the RF tones near the baseband in the frequency domain after performing FFT.

3.2.2. Theoretical model of a static target

The theoretical derivation of the AB-MTCW ranging method starts with the output of the CW laser that has an electric field (E-field) as shown in Eq.(3.1). Here, A_0 is the amplitude, $\omega_0 = 2\pi f_0$ is the optical carrier frequency, ϕ_0 stands for the initial carrier phase, k_0 is the wave number and z depicts the propagation distance. The defined variables are indicated in Fig. 9.

$$E_1 = A_0 \exp(j\omega_0 t + j\phi_0) \exp(jk_0 z) \quad (3.1)$$

$$\frac{1}{\sqrt{2}} \left[\cos\left(\frac{\pi}{2V_\pi}\right) E_{RF} - \sin\left(\frac{\pi}{2V_\pi}\right) E_{RF} \right] \quad (3.2)$$

The CW light is modulated via the Mach-Zehnder modulator (MZM) by multiple RF frequencies. The transfer function of the MZM under push-pull configuration is given in Eq.(3.2), where E_{RF} represents the E-field of the electronic RF signal and V_{π} is the quadrature bias voltage of the MZM [47–50,80–83].

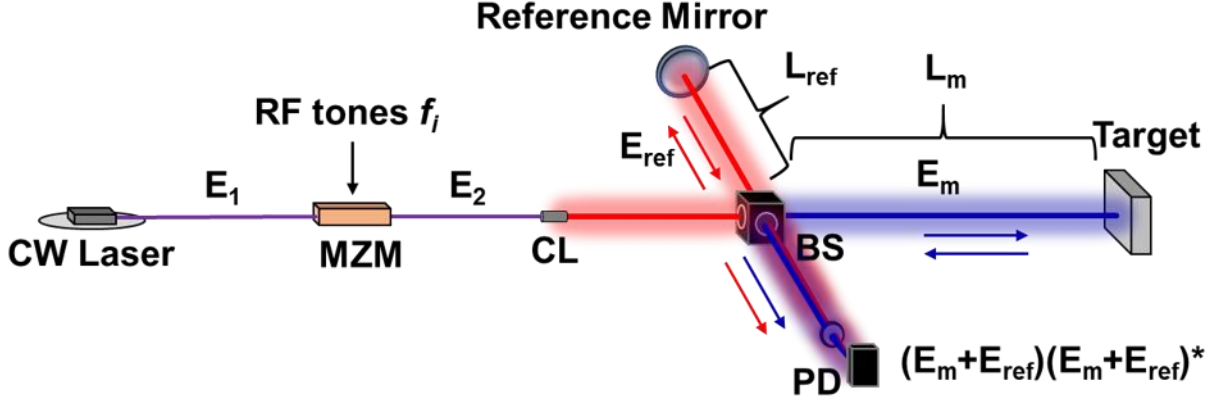


Fig. 9 | Theoretical model parameters on the AB-MTCW configuration. E_1 is the electric field of the CW laser and E_2 is the electric field of the modulated light. E_m and E_{ref} represent the electric field of the reference (LO) arm and measurement arm respectively. L_m and L_{ref} are the measurements and reference ranges.

The E_{RF} is acquired from multiple RF synthesizers, which generate a total of N tones, with each tone having a different frequency of ω_i , amplitudes of A_i , and initial phases of ϕ_i is formalized as in Eq.(3.3).

$$E_{RF} = \sum_{i=1}^N 0.5A_i [\exp(j\omega_i t + j\phi_i) + \exp(-j\omega_i t - j\phi_i)] \quad (3.3)$$

To achieve linear modulation, low modulation depth is used as $m = \pi A_i / V_{\pi} \ll 1$, therefore modulated electric field can be expressed by $E_2 = \frac{E_1}{\sqrt{2}} - \frac{E_1}{\sqrt{2}} \frac{\pi}{2V_{\pi}} E_{RF}$ using small-angle approximations. After inserting E_1 and E_{RF} , the modulated light E-field is obtained as in Eq.(3.4).

$$E_2 = \frac{A_0}{\sqrt{2}} \exp(j\omega_0 t + j\phi_0) - \frac{mA_0}{4\sqrt{2}} \sum_{i=1}^N \exp[(\omega_0 + \omega_i)t + j(\phi_0 + \phi_i)] + \exp[j(\omega_0 - \omega_i)t + j(\phi_0 - \phi_i)] \quad (3.4)$$

The laser beam is then split into two via a beamsplitter (BS), where one arm is kept as the local oscillator and the other as the measurement branch to realize coherent detection on the photodetector (PD). The local

signal is transmitted to the reference mirror that is separated from the BS by a distance L_{ref} . The back-reflected signal from the reference mirror accumulates a phase with respect to the corresponding frequency and has the field equation E_{ref} as given in Eq.(3.5), where α_{ref} is the linear attenuation coefficient realized in the reference arm and c is the speed of light.

$$E_{ref} = \frac{A_0}{2\sqrt{2}} \alpha_{ref} \exp(j\omega_0 t + j\omega_0 \frac{2L_{ref}}{c} + j\phi_0) - \frac{mA_0}{4\sqrt{2}} \alpha_{ref} \sum_{i=1}^N \left(\begin{aligned} &\exp \left[j(\omega_0 + \omega_i)t + j(\omega_0 + \omega_i) \frac{2L_{ref}}{c} + j(\phi_0 + \phi_i) \right] \\ &+ \exp \left[j(\omega_0 - \omega_i)t + j(\omega_0 - \omega_i) \frac{2L_{ref}}{c} + j(\phi_0 - \phi_i) \right] \end{aligned} \right) \quad (3.5)$$

Similarly, the measurement arm will be as in Eq.(3.6) with α_m being the attenuation coefficient of the echo signal.

$$E_m = \frac{A_0}{2\sqrt{2}} \alpha_m \exp(j\omega_0 t + j\omega_0 \frac{2L_m}{c} + j\phi_0) - \frac{mA_0}{4\sqrt{2}} \alpha_m \sum_{i=1}^N \left(\begin{aligned} &\exp \left[j(\omega_0 + \omega_i)t + j(\omega_0 + \omega_i) \frac{2L_m}{c} + j(\phi_0 + \phi_i) \right] \\ &+ \exp \left[j(\omega_0 - \omega_i)t + j(\omega_0 - \omega_i) \frac{2L_m}{c} + j(\phi_0 - \phi_i) \right] \end{aligned} \right) \quad (3.6)$$

L_m is the distance between the target and the output facet of the beamsplitter. The electric field of the reference arm, E_{ref} , after the BS is identical to E_m . A_0 should be modified based on the BS ratio. The photocurrent generated over the photodetector is $I_{PD} = R(E_{ref} + E_m)(E_{ref} + E_m)^*$, where R is the responsivity of the photodiode. The final delivered photocurrent, I_{PD} , by a P-I-N photodiode can be formalized as in Eq. (3.7) for a stationary target without the inclusion of any velocity component [47]. Here, $I_{PD,ave}$ is the average photocurrent due to the sum of all self-beating components.

$$I_{PD} = I_{PD,ave} - \frac{1}{4} RmA_0^2 \sum_{i=1}^N \left(\begin{aligned} &\left(\alpha_{ref} \alpha_m + \alpha_{ref}^2 \right) \cos \left(\omega_i t + \frac{2L_{ref}}{c} \omega_i \right) \\ &+ \left(\alpha_{ref} \alpha_m + \alpha_m^2 \right) \cos \left(\omega_i t + \frac{2L_m}{c} \omega_i \right) \end{aligned} \right) \quad (3.7)$$

As is shown in Eq.(3.7), each RF tone at f_i frequency will accumulate a different phase while traveling to, and back from the target. The phase difference between the measurement and the reference arms can be expressed as $\Delta\phi = (2\Delta L\omega_i / c)$, where $\Delta L = |L_m - L_{ref}|$, after the convolution of the transmitted light with the LO. It is possible to achieve ranging with $(2/c)\Delta L(\omega_2 - \omega_1) = 2\pi$, where ω_2 and ω_1 are the two successive peak frequencies of a sine waveform. Therefore, the amplitude variations due to phase differences will yield a sinusoidal pattern in the frequency domain. Simply, the frequency of the sinusoidal fitting applied to the amplitude of the measured modulation tones will correspond to the path difference between two arms as $\Delta L = c / 2\Delta f_{fit}$, where Δf_{fit} represents the frequency of the fitting curve as shown in Fig. 8(b). Here, the numerical solution of Eq.(3.7) is shown by utilizing five different RF tones up to 2.5GHz. The ΔL is set to 20cm, which yields a sine fitting with 750MHz frequency to illustrate the ranging principle of the AB-MTCW method.

3.2.3. Theoretical model of a dynamic target

On the other hand, simultaneous velocimetry is realized by exploiting the photonic Doppler velocimetry (PDV) technique [68,84]. Due to the movement of the target, the optical carrier and the modulation sidebands will experience a Doppler frequency shift in the measurement arm. The beating of the received frequency-shifted signal with the local oscillator will yield a frequency spike near the baseband as indicated in Fig. 8(c). In this process, the cross-beating terms of the RF tones in the measurement arm wouldn't overlap with the reference arm; thus, the interference will only be depending on the self-beating terms to perform ranging. The E-field of the measurement arm in Eq.(3.6) can be modified into Eq.(3.8) by introducing the ω_d and ω_d^i , which are the Doppler shifts realized by the optical carrier and the modulation frequencies, respectively. The magnitude of the frequency shift determines the speed of the target by $v = \lambda_0 f_d / 2$ or $f_d = 2 \frac{v}{c} f_0$, where v is the speed of the target, and λ_0 is the wavelength of the optical carrier.

The interferometric coherent detection is achieved only if ω_d^i is negligibly small. Such an assumption can be realized by comparing the possible Doppler shifts in the kHz-MHz range and the optical carrier

frequency in the THz. Therefore, the resultant complex Doppler-shifted I_{PD} equation can be simplified by utilizing the approximation of $\omega_d + \omega_d^i \approx \omega_d$. Moreover, the phase shifts of the modulation tones, ϕ_i , and the initial optical carrier phase, ϕ_0 , do not affect the relative phase shift. The phase change due to the main carrier, $\omega_0 \Delta L / c$, yields a resolution in the micrometer range and it is assumed to be averaged out by the target surface roughness and possible small optical path mismatches thus are neglected. By employing these assumptions, it is possible to simplify the resultant cumbersome I_{PD} equation that contains ω_d and the corresponding DC component as in Eq.(3.9) This is analogous to Eq.(3.7) if a static target is assumed with $\omega_d = 0$.

$$E_m = \frac{A_0}{2\sqrt{2}} \alpha_m \exp\left(j(\omega_0 + \omega_d) + j\phi_0 + j\omega_0 \frac{L_m}{c} + j(\omega_0 + \omega_d) \frac{L_m}{c} \right) - m \frac{A_0}{4\sqrt{2}} \alpha_m \sum_{i=1}^N \left\{ \begin{array}{l} \exp\left[\begin{array}{l} j(\omega_0 + \omega_i + \omega_d + \omega_d^i)t + j(\phi_0 + \phi_i) \\ + j(\omega_0 + \omega_i) \frac{L_m}{c} + j(\omega_0 + \omega_i + \omega_d + \omega_d^i) \frac{L_m}{c} \end{array} \right] \\ + \exp\left[\begin{array}{l} j(\omega_0 - \omega_i + \omega_d - \omega_d^i)t + j(\phi_0 - \phi_i) \\ + j(\omega_0 - \omega_i) \frac{L_m}{c} + j(\omega_0 - \omega_i + \omega_d - \omega_d^i) \frac{L_m}{c} \end{array} \right] \end{array} \right\} \quad (3.8)$$

$$I_{PD} = I_{PD,ave} + \frac{1}{4} RA_0^2 \alpha_{ref} \alpha_m \cos(\omega_d t + \omega_d \frac{L_m}{c}) - \frac{1}{4} RmA_0^2 \sum_{i=1}^N \left\{ \begin{array}{l} \alpha_{ref}^2 \cos\left(\omega_i t + \omega_i \frac{2L_{ref}}{c}\right) + \alpha_m^2 \cos\left(\omega_i t + \omega_i \frac{2L_m}{c}\right) \\ + \frac{1}{2} \alpha_{ref} \alpha_m \left(\cos\left[\left(\omega_i + \omega_d\right)t + \omega_i \frac{2L_{ref}}{c} + \omega_d \frac{L_m}{c}\right] + \cos\left[\left(\omega_i - \omega_d\right)t + \omega_i \frac{2L_{ref}}{c} - \omega_d \frac{L_m}{c}\right] \right) \\ + \frac{1}{2} \alpha_{ref} \alpha_m \left(\cos\left[\left(\omega_i + \omega_d\right)t + \left(2\omega_i + \omega_d\right) \frac{L_m}{c}\right] + \cos\left[\left(\omega_i - \omega_d\right)t + \left(2\omega_i - \omega_d\right) \frac{L_m}{c}\right] \right) \\ - \frac{1}{4} m \alpha_{ref} \alpha_m \left(\cos\left[\omega_d t + \omega_i \frac{2\Delta L}{c} + \omega_d \frac{L_{meas}}{c}\right] + \cos\left[\omega_d t - \omega_i \frac{2\Delta L}{c} + \omega_d \frac{L_m}{c}\right] \right) \end{array} \right\} \quad (3.9)$$

As is shown in Eq.(3.9), there will be weak amplitude variations over the RF tones based on the magnitude of the Doppler shifts. If these variations are small, the ranging methodology will still be valid, and the interferometric coherent detection will still be achieved. However, for applications involving faster targets, a frequency-shifter should be integrated into the AB-MTCW lidar to realize the interference by compensating the wide Doppler shifts, which will still enable the AB-MTCW system to perform simultaneous ranging and velocimetry.

It is possible to extract the speed information either by applying short-time Fourier Transform (STFT) to the measured time-domain signal or by measuring the Doppler shift in the base-band after applying Fast Fourier Transform (FFT) for ranging to accelerate the data processing during the measurements. For visualization purposes, the entire flow of the AB-MTCW lidar for simultaneous ranging and velocimetry is illustrated in Fig. 8. The time-domain data carried by I_{PD} is transferred into the frequency domain by performing FFT. First, sinusoidal fitting is applied to the acquired tone powers for ranging. Then the Doppler shift is measured from the frequency spikes near the baseband to extract the velocimetry information by using the same acquired data.

3.3. Numerical Verification

3.3.1. Simulation of the numerical model

The full system of the proposed AB-MTCW lidar is modeled in the computer environment that includes the modulator and detector nonlinearities, laser and detector noises, and losses in the measurement arm to verify the experimental results. In Fig. 10, the evolution of the tone powers is demonstrated while the range of the target is moved up to 30cm from its initial position. The modulation depth is set to 10% and losses are neglected ($\alpha_m = \alpha_{ref} = 1$). To eliminate overlapping of actual tones with higher-order distortions such as harmonic distortions ($2\omega_i, 3\omega_i, \dots$) and the intermodulation distortion ($2\omega_2 \pm \omega_1, 2\omega_1 \pm \omega_2, \dots$), the RF tones are selected as 150MHz, 650MHz, 1.25GHz, 1.5GHz, and 2.1GHz with the same amplitude as shown in Fig. 10(a). When the target is 10cm away, the light propagates a total distance of 20cm back and forth from the target by creating peaks at every 1.5GHz. While the 1.5GHz tone has the same amplitude as before,

650MHz is degraded the most due to the proximity to the valley point at 750MHz that experiences complete destructive interference at the detector as seen in Fig. 10(b). When the target distance is doubled and tripled as in Fig. 10(c) and Fig. 10(d), respectively, the period of the sinusoidal fit decreases accordingly. Therefore, to achieve high resolutions, larger bandwidth is required. For example, by facilitating 50GHz RF bandwidth, the system can achieve <1mm resolution. Such higher resolutions can also be achieved by extrapolating the data of the lower frequency tones and signal processing without going to X-band modulation.

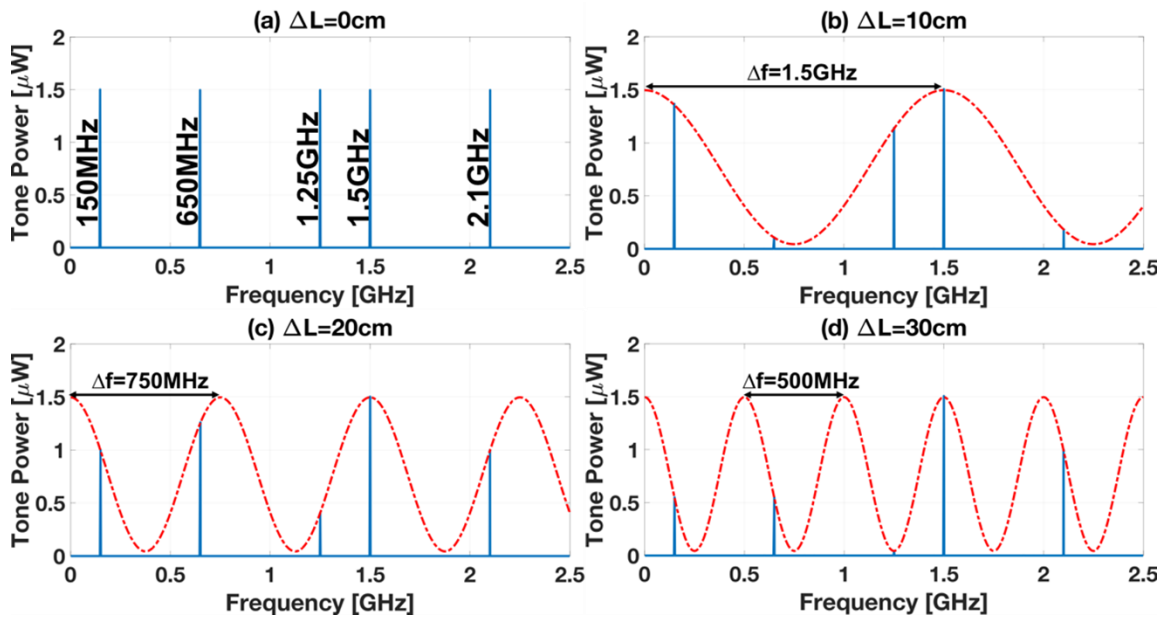


Fig. 10 | Simulation results of the AB-MTCW lidar. RF tone power variation for various target distances and corresponding frequencies. The used tones are 150, 650, 1250, 1500, and 2100MHz. The target distances are (a) $L_m = 0$, (b) $L_m = 10\text{cm}$, (c) $L_m = 20\text{cm}$, and (d) $L_m = 30\text{cm}$.

3.3.2. Scattering loss and unambiguous range characterization

When the target range increases, the consecutive peaks of the sinusoidal fit get closer to each other due to the inverse proportionality of range and frequency as in $\Delta L = \frac{c}{2\Delta f_{fit}}$. However, the same modulation pattern repeats itself according to the period of the greatest common divisor (ω_{gcd}) of all RF tones. For the given tones ω_{gcd} is 50MHz, therefore the same modulation pattern is repeating itself in every 3 meters. This AB-MTCW system is designed for the fine range measurements at the last portion of true range information

(L_m) that can be represented as $L_m = n \times L_{rep} + L_f$, where L_{rep} is the distance of modulation pattern repetition and L_f is the final range of information that can be extracted from this system. However, it is not possible to extract the number of repetitions (n) directly. Using quasi-CW signals can eliminate uncertainty and act as coarse range measurement. For instance, in the case of autonomous vehicles, the 300m operation range requires $2\mu\text{s}$ light propagation. The pulsed modulation with a 100kHz repetition rate and 50% duty cycle can yield sufficient time ($>3\mu\text{s}$) to acquire enough data for averaging. Also, it is possible to further increase the data acquisition time by increasing the duty cycle or decreasing the repetition rate.

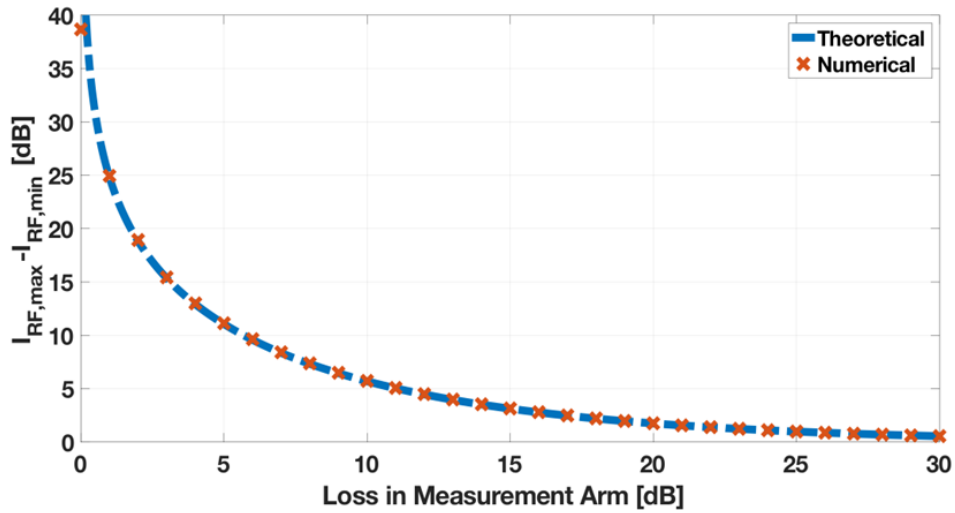


Fig. 11 | Simulation of the impact of the loss in the echo signal. The effect of measurement arm loss on the modulation depth of sinusoidal fit when there is no loss in the reference arm.

Fig. 11 demonstrates how the modulation depth of the sinusoidal fit is decreasing while the backscattered signal is being attenuated with respect to the reference signal. There is a trade-off between the modulation depth and sensitivity of the system. When a high reference power is used, the coherent detection allows you to detect lower scattering powers, however, the variation between the constructive and destructive interference is mitigated. Therefore, the reference power should be optimized for the desired application based on the loss in the measurement arm that is due to divergence, range, and scattering efficiency. AB-MTCW lidar can measure the amplitude variations up to a 20dB power imbalance between the two arms.

3.4. Experimental Verification

3.4.1. Methodology

The experimental setup used for ranging and velocimetry is presented in Fig. 12. To assess the accuracy of the ranging measurement and compare the results, both the AB-MTCW and PToF lidars are implemented on the same platform. Here, the PToF lidar is realized by using a mode-locked (ML) laser with a 25MHz pulse repetition rate. Since the AB-MTCW measures the delay between the reference arm and the target as amplitude variations, the time difference between the pulses from the reference mirror and the target mirror is used to capture the same information in the PToF system. A sample of PToF ranging results is presented in Fig. 13(a), in which Δt represents the time difference between the pulses backscattered from the reference and the target. The path difference is further calculated via $\Delta L = c \times 2\Delta t$. The accuracy of this technique depends on the time resolution of the oscilloscope or data acquisition card, which is set to 50ps and corresponds to a 0.75cm range resolution.

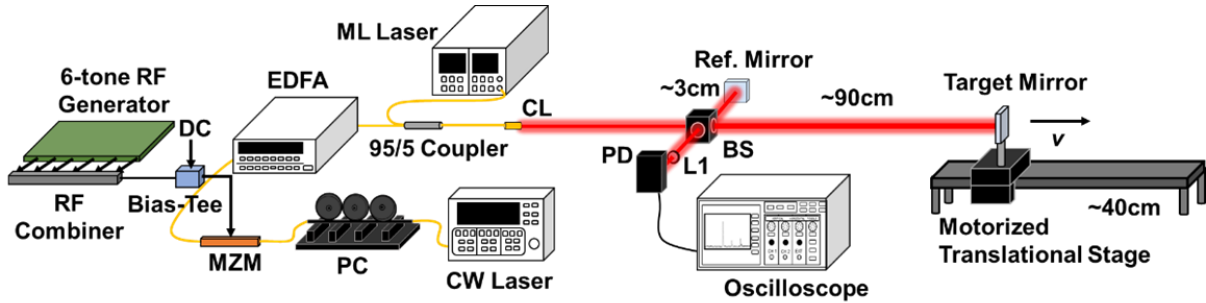


Fig. 12 | The experimental setup used for AB-MTCW and PToF lidar ranging, and simultaneous AB-MTCW lidar ranging and velocimetry. Where the target is a mirror on a motorized translational stage and placed ~90cm away from the output facet of the beam splitter.

The AB-MTCW lidar is built by using a narrow-linewidth CW laser (<1MHz) operating at 1540.2nm with 14mW average output power that yields a coherence length of about 150m to realize coherent detection. The light is further carried to a polarization controller (PC) by a single-mode fiber (SMF) to optimize the modulation with MZM. 6 RF tones at 79, 391, 971, 1657, 2159, and 2623 MHz were generated by generator boards and combined with a 6-channel RF combiner that is followed by a Bias-Tee with an additional 1.3V DC offset to realize quadrature bias at the MZM. To define a sinusoidal pattern at least 2

RF modulation tones are required according to the sampling theory. However, having more than 2 tones will improve the fitting accuracy if the signal is noisy. The experimental demonstration with six tones here, on the other hand, is limited by the number of input ports of the RF combiner used in the setup. Moreover, the tones are carefully selected in a fashion to forestall the cross-beating and the harmonic terms to overlap with the main modulation tones. The modulated light is amplified with a commercial Erbium-doped fiber amplifier (EDFA) with a >10dB gain to achieve a higher SNR. A 95/5 fiber Y-coupler is used to combine the 5% of the ML laser with 95% of MTCW Lidar and feed it to the CL. ML Laser was only operational while ranging is performed with the PToF method.

In the free space, a 50/50 beamsplitter is placed on the optical free-space path to realize interference. A reference mirror is placed ~3cm away from the BS to reflect the beam into the BS, then to the detector for coherent detection. The detected tones in the reference arm are shown in Fig. 13(b). To inhibit any ambiguities due to tone power differences, the acquired measurement data is normalized with respect to the reference arm during each measurement to realize the variations in the tone powers.

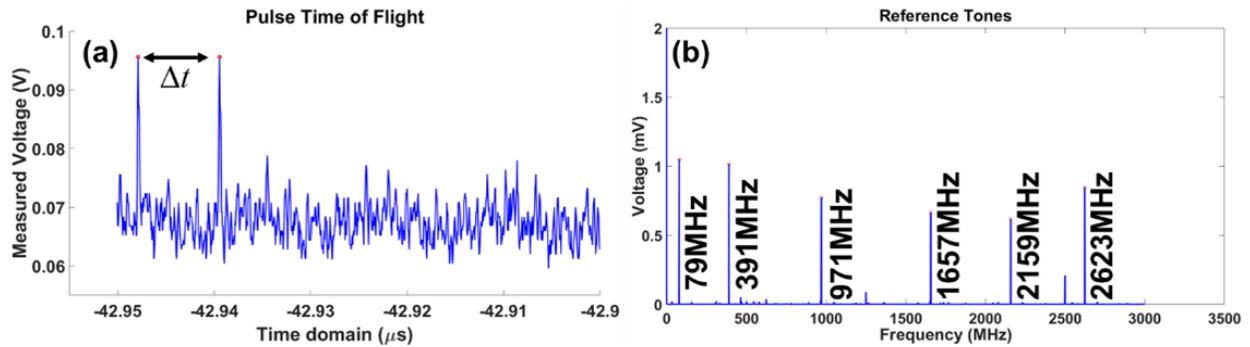


Fig. 13 | Experimental configurations of the PToF technique and AB-MTCW lidar. (a) Performing ranging via PToF technique of a stationary target, (b) acquired reference tones for MTCW ranging.

A pre-programmed motorized translational stage that can move with a desired constant speed, v , up to ~10cm/s is anchored ~90cm away from the BS, and a mirror is stationed on the stage to be used as a target to avoid the power requirements and reduce the effect of α_{meas} for demonstration purposes. The reflected beams from both mirrors are further combined in the BS and navigated into the collection lens (L1). The collected light is compressed by L1 and sent to the free space InGaAs P-I-N photodetector (PD), which has a 5GHz BW and 80μm active area. By considering the thermal noise of the oscilloscope, the minimum

resolvable power is in the μW levels with the utilized PD. The data is acquired by an 8GHz BW oscilloscope, where the time window is set to 100 μs with 50ps time resolution, yielding a 10 kHz frequency resolution, which determines the limit for the velocimetry accuracy.

First, the 40cm long stage is swept in 20 steps with 10 trials per step and at each step, ranging is performed with both AB-MTCW and PToF lidars one at a time. Then the stage is operated in the scanning mode, where the target oscillates back and forth at a constant speed to perform PDV at different speeds. Moreover, 15 different trials are performed while the target is around the midsection of the motorized stage for simultaneous ranging and velocimetry. If they operate at the same time, ML distorts the data acquired by the MTCW technique. Therefore, it is not possible to acquire the position information via PToF at the same instance of data acquisition by AB-MTCW lidar. Due to this adverse issue, the comparison is performed only for stationary targets.

3.4.2. Static target results

The PToF method results yield a total coverage of 87.7cm to 126.7cm from one facet of the stage to the other. The minimum measurable range with the AB-MTCW can be estimated by assuming a single sinusoidal fit in the entire frequency window as $\Delta L_{\min} = c / 2\Delta f_{RF}$, where $\Delta f_{RF} = f_N - f_1 \approx f_N$ is defined by the first and last RF modulation tones f_1 and f_N , respectively. The resultant ΔL_{\min} with the selected RF tones is ~5.9cm. On the other hand, the maximum unambiguous range, $L_{unambiguous}$, of the AB-MTCW methodology can be theoretically defined by the greatest-common-divisor frequency of the selected RF modulation tones, which is 1MHz in the current setup corresponds to ~150m [48,80]. Overall, the current setup is capable of providing range information between 5.9cm-150m without facing any recursion of the emerging sine pattern. During stationary target ranging, sine fitting is performed based on $a_1 \sin(b_1 f + c_1)$ function at each step after normalization with respect to the reference arm, where b_1 represents the frequency of the fitting curve, Δf_{fit} . The sweeping limits for b_1 are set based on the information gathered by the PToF technique to mimic a quasi-CW operation. The average mismatch in range measurements between PToF and AB-MTCW is measured to be ~0.75cm, where 0.75cm is also the range resolution that

PToF can provide with the given RF bandwidth and the sampling rate of the system. In particular, a 5GHz photodetector and 8GHz oscilloscope are used in the experimental system along with a 20GS/s sampling rate, hence the maximum step resolution of the PToF is found to be 0.75cm. Furthermore, the resolution of the AB-MTCW lidar is determined by how well the variations in the tone amplitudes can be detected with respect to the fine step size. This is governed by the noise over the RF modulation tones and the selected tone frequencies. Due to the behavior of cosine, the high-frequency tones will yield larger amplitude variations compared to slower frequencies. With amplitude variations larger than the noise limit, the AB-MTCW lidar will perform ranging with high resolution.

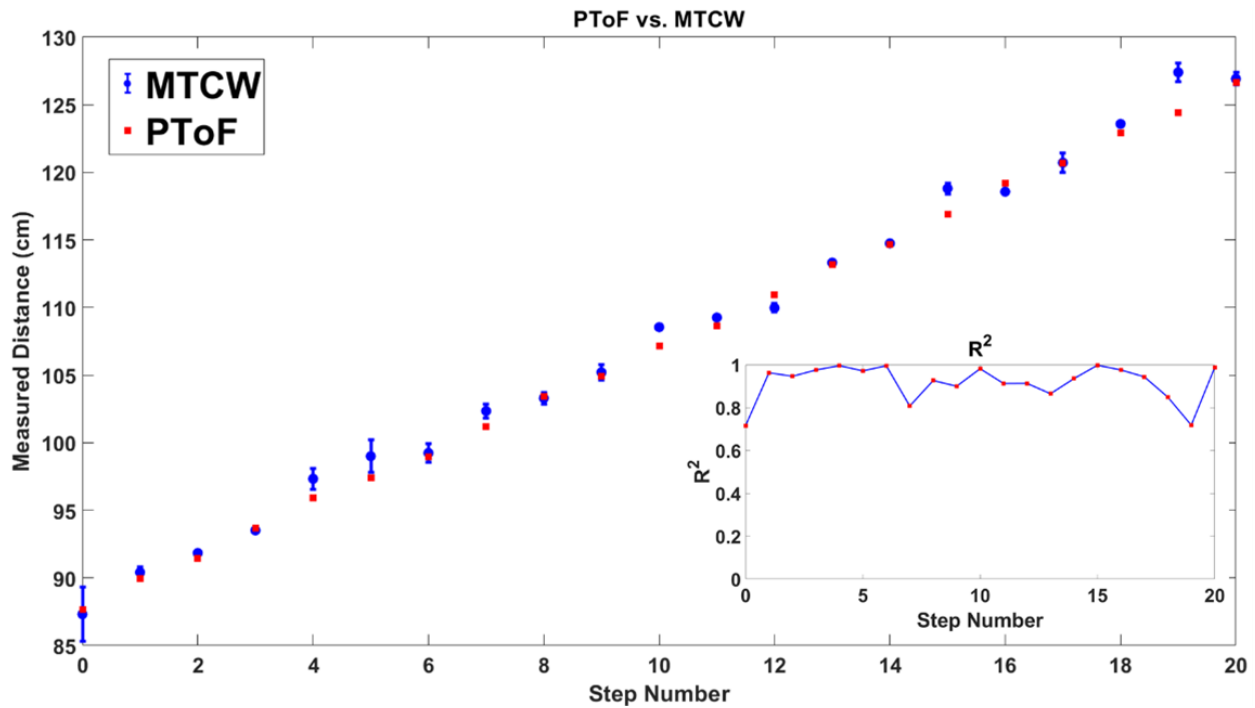


Fig. 14 | Static target ranging results with PToF and AB-MTCW lidars. Stationary target ranging with PToF technique (red) and AB-MTCW lidar (blue) along with the corresponding error bars that represent the standard deviation of 10 trials with respect to the best R^2 data. The inset shows the calculated R^2 at the given step.

On the other hand, the accuracy of the AB-MTCW lidar is governed by the quality of the sine fitting on RF tone power distribution. The detected tone powers after the interference will vary due to the amplified spontaneous emission (ASE) at the EDFA, RF source noises, and detector noises, which will impact the accuracy of the measurements. The amplitude m' of the emerging sine fitting will indicate the accuracy of

the MTCW Lidar technique. Higher the sine fitting amplitude m' , the better matching, and detection accuracy it will produce. Here, the R-squared (R^2) statistical regression model is used to measure the accuracy of the sine fitting algorithm, where $R^2=1$ depicts a perfect fitting, and $R^2=0$ is no correlation. The data with maximal R^2 is selected among the 10 trials at each step and compared with the corresponding PToF measurement as in Fig. 14.

As is clear, the ranging via AB-MTCW Lidar is in close agreement with the PToF results. The greater portion of the results is within the PToF range resolution. The maximum deviation between the two techniques is $<3\text{cm}$, which occurred only in step number 19 at $\sim 124.4\text{cm}$ target distance. This can be attributed to the possible destructive interferences realized by the majority of the tones at the corresponding ΔL that distorts the sine fitting algorithm, and also to the stability of RF sources. The calculated R^2 values vary between 0.715 and 0.997 and the average R^2 is 0.918, which indicates a $>90\%$ accuracy in the sine fitting algorithm. Increasing the number of RF modulation tones, or low noise RF tones may improve the variations in the R^2 measurements. The average standard deviation measured in 20 steps with 10 trials is 0.5cm , which indicates the repeatability, in other words, the precision of the AB-MTCW methodology. Moreover, the error bars in Fig. 14 represent the standard deviation of the measurements while the target is at the same location. The largest deviation is $<2\text{cm}$ and the smallest standard deviation is measured to be 0.12cm .

3.4.3. Dynamic target results

At first, to investigate the PDV with the MTCW setup, only velocimetry is performed without simultaneous ranging. Four different velocity settings are introduced to the motor one at a time to realize four different speeds and corresponding Doppler shifts. Hence, each velocity setting yields a different frequency spike near the modulation tones and the baseband. For instance, an RF modulated optical carrier at f_0 and sidebands at $f_0 \pm f_i$ will move to new frequencies at $f_0 + f_d$ and $f_0 \pm f_i + f_d$, respectively. The new beating tones are used to estimate the velocity of the moving object.

Fig. 15 presents the measured f_d near the baseband under different motor velocity settings. The measured frequencies are at 45, 65, 105, and 135kHz, respectively, and the corresponding calculated speeds are 3.5, 5.0, 8.0, and 10.4cm/s. The measured speeds are verified coarsely by timing the movement of the translational stage and further confirmed with the specs of the electric motor. The resolution of the velocimetry is related to the frequency step size, which is 10kHz. Depending on the sampling of the Doppler shift, there is an error range of about ± 0.8 cm/s during the PDV.

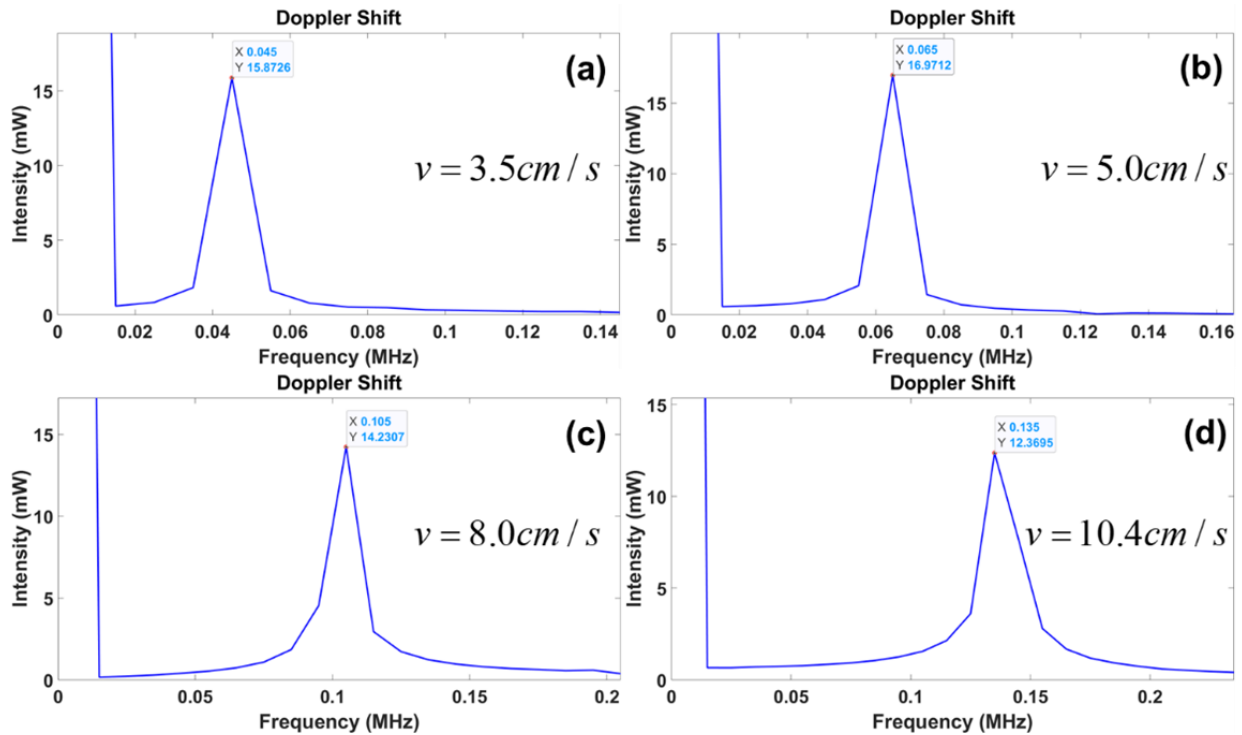


Fig. 15 | Velocimetry results by using AB-MTCW lidar. Frequency spikes at the base band for moving targets with speeds of (a) 3.5cm/s, (b) 5.0cm/s, (c) 8.0cm/s and (d) 10.4cm/s. The corresponding Doppler shifts are 45kHz, 65kHz, 105kHz and 135kHz, respectively.

Due to the employed dual-sideband (DSB) modulation, coherent detection will yield both positive and negative terms caused by the Doppler shift in the RF domain as given in Eq.(3.9). Hence, a standard modulation technique will not resolve the direction of the motion. In order to resolve the direction, a single-sideband (SSB) modulation should be considered. During the SSB modulation, the direction in the shifts near the modulation frequencies will reveal the direction of the speed in the RF domain as $f_i + f_d$ or $f_i - f_d$ where the sign indicates the direction of the motion. The magnitude of the velocity can still be acquired by

the Doppler spike near the baseband; however, the sign of the Doppler shift can only be realized near a modulation tone under SSB configuration. In addition, for the targets with acceleration, the STFT methodology can be employed to map the changes in the speed of the target during selected time intervals [50].

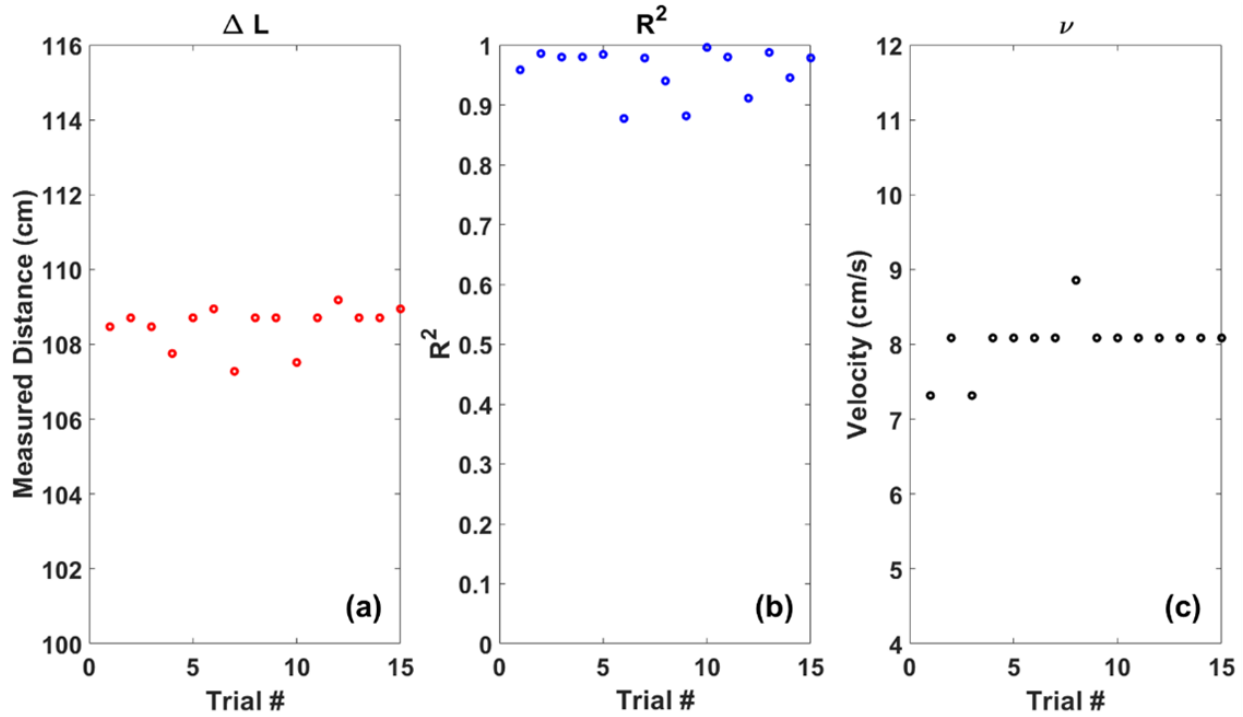


Fig. 16 | Simultaneous ranging and velocimetry results while the target is moving with $\nu=8\text{cm/s}$. (a) Ranging, (b) corresponding R^2 of the sine fitting, and (c) the measured velocity at the same instance.

Simultaneous ranging and velocimetry are performed while the target is passing through the midsection of the translational stage at ΔL of 106-110cm for verification purposes. 15 data points are collected, and the simultaneous range and velocity measurement results are presented in Fig. 16. As expected, the measured ΔL are within the indicated range with high R^2 values in each trial. The lowest R^2 is 0.88 and the average R^2 is 0.96 which indicates the accuracy of the sine fitting. The power transferred to the Doppler spikes from the measured RF tones has a lower impact on the resultant R^2 in the experimental setup. Thus, the average R^2 is found to be within the same range as the average R^2 acquired in the static target case.

The measured frequency spikes near the baseband after coherent heterodyning is $\sim 105\text{kHz}$, which corresponds to a speed of $\sim 8\text{ cm/s}$. The majority of the trials yield the expected value except for trial

numbers 1, 3, and 8. As is seen in Fig. 16(c), the outliers are within the predicted error range of $\pm 0.8\text{cm/s}$. The sampling of the frequency spikes depicts the accuracy; thus, it is possible to improve the velocity resolution by increasing the time window without changing the sampling rate. This will result in compromising on the BW based on the requirements of the desired application.

3.5. Analysis

3.5.1. Lidar parameters

The unambiguous range of the AB-MTCW lidar is determined by the tone selection. In particular, the greatest common divisor of the RF modulation tones yields the unambiguous range of the system as in Eq.(3.10).

$$L_{unambiguous} = \frac{2\pi c}{2\omega_{gcd}} \quad (3.10)$$

It should be noted that the initial phases of the RF tones should be known, or calibrated or a phase-locked loop (PLL) technique should be employed to have tones with fixed phases before leaving the lidar system. In the case of the experiment, the greatest-common-divisor is selected as 1MHz, hence yielding a $\sim 150\text{m}$ unambiguous range for detection.

Along with the unambiguous range, AB-MTCW lidar has the minimum measurable distance limit. The minimum measurable range with the AB-MTCW can be estimated by assuming a single sinusoidal fit in the entire frequency window as $\Delta L_{min} = c / 2\Delta f_{RF}$, where $\Delta f_{RF} = f_N - f_1 \approx f_N$ is defined by the first and last RF modulation tones f_1 and f_N , respectively. This term is calculated to be $\sim 5.9\text{cm}$ for the experiment. In PToF techniques, such a distance is defined as the blind zone which is commonly related to beam steering dynamics [85]. It is possible to configure this distance by manipulating the lidar architecture or fine-tuning the distance of the reference arm to match the ΔL_{min} .

The resolution of the AB-MTCW lidar is similar to that of FMCW lidars. However, since multiple RF modulations are employed, the phase resolution of the RF tones will define the ranging resolution in the AB-MTCW lidar architecture along with the capability of the measurement electronics to resolve the

amplitude variations over each tone. As in the other lidar methodologies, the phase resolution of the detected photocurrent is essentially defined by the time resolution of the detection electronics, in other words, the bandwidth of the system. Thus, the resolution is defined for each modulation frequency as in Eq.(3.11), where dt is the time resolution, $d\phi_i$ is the phase resolution of the i^{th} tone and Δf is the bandwidth of the electronics. Since the complete Δf is not utilized by the AB-MTCW lidar, the resolution can be related to the fastest tone frequency, f_{max} . In this experiment, the range resolution was limited to $\sim 5\text{cm}$ based on the selected maximum tone frequency.

$$\delta L = \frac{d\phi_i}{\omega_i} c = \frac{\omega_i \times dt}{\omega_i} c = \frac{c}{2\Delta f} \sim \frac{c}{2f_{\text{max}}} \quad (3.11)$$

The precision of the AB-MTCW ranging technique is highly dependent on the signal-to-noise ratio (SNR). As described in Fig. 11, the amplitude variations can be detected up to a 20dB power imbalance between the LO and the echo signal. Based on these findings, a variable attenuator in the reference arm was suggested to preserve the m' , which is the modulation depth of the sine fitting. By introducing monitoring power meters co-operating with a variable attenuator to the reference branch, it is possible to manipulate the power of the local oscillator depending on the collected power from the target. Hence, a coarse adjustment on the reference power will be sufficient to achieve the power balance. Otherwise, the reference arm dominates the interference and minimizes the amplitude variations induced by the phase difference. Even though coherent detection is employed as in FMCW lidars, the LO power levels are subject to the collected signal, which alters the impact of the shot noise due to the optical power.

In terms of SNR, the same formalism as of FMCW can be used for coherent detection with a balanced photodetector. The SNR equation for AB-MTCW is given in Eq.(3.12), where P_{ref} and P_{echo} represent the optical power received from the reference arm and the echo signal, respectively.

$$SNR = \frac{\langle i_s^2 \rangle}{\langle i_n^2 \rangle} = \frac{4R^2 P_{\text{ref}} P_{\text{echo}}}{\langle i_{\text{in}}^2 \rangle + \langle i_{\text{shot}}^2 \rangle + \langle i_{\text{dk}}^2 \rangle + \langle i_{\text{bg}}^2 \rangle + \langle i_{\text{bg}} \rangle \langle i_{\text{LO}} \rangle} \quad (3.12)$$

Unlike the FMCW lidar, the power imbalance between the LO and echo should be <20dB to resolve the amplitude variations and by assuming a variable attenuator it is possible to imagine $P_{ref} \approx P_{echo}$. Moreover, the SNR will be limited to the detector sensitivity for low reception powers due to the tunability of the P_{ref} . Therefore, it is possible to simplify Eq.(3.12) to Eq.(3.13) for low optical power cases, where K is a constant defined by the system parameters. Similarly, if the echo signal power is high, the system will be shot noise limited as shown in Eq.(2.26).

$$SNR = \frac{\langle i_s^2 \rangle}{\langle i_n^2 \rangle} = \frac{4R^2 P_{ref}^2}{\langle i_{th}^2 \rangle} = \frac{4R^2 P_{ref}^2}{\left(\frac{4k_B T}{R_L} \right) F_N \Delta f} = \frac{R^2 P_{ref}^2 R_L}{F_N k_B T \Delta f} = K \frac{P_{ref}^2}{\Delta f} \quad (3.13)$$

As shown in this equation, the SNR is depending on the reception power, as well as the electronic bandwidth of the lidar architecture. Since the region of interest in the spectrum is only the pre-selected RF tones, it is possible to enhance the SNR by applying multiple narrow pass filters at the tone frequencies to compute the target distance by the resultant amplitudes. Hence, it is not required to utilize the complete RF spectrum to determine the target position compared to other lidar systems.

Furthermore, another numerical simulation is performed by using RSoft's OptSim[®] optical simulation software to analyze the impact of noise on m' . 6 RF tones up to 3.5GHz are used to modulate a 20mW, 1kHz linewidth input laser operating at 1550nm. The modulated light is amplified up to 1W average output power via an EDFA. In the free space, a time delay that corresponds to a 1m path difference was placed on the measurement side, while the reference arm is kept as a local oscillator after a 50/50 BS. The detection is realized via a P-I-N PD with 5GHz BW that has $R = 0.9A/W$ and a dark current equal to 1.5nA, which matches the specs of the detector used in the experiment. The PD is terminated by a 50Ω load, and room temperature is assumed without any electrical amplifier gain as the parameters for the thermal noise. All the electrical and optical noises are enabled during the simulations in noise-included trials. Both measurement and reference arms are multiplied by the same linear attenuation coefficient to mimic the behavior of a variable attenuator. With this approach, the effect of the single-arm attenuation is isolated to see the impact of the noise alone. The resultant RF tones with noise after each simulation are compared

with the ideal noiseless RF tones. The ideal case yields the best achievable m' that corresponds to maximal measurement accuracy. The deviation in the amplitude of the sine fitting, $\delta m'$, can be represented as $\delta m' \sim \langle \sum_i |P_{ideal}(f_i) - P_{result}(f_i)| \rangle$, where P_{ideal} and P_{result} are the tone powers at i^{th} tone frequency under noiseless and noisy configurations, respectively. The relative $\delta m'$ is presented in Fig. 17 along with the corresponding average received powers at different attenuation levels. The average noise power is calculated to be -73dBm, where the noise equivalent power (NEP) is calculated to be $0.6\text{fW/Hz}^{1/2}$, which matches commercially available PIN PDs [86].

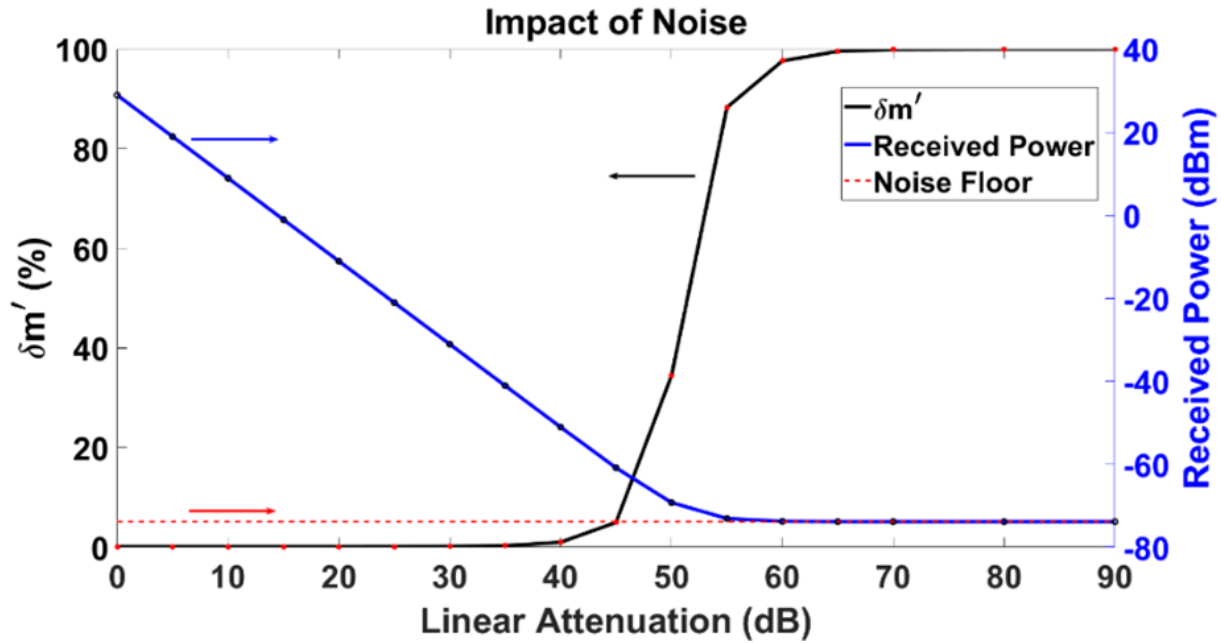


Fig. 17 | Simulation results showing the impact of SNR in AB-MTCW lidar. The deviation in the amplitude of the sine fitting (m') is due to noise (left). The received power with respect to the introduced linear attenuation (right). The noise floor is indicated as -73dBm (right).

$\delta m'$ develops an understanding of the relation between the error in the measurement due to noise and the minimum required power in detection. When the received signal power falls under -50dBm, fluctuations in the tone powers due to noise will alter the sine fitting. Therefore, the measured sine frequency will change, and the accuracy will start to degrade. It is not possible to explicitly differentiate the signal after -60dBm of received power. The largest contribution to noise is caused by the thermal noise, which is further enhanced with the wide BW requirements. Once the effect of α_{meas} and noises are combined, received power

should be high enough to achieve an SNR of $>15\text{dB}$. To mitigate such an issue, quasi-CW pulsation can be realized by introducing applicable repetition rates and duty cycles via the addition of another modulator. As a result, the detected power will be higher, and the RF tone powers will yield the desired sine fitting.

In terms of precision and accuracy, the AB-MTCW system is dependent on the SNR. As mentioned earlier, the SNR can be enhanced by filtering the individual frequencies only. For the experimental demonstration, the precision is determined by the standard deviation from the mean for all the locations. The average standard deviation is measured to be $\sim 0.5\text{cm}$, where the maximum was $<3\text{cm}$ as indicated with the error bars in Fig. 14. In addition, the accuracy of the AB-MTCW lidar is determined by the quality of the sine fitting, which is found via the R^2 regression model. The average R^2 is found as 0.918 indicating a $>90\%$ accuracy in the sine fitting algorithm.

3.5.2. Challenges

The most significant challenge in AB-MTCW lidar is the power balance requirements between two arms that create the need for adaptive power adjustment of the reference arm. By introducing monitoring power meters co-operating with a variable attenuator to the reference branch, it is possible to manipulate the power of the local oscillator depending on the collected power from the target. Hence, a coarse adjustment on the reference power will be sufficient to achieve the power balance. Otherwise, the reference arm dominates the interference and minimizes the amplitude variations induced by the phase difference.

Another crucial factor is the potential ambiguity caused by the initial phases of the RF modulation frequencies. The initial phases of the modulated signal should be known to compute the target position. This can be solved by manipulation of the RF synthesizers as well as the pre-calibration of the system before operation. The known reference branch can be measured prior to the data acquisition to calibrate the initial phases of the RF tones.

In addition, tone selection plays an important role in terms of minimum range, unambiguous range, and range resolution. The minimum range is determined by the maximum tone frequency, while the unambiguous range is defined by the greatest-common-divisor of the RF tones. To enhance the unambiguous range, it is possible to integrate the multi-tone modulated CW light with a quasi-CW pulse to

realize the time gating of the echo signal. As an alternative, it is possible to utilize low-frequency tones along with the high-frequency ones to generate the coarse range information of the target. In terms of resolution, faster tone frequencies will yield greater amplitude variations, in other words, phase variations, over shorter distances, which can enhance the sensitivity of the AB-MTCW lidar in terms of distinguishing the range of closer targets.

Moreover, the AB-MTCW lidar can distinguish the speed of the dynamic target by utilizing the Doppler spikes near the baseband or near the modulation frequencies. However, since the system relies on the beating of two similar frequencies to generate the phase difference as amplitude variations, the high-speed targets will induce a wide Doppler shift to the echo signal that inhibits the realization of amplitude variations. In particular, when the magnitude of the induced Doppler shift exceeds the line width of the laser, the amplitude variations will wash out, hence the AB-MTCW lidar wouldn't be able to generate the target's range. This can be compensated by implementing acousto-optic frequency shifters in the reference arm, to match the frequency of the Doppler-shifted echo signal. Additional techniques to generate the target distance of high-speed targets will be presented in the following chapter.

Besides, the challenges regarding the coherence length of the laser, as well as multip-path interference can also be realized in AB-MTCW lidar architecture, similar to FMCW lidars. Therefore, a narrow linewidth laser is necessary for long-range operations.

Chapter 4

Phase-Enhanced Amplitude-Based

Multi-Tone Continuous-Wave Lidar

4. PHASE-ENHANCED AMPLITUDE-BASED MTCW LIDAR

4.1. Motivation

The potential challenges related to the amplitude-based multi-tone continuous wave (AB-MTCW) lidar are described in Chapter 3. Among others, the wide frequency shift induced by the high-speed dynamic target is a very significant limitation that needed to be addressed. In this chapter, a complementary phase detection algorithm to enhance the capabilities of the AB-MTCW lidar for single-shot simultaneous ranging and velocimetry measurements. As described in the AB-MTCW approach [47,80], the range information of the target is stored in the phases of the individual RF tones. The phase of the Doppler-shifted RF tones and the amount of the induced Doppler frequency shift can be used to extract the range and velocity information, simultaneously. Specifically, the distribution of tones, their phases, and the amplitude information, and utilization of these can enhance the single-shot measurements by AB-MTCW lidar. Combined with pseudo-PToF to generate quasi-CW signals, the technique can give high resolution ranging limited by the maximum tone frequency and temporal resolution of detection electronics irrespective of the target distance. The resolution can be further enhanced by using prediction algorithms [87]. Moreover, the Phase-Enhanced AB-MTCW (PE-MTCW) approach has the potential to mitigate the requirement for a narrow linewidth laser for coherent detection, since the relative phase changes of RF tones are being used instead of absolute phase and frequency measurements as a means to determine the target range.

4.2. Working Principle

4.2.1. Theoretical model

The numerical formalism of the PE-MTCW approach is similar to AB-MTCW with an emphasis on the individual phases of the resultant frequencies. Therefore it is possible to use Fig. 9 to visualize the parameters. Similar to AB-MTCW, the laser beam is split into two via a beamsplitter (BS), where one modulated beam is kept as the local oscillator and the other as the measurement branch to realize coherent detection on the photodetector (PD). The local signal is transmitted to the reference mirror that is separated from the BS by a distance L_{ref} . The back-reflected signal from the reference mirror accumulates a phase

with respect to the corresponding frequency and has the field equation E_{ref} as given in Eq.(3.5), where α_{ref} is the linear attenuation coefficient realized in the reference arm. The electric field in the measurement branch is represented by E_m , where the target speed, v , alters the echo signal by inducing Doppler shift, ω_d , to the optical carrier frequency $\omega_d = \frac{2v}{c}\omega_0$ after the laser beam travels a distance of L_m [68,84]. Similarly, each modulation frequency realizes a Doppler shift ω_d^i , as well. The returned signal electric field equation after the completion of the round trip is shown in Eq. (3.8).

The forward propagating and backscattered light have different phases due to changes in the carrier and modulation frequencies. Since $\omega_0 \gg \omega_i$ it is possible to assume $\omega_d + \omega_d^i \simeq \omega_d - \omega_d^i \simeq \omega_d$. Unless the laser linewidth is in the order of kHz or below and the target is moving at extreme velocities, this assumption is always true for most practical applications. The Doppler shift realized by individual modulation frequencies will be in the <kHz levels even for very fast targets, while the optical carrier will realize MHz level shifts.

After the beams in both arms propagate back to the PD from the reference mirror and the target, the corresponding electric fields will be converted into the detector photocurrent $I_{PD} = R(E_m + E_{ref}) \cdot (E_m + E_{ref})^*$ to realize coherent detection, where R is the responsivity of the PD in A/W. The explicit I_{PD} equation is given in Eq.(4.1), where A_{ref} and A_m stand for $A_{ref} = \frac{A_0 \alpha_{ref}}{2\sqrt{2}}$ and $A_m = \frac{A_0 \alpha_m}{2\sqrt{2}}$, respectively. Moreover, selecting tone frequencies in a manner that prevents frequency overlap between desired beating tones and weak cross-beating tones would improve the crosstalk and spur-free dynamic range of the measurement. Here, the weak cross-beating terms between individual tone frequencies are neglected in Eq.(4.1). The expected spectral peaks in the frequency domain are stationed at ω_d , ω_i , $2\omega_i$, $\omega_i + \omega_d$, $\omega_i - \omega_d$, $2\omega_i + \omega_d$ and $2\omega_i - \omega_d$, and at their negatives if a dual side-band modulation is used. The phases of ω_i and $2\omega_i$ terms are highly dependent on the reference field and have a very small contribution from the measurement arm for a highly unbalanced system. However, the previous AB-MTCW experiments

[47,80] demonstrated how to utilize those tones for range measurements by comparing the relative amplitude variations [47].

$$\begin{aligned}
I_{PD} = & RA_{ref}^2 + RA_m^2 + RA_{ref}A_m \left[\exp\left(j\omega_d t + j\omega_d \frac{L_m}{c}\right) + \exp\left(-j\omega_d t - j\omega_d \frac{L_m}{c}\right) \right] \\
& - mRA_{ref}^2 \sum_{i=1}^N \left[\exp\left(j\omega_i t + j\omega_i \frac{2L_{ref}}{c}\right) + \exp\left(-j\omega_i t - j\omega_i \frac{2L_{ref}}{c}\right) \right] \\
& - mRA_m^2 \sum_{i=1}^N \left[\exp\left(j\omega_i t + j\omega_i \frac{2L_m}{c}\right) + \exp\left(-j\omega_i t - j\omega_i \frac{2L_m}{c}\right) \right] \\
& + \frac{m^2 RA_{ref}^2}{4} \sum_{i=1}^N \left[2 + \exp\left(j2\omega_i t + j\omega_i \frac{4L_{ref}}{c}\right) + \exp\left(-j2\omega_i t - j\omega_i \frac{4L_{ref}}{c}\right) \right] \\
& + \frac{m^2 RA_m^2}{4} \sum_{i=1}^N \left[2 + \exp\left(j2\omega_i t + j\omega_i \frac{4L_m}{c}\right) + \exp\left(-j2\omega_i t - j\omega_i \frac{4L_m}{c}\right) \right] \\
& - \frac{mRA_m A_{ref}}{2} \sum_{i=1}^N \left[\begin{aligned} & \exp\left(j(\omega_i + \omega_d)t + j\left(\omega_i \frac{2L_{ref}}{c} + \omega_d \frac{L_m}{c}\right)\right) + \exp\left(-j(\omega_i + \omega_d)t - j\left(\omega_i \frac{2L_{ref}}{c} + \omega_d \frac{L_m}{c}\right)\right) \\ & + \exp\left(j(\omega_i + \omega_d)t + j\left(\omega_i \frac{2L_m}{c} + \omega_d \frac{L_m}{c}\right)\right) + \exp\left(-j(\omega_i + \omega_d)t - j\left(\omega_i \frac{2L_m}{c} + \omega_d \frac{L_m}{c}\right)\right) \\ & + \exp\left(j(\omega_i - \omega_d)t + j\left(\omega_i \frac{2L_{ref}}{c} - \omega_d \frac{L_m}{c}\right)\right) + \exp\left(-j(\omega_i - \omega_d)t - j\left(\omega_i \frac{2L_{ref}}{c} - \omega_d \frac{L_m}{c}\right)\right) \\ & + \exp\left(j(\omega_i - \omega_d)t + j\left(\omega_i \frac{2L_m}{c} - \omega_d \frac{L_m}{c}\right)\right) + \exp\left(-j(\omega_i - \omega_d)t - j\left(\omega_i \frac{2L_m}{c} - \omega_d \frac{L_m}{c}\right)\right) \end{aligned} \right] \\
& + \frac{m^2 RA_m A_{ref}}{4} \sum_{i=1}^N \left[\begin{aligned} & \exp\left(j(2\omega_i + \omega_d)t + j\left(2\omega_i \left(\frac{L_m + L_{ref}}{c}\right) + \omega_d \frac{L_m}{c}\right)\right) \\ & + \exp\left(-j(2\omega_i + \omega_d)t - j\left(2\omega_i \left(\frac{L_m + L_{ref}}{c}\right) + \omega_d \frac{L_m}{c}\right)\right) \\ & + \exp\left(j(2\omega_i - \omega_d)t + j\left(2\omega_i \left(\frac{L_m + L_{ref}}{c}\right) - \omega_d \frac{L_m}{c}\right)\right) \\ & + \exp\left(-j(2\omega_i - \omega_d)t - j\left(2\omega_i \left(\frac{L_m + L_{ref}}{c}\right) - \omega_d \frac{L_m}{c}\right)\right) \\ & + \exp\left(j\omega_d t + j\left(2\omega_i \left(\frac{L_m - L_{ref}}{c}\right) + \omega_d \frac{L_m}{c}\right)\right) + \exp\left(-j\omega_d t - j\left(2\omega_i \left(\frac{L_m - L_{ref}}{c}\right) + \omega_d \frac{L_m}{c}\right)\right) \\ & + \exp\left(j\omega_d t + j\left(2\omega_i \left(\frac{L_m - L_{ref}}{c}\right) + \omega_d \frac{L_m}{c}\right)\right) + \exp\left(-j\omega_d t - j\left(2\omega_i \left(\frac{L_m - L_{ref}}{c}\right) + \omega_d \frac{L_m}{c}\right)\right) \end{aligned} \right]
\end{aligned} \tag{4.1}$$

The Eq.(4.1) can be further simplified for frequency tones at $\omega' = \omega_i \pm \omega_d$ or $\omega' = 2\omega_i \pm \omega_d$ as $4\cos\left(\frac{\phi'}{2} - \frac{\phi''}{2}\right)\cos\left(\omega't + \frac{\phi'}{2} + \frac{\phi''}{2}\right)$ by using trigonometric identities. The definitions of $\left(\frac{\phi'}{2} - \frac{\phi''}{2}\right)$ and $\left(\frac{\phi'}{2} + \frac{\phi''}{2}\right)$ for each tone are given in Table 1 Hence, their amplitudes and phases reveal the range information as indicated in Eq.(4.1) and Table 1 [81,88]. In particular, the phases of the measurable tones for the range information are given. However, as shown in these definitions, for a system with N RF tones at the there are $4N$ frequency tones for data analysis for dynamic targets and there are $2N$ tones for static targets to extract the range information only, which is instrumental to increasing the robustness and accuracy of the system. Here, the objective is to have an algorithm for single-shot range and velocity measurements by utilizing the phases rather than the tone amplitudes. For illustration purposes, the main focus will be on the phase accumulations of tones at $\omega_i + \omega_d$ and $\omega_i - \omega_d$ only.

Table 1 | Resultant frequencies and their corresponding amplitude, phase, and L_0 equations.

Frequency	Amplitude $\left(\frac{\phi'}{2} - \frac{\phi''}{2}\right)$	Phase $\left(\frac{\phi'}{2} + \frac{\phi''}{2}\right)$	$L_0^{\omega_i \pm \omega_d}$
$\omega_i + \omega_d$	$-4mRA_m A_{ref} \cos\left(\frac{\omega_i}{c}(L_m - L_{ref})\right)$	$\frac{\omega_i + \omega_d}{c}L_m + \frac{\omega_i}{c}L_{ref}$	$L_0^{\omega_i + \omega_d} = \frac{c\phi_{\omega_i + \omega_d}^{meas} - \omega_i L_{ref}}{\omega_i + \omega_d}$
$\omega_i - \omega_d$	$-4mRA_m A_{ref} \cos\left(\frac{\omega_i}{c}(L_m - L_{ref})\right)$	$\frac{\omega_i - \omega_d}{c}L_m + \frac{\omega_i}{c}L_{ref}$	$L_0^{\omega_i - \omega_d} = \frac{c\phi_{\omega_i - \omega_d}^{meas} - \omega_i L_{ref}}{\omega_i - \omega_d}$
$2\omega_i + \omega_d$	$\frac{m^2 RA_m A_{ref}}{2}$	$\left(2\omega_i \left(\frac{L_m + L_{ref}}{c}\right) + \omega_d \frac{L_m}{c}\right)$	$L_0^{2\omega_i + \omega_d} = \frac{c\phi_{2\omega_i + \omega_d}^{meas} - 2\omega_i L_{ref}}{2\omega_i + \omega_d}$
$2\omega_i - \omega_d$	$\frac{m^2 RA_m A_{ref}}{2}$	$\left(2\omega_i \left(\frac{L_m + L_{ref}}{c}\right) - \omega_d \frac{L_m}{c}\right)$	$L_0^{2\omega_i - \omega_d} = \frac{c\phi_{2\omega_i - \omega_d}^{meas} - 2\omega_i L_{ref}}{2\omega_i - \omega_d}$

One of the challenges in the proposed technique is the modulo 2π cyclic pattern of the phase accumulation. In other words, $\phi_{\omega_i \pm \omega_d}^{meas}$ represents the measured phase of the indicated frequency term, where

$$0 \leq \phi_{\omega_i \pm \omega_d}^{meas} \leq 2\pi, \text{ and yields the same phase result for every } L_m \text{ such that } L_m = L_0^{\omega_i \pm \omega_d} + \frac{2\pi c}{\omega_i \pm \omega_d} n_i, \text{ where } n_i$$

is an integer related with the i^{th} frequency and $L_0^{\omega_i \pm \omega_d}$ is the measured length in the first cycle of the i^{th}

frequency when $n_i = 0$. Therefore, the multiple tones will be used to facilitate triangulation algorithms. In

particular, if the integer $n_i = \left\lfloor \frac{L_m}{\lambda_{i-RF}} \right\rfloor$ is defined, where λ_{i-RF} is the RF tone wavelength, then it is possible to

formalize the measurement distance L_m for a given phase measurement as in Eq. (4.2).

$$L_m = \frac{\left(2\pi n_i + \phi_{\omega_i \pm \omega_d}^{meas}\right) - \frac{\omega_i L_{ref}}{c}}{\frac{\omega_i \pm \omega_d}{c}} \quad (4.2)$$

Hence, for a given maximum measurable distance L_{m-max} that is determined by the system parameters, such as laser power, laser linewidth, SNR of the system, etc., there will be multiple solutions for the same target. While higher tone frequencies are desired for high resolution ranging, they are handicapped due to increasing n_i value. Low-frequency tones produce a lower number of solutions with coarser resolutions, whereas the rapidly varying phases on the higher frequency tones generate multiple solutions with higher resolutions. The actual ranging solution is a triangulation of all tone frequencies. One method of converging to a single solution after triangulation is selecting the lowest frequency RF tone as $\lambda_{i-RF} \geq L_{m-max}$. However, this will impose additional constraints on the detection electronics and the length of the time window for the desired application. Similar to constraints in FMCW, if there is extensive scanning involved, using a longer time window will limit the number of scans that can be performed per second. Therefore, the number of RF tones and their frequency ranges should be determined based on the desired resolution and maximum ranging distance L_{m-max} . However, implementation of a pseudo pulsation or quasi-CW operation that uses long pulses with multi-tone RF modulations imposed on them can further enhance this approach by eliminating the limits of n_i described above and providing a higher SNR solution due to high peak power excitation.

Similar to FMCW lidars, the frequency variations due to Doppler shift are used to identify the velocity information [89]. There are up to $2N$ degrees of freedom to estimate the velocity information. The precision of the velocity measurement is determined by the time window used to capture the range. For instance, a 1ms time window will yield a 1kHz spectral resolution that corresponds to 1mm/s or 1.5mm/s resolutions

in velocity measurements by using a $1\mu\text{m}$ laser or by using a standard telecom laser at $1.55\mu\text{m}$, respectively. The variations in Doppler shifts at different RF tones are negligibly small in most applications. For practical purposes, using tones with higher powers would yield high SNR velocity measurements. The value of ω_d can be extracted from the photocurrent spectrum by comparing the ω_i or $2\omega_i$ tones and their corresponding Doppler-shifted $\omega_i \pm \omega_d$ or $2\omega_i \pm \omega_d$ tones, respectively, or by evaluating the Doppler peak near the baseband.

4.2.2. Triangulation algorithm

The triangulation algorithm is used after calculating $L_0^{i,j} = c\Delta\phi_{i,j} / \Delta\omega_{i,j}$, the final range estimation without recursions, from the phase variation of the individual tones to determine the actual value of the target distance L_m , where $\Delta\phi_{i,j}$ and $\Delta\omega_{i,j}$ represent the phase and frequency differences of the i^{th} and j^{th} tones, respectively. It is possible to generate a total of $\binom{N}{2}$ possible $L_0^{i,j}$ for a stationary target, whereas the targets in motion will yield $\binom{2N}{2}$ degrees of freedom. The final estimated L_m values should converge to the same value for each integer n_i based on $L_m = L_0^{i,j} + n_i L^{i,j}$ where $L^{i,j} = 2\pi c / \Delta\omega_{i,j}$.

Here, the maximum anticipated range of a target is set by selecting the maximum value of n_i . In practice, this range is determined by the total loss of the system or the application. Then, the integer value of n_i is scanned from $n_i = 1$ to n_{max} and all the estimated L_m are concatenated in a data matrix $M_{k,l}$, where k is equal to n_{max} and l is the number of available $\Delta\omega_{i,j}$, also corresponding L_m for each $\Delta\omega_{i,j}$ are placed in an increasing fashion to each column. An example of the data matrix $M_{k,l}$ is given in Fig. 18 after acquiring data with a 3-tone PB-MTCW lidar. Finally, the standard deviation of each row is computed as

$$\sigma_k = \sqrt{\sum_{r=1}^l (M_{k,r} - \overline{M}_k)^2 / l}, \text{ where } \overline{M}_k \text{ is the mean value of the } k^{\text{th}} \text{ row. Then the first column of } M_{k,l} \text{ is}$$

matched with σ_k to find the standard deviation at the corresponding L_m . The length where the minimum σ_k is found will yield the closest target range since all the calculated L_m converges to this particular range value.

		l		
		$\omega_3 - \omega_2$	$\omega_3 - \omega_1$	$\omega_2 - \omega_1$
1	$k = 1$	$k = 1$	$k = 1$	$k = 1$
2	$k = 2$	repeat	repeat	repeat
3	$k = 3$	repeat	repeat	repeat
4	$k = 4$	repeat	repeat	repeat
\vdots	\vdots	repeat	$k = 2-10$	$k = 2-10$
300	$k = 300$	$k = 2$	$k = 11$	$k = 11$
k 301	$k = 301$	repeat	repeat	repeat
302	$k = 302$	repeat	repeat	repeat
\vdots	\vdots	$k = 3$	$k = 12-17$	$k = 12-17$
498	$k = 498$	repeat	$k = 18$	$k = 18$
499	$k = 499$	repeat	repeat	repeat
500	$k = 500$	repeat	repeat	repeat

Fig. 18 | Example of the triangulation matrix. Illustration of data matrix $M_{k,l}$ for a 3-tone PE-MTCW lidar with ω_1 , ω_2 , and ω_3 . The k values in the matrix represent the value of n in $L_m = L_0^{i,j} + (2\pi n_i c / \Delta\omega_{i,j})$. The repetitive terms, where the k values are equal in the consecutive rows are indicated in the matrix as repeat.

4.3. Numerical Verification

4.3.1. Simulation parameters

A numerical verification is performed by mimicking simultaneous ranging and velocimetry of a fast-moving target to demonstrate the system's capability. To configure the MTCW lidar, a narrow linewidth CW laser is set to operate at a 1 μ m central wavelength. The laser beam enters the MZM with a selected modulation depth of $m = 0.01$ to maintain the linearity of the modulator. Four modulation frequencies are fed to the MZM at 75MHz, 500MHz, 1900MHz, and 2450MHz. These tones are carefully selected in a fashion to forestall any form of frequency overlapping over a $\omega_i \pm \omega_d$ frequency span. MZM output is followed by a beam splitter. At the detector, the reference signal amplitude is set to be $\alpha_{ref} = 1$, while the signal from the target has an attenuation of $\alpha_m = 0.01$ pointing out a 20dB loss due to scattering.

An InGaAs PIN photodetector is assumed in the system with a 5GHz bandwidth based on the selected tone frequencies, and 0.9A/W responsivity in accordance with the commercially available detectors. The load impedance of the detector is set to 50Ω. For simplicity and proof of concept purposes, detector noises such as the shot noise and the thermal noise are neglected. In the simulation, a 256μs time window with about 61 ps temporal resolution (i.e. 2^{22} samples) is used, which corresponds to a total of a 16.4GHz frequency window and ~4kHz frequency resolution. The L_{ref} is preselected in the system as 10cm and the target is set to be $L_m = 50\text{m}$ away from the lidar with a movement speed of 30m/s (108km/h) in the direction of the laser beam propagation. This speed induces a 60MHz Doppler shift to the optical carrier. Eq.(3.5) and Eq.(3.8) are used by setting $\phi_o = \phi_i = 0$ to acquire the resultant I_{PD} . In practice, the initial phases of RF tones can be set by synchronization of RF generators via master-slave operation.

4.3.2. Simulation results

The detected time-domain signal by the PD is converted into the RF spectrum via Fast Fourier Transform (FFT) as shown in Fig. 19. The significant frequencies are indicated on the spectrum, which are ω_d , ω_i , $2\omega_i$, and $2\omega_i \pm \omega_d$. There are in total of 8 frequency spikes that are applicable for Eq.(4.2). These peaks are found via a peak finding algorithm and by using the known ω_i and measured ω_d values as reference points.

On the other hand, it is possible to acquire the value of ω_d by analyzing the spike near the baseband or the peaks near the known modulation tones in Fig. 19. The measured Doppler shift on the RF spectrum is 60MHz and the Doppler peak is indicated in Fig. 19 as ω_d . The resolution of the velocimetry is depending on the frequency resolution of the spectrum, $\delta\omega$. Therefore, the velocity resolution can be formalized as $\delta v = (\pm\delta\omega / \omega_0) c$. In this particular simulation, the δv of the MTCW system is 0.4cm/s due to the long time window. In the actual practice, there is an interplay between time window, i.e. velocimetry resolution, and the number of scans one can perform per second in most of the CW lidar systems, in particular FMCW lidar systems, which should be taken into account while configuring the lidar depending on the desired application.

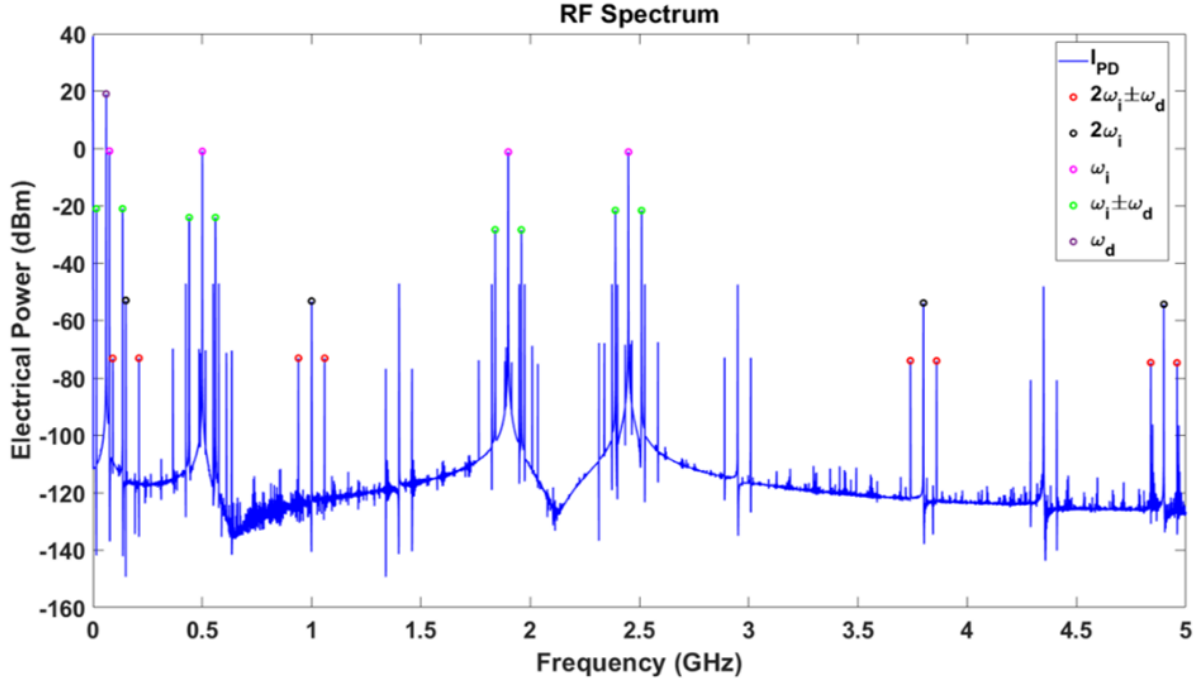


Fig. 19 | RF spectrum of the simulation result of PE-MTCW technique. RF spectrum of the resultant I_{PD} of a target at 50m with 108km/h speed. Each modulation tone, higher-order frequencies, their corresponding Doppler shifts, and the ω_d are indicated on the RF spectrum.

The desired phases are extracted by using the output voltage, V_{out} , generated by the I_{PD} . After performing FFT, the resultant complex V_{out} yields the phase observed at that particular tone in between the interval of $-\pi, \pi$. This process can be further improved by using Bessel filters in the frequency domain to generate the phases of individual tones. At this point, all the variables are found to compute L_m except for the value of n_i in Eq.(4.2). It is not possible to measure the exact number of complete cycles of a modulation tone via the MTCW methodology by looking at the results in a single tone. Hence a triangulation approach is used to generate the exact distance of the target using the individual $\omega_i \pm \omega_d$ phases. It is possible to further enhance the sensitivity of the methodology by employing $2\omega_i \pm \omega_d$ tones, however, these tones will have lower powers compared to $\omega_i \pm \omega_d$.

To find the measurement length, the possible n_i values are swept for each $\omega_i \pm \omega_d$. The highest n_i value belongs to the highest frequency tone with the smallest RF wavelength. The lowest frequency tone will have the lowest value of n_i . In an actual application, it is desired to have a minimum value of $n_i = 1$ within

the maximum measurement range by selecting an appropriate tone frequency, or it is desired to use the time of arrival information of quasi-CW pulses to estimate a coarse range value. The calculated L_m results for the given n_i at the corresponding frequencies are shown in Fig. 20(a). Each frequency has a different repetition length of $2\pi c / \omega_i \pm \omega_d$ as the following, $L_{\omega_1 - \omega_d} = 19.98\text{m}$, $L_{\omega_1 + \omega_d} = 2.22\text{m}$, $L_{\omega_2 - \omega_d} = 68.13\text{cm}$, $L_{\omega_2 + \omega_d} = 53.53\text{cm}$, $L_{\omega_3 - \omega_d} = 16.29\text{cm}$, $L_{\omega_3 + \omega_d} = 15.29\text{cm}$, $L_{\omega_4 - \omega_d} = 12.54\text{cm}$, and $L_{\omega_4 + \omega_d} = 11.94\text{cm}$.

To estimate the actual L_m , first, a data matrix $M_{k,l}$ is generated such that $M_{k,l} = k(2\pi c / \omega_i \pm \omega_d) + L_0^{\omega_i \pm \omega_d}$, where $L_0^{\omega_i \pm \omega_d}$ is computed by using the equations in Table 1, $k = 1, 2, \dots, n_{i-\max}$, and $l = 2N$. For illustration purposes, it is assumed that the desired measurement range is within $n_{i-\max} = 500$ for the highest frequency tone. Since, for other lower frequencies, $n_{i-\max}$ will be lower for the same target range, it is not needed to fill values of the matrix for the estimated length $L_k^i = k(2\pi c / \omega_i \pm \omega_d) + L_0 > L_{\max}$. Since $\omega_4 + \omega_d$ will yield a better resolution due to its smaller repetition length, the last column of $M_{k,l}$ is set to the estimated L_m at each n_i , which will be used as the finest length resolution. The rest of the columns are filled in the same manner. However, range estimation values presented in new columns are selected in a manner to closely match the estimated L_m values in the last column. Since as the tone frequency decrease, $2\pi c / (\omega_i \pm \omega_d)$ will repeat itself less often, hence the repetitive terms are obtained in the previous columns, as illustrated in a sample matrix in Fig. 20(b).

After establishing the $M_{k,l}$, the standard deviation of each row is calculated and stored in the array σ_k as

$$\sigma_k = \sqrt{\frac{\sum_{i=1}^l (M_{k,i} - \overline{M}_k)^2}{l}}. \text{ Here, } \overline{M}_k \text{ stands for the mean of the } k^{\text{th}} \text{ row. Then the first column of } M_{k,l} \text{ is}$$

matched with σ_k to find the standard deviation at the corresponding L_m . The length where the minimum σ_k is found will yield the closest target range. Fig. 21 illustrates the σ_k values for a target at 50m away. The minimum σ_k corresponds to a target at $L_m = 50.0091\text{m}$ that deviates 0.91cm from the actual. Here the error range is dictated by the time resolution δt of the detected signal as $\delta L = (\pm \delta t \times c) / 2$.

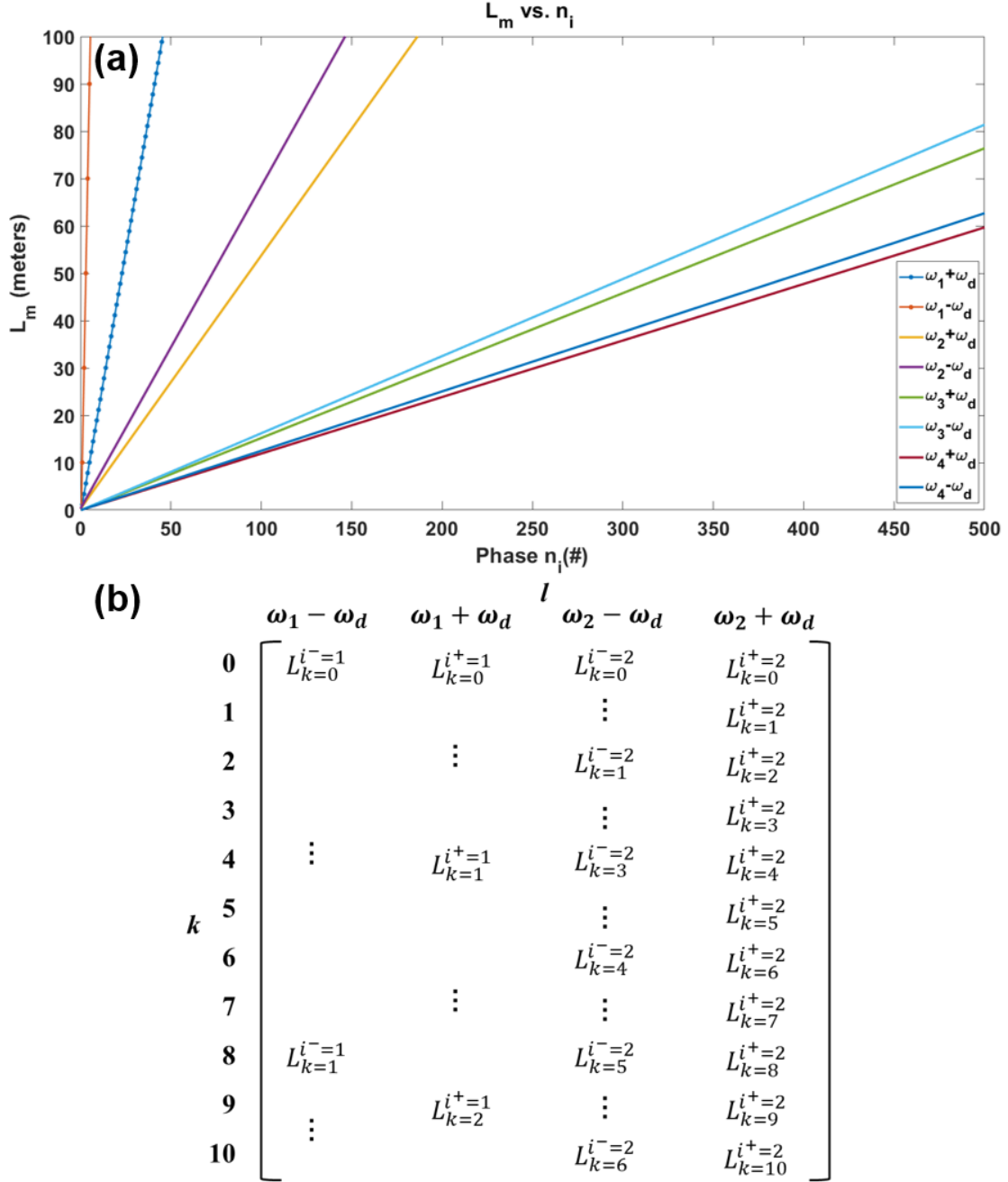


Fig. 20 | Measured distance by each Doppler-shifted frequency. (a) Measurement length results, $L_k^{\omega_i \pm \omega_d}$, after sweeping the n_i up to 500 for each $\omega_i \pm \omega_d$ (b) Representation of the first 11 rows of the $M_{k,l}$ matrix with 2 RF modulation tones with the calculated $L_k^{\omega_i \pm \omega_d}$ values. Blank spaces are repeating terms for $k < 10$.

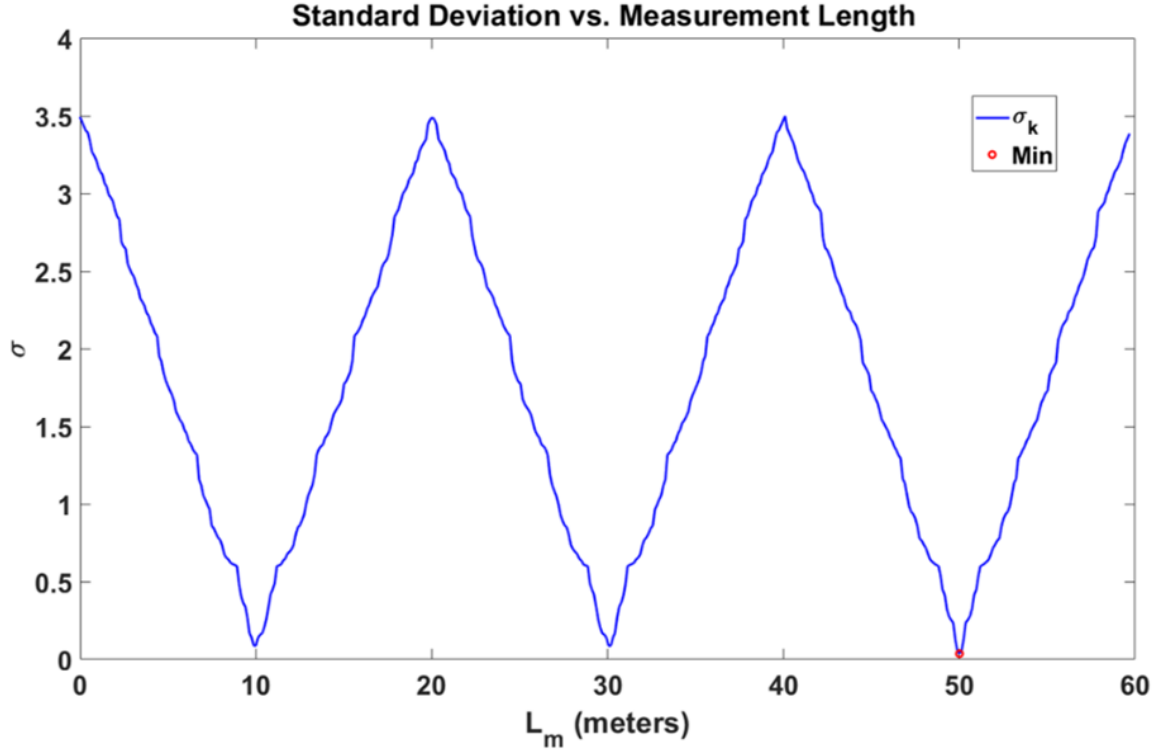


Fig. 21 | Result of the triangulation algorithm based on simulation results. σ_k with respect to L_m to find the distance of the target via triangulation. L_m set to 50m with a target speed of 108km/h. The minimum σ_k value is indicated in the figure.

Detecting targets that are further than the λ_{RF-max} should be evaluated by considering the fact that the minimum standard deviation point repeats itself for every distance of $L_{rep} = 2\pi c / \omega_{gcd}$, where ω_{gcd} is the greatest common divisor of $\omega_i \pm \omega_d$ frequencies. In particular, for applications like aerial imaging or remote sensing through satellites or flying devices, a quasi-CW approach should be utilized to generate long pulses with high peak power and RF modulations on top of them to mitigate the cyclic behavior. In a such method, the quasi-CW pulses offer the time of arrival measurements to capture coarse range measurements, while RF modulations on top of the long pulse facilitate more precise range and velocity measurements. Therefore, the span of n_i will be limited due to the time gating of the modulated pulses. At each interval, the selected n_i range will yield a single solution based on the measured tone frequencies and phases. In our theoretical model, L_{rep} is found to be ~ 60 m, which corresponds to the greatest common divisor of all $\omega_i \pm \omega_d$ terms that is 5MHz. As a result, the minimum standard deviation repeats itself at 50m, 110m,

170m, ... etc. Hence, selecting tone frequencies in a way that the greatest common divisor of all $\omega_i \pm \omega_d$ terms is as small as possible will increase the L_{rep} .

4.4. Experimental Results

4.4.1. Dynamic target results

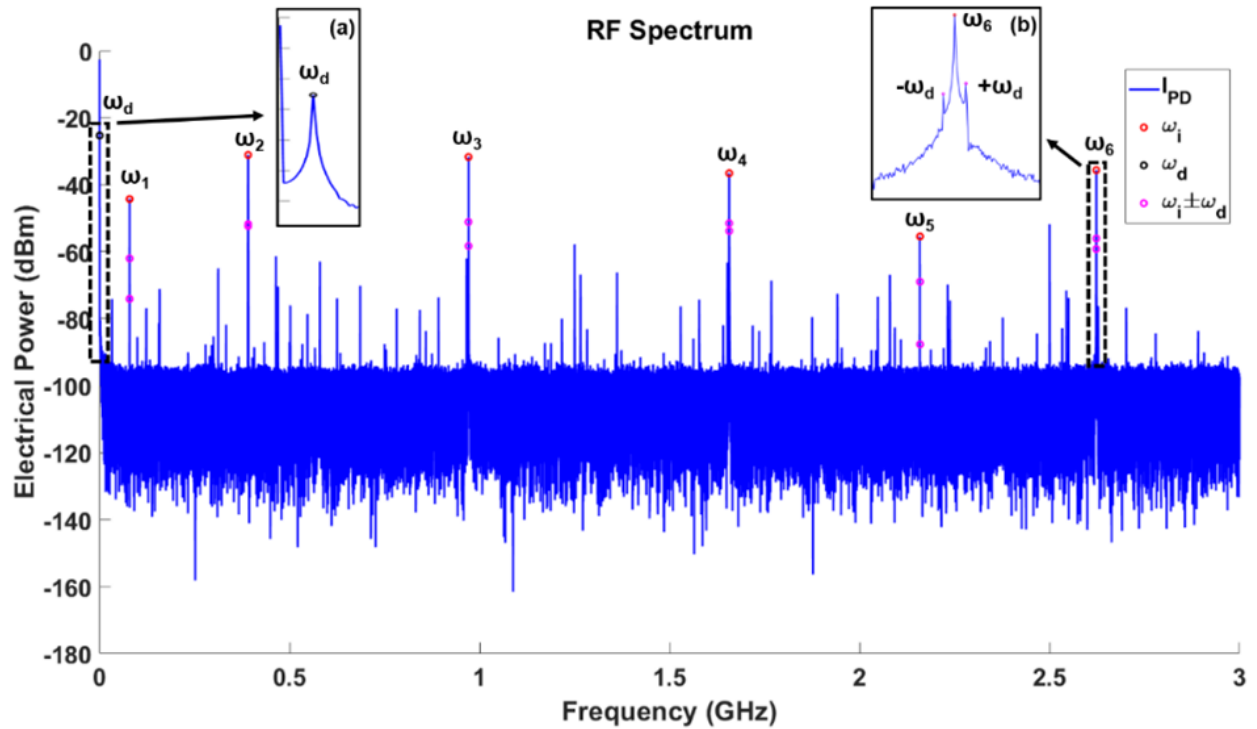


Fig. 22 | Measured resultant RF spectrum of the target moving with $\sim 8\text{cm/s}$. 6 RF modulation frequencies are indicated on the spectrum. Insets (a) magnified Doppler spike near the baseband at 105kHz, (b) magnified ω_6 and its corresponding $\omega_6 \pm \omega_d$.

To prove the concept in the experimental domain, the test bench in Fig. 12 is used. The target is set to move with $\sim 8\text{cm/s}$ and the 40cm long stage is placed 90cm away from the PE-MTCW lidar. A region is selected on the stage for data acquisition that corresponds to a distance of 110-115cm from the detector since the actual distance of the target cannot be measured due to the movement of the target with an integrated PToF lidar for comparison and verification. The data is acquired while the target is moving through this predetermined location on the translational stage at a constant speed. A narrow linewidth 1550nm laser is modulated by 6 RF modulation tones at 79, 391, 971, 1657, 2159, and 2623MHz. The L_{ref} is measured to be 3cm and the initial tone phases, ϕ_i , are acquired from the E_{ref} spectrum to normalize the

resultant $\omega_i \pm \omega_d$ phases. The triangulation algorithm is applied to the measured $\omega_i \pm \omega_d$ phases to compute the target distance. The velocity of the target is found using the RF peak near the baseband.

The final measured RF spectrum is presented in Fig. 22. Each ω_i and its corresponding $\omega_i \pm \omega_d$ are labeled on the spectrum as well as the Doppler frequency near the baseband. The measured Doppler spike is at 105kHz which is equal to 8.08cm/s at 1550nm with a ± 0.8 cm/s accuracy due to the frequency resolution of the measurement setup. For ranging, data matrix $M_{k,l}$ is generated by setting l to 12 and k to 30. The phase of $\omega_6 + \omega_d$ is used as the reference point to maximize resolution. The final σ_k and the minimum standard deviation point are shown in Fig. 23. The L_m is measured as 111.9cm which is within the predetermined measurement range. The expected ranging resolution, δL , is ± 0.75 cm based on the temporal resolution after interpolation of the acquired data. The minimum σ_k is 0.15, where the minimum standard deviation should be zero in an ideal noiseless system. It is expected to have a nonzero standard deviation due to the phase noise of the source and detector noises.

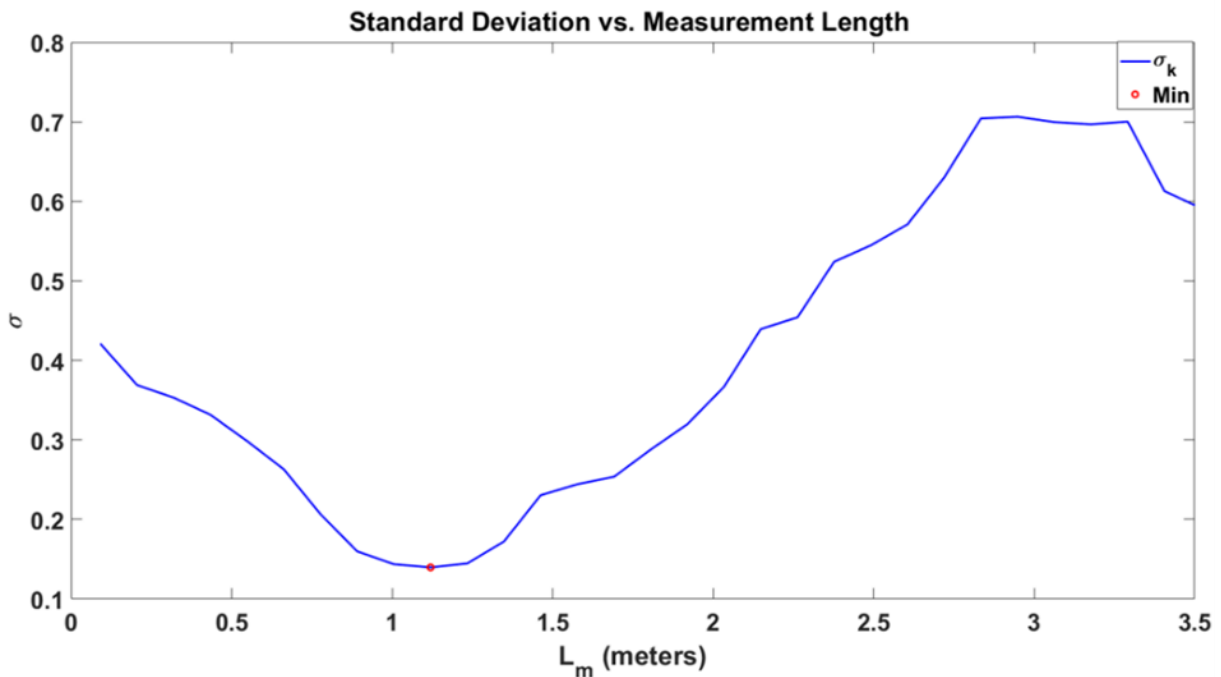


Fig. 23 | Experimental triangulation result of the PE-MTCW lidar. σ_k with respect to L_m to find the distance of the target via triangulation. The minimum σ_k value is indicated in the figure at $L_m = 111.9$ cm.

4.5. Analysis

4.5.1. Lidar parameters

The parameters for the PE-MTCW technique are the same as the AB-MTCW lidar since the technique is based on the AB-MTCW architecture. To summarize, the unambiguous range is related to the greatest common divisor of the selected RF tones as indicated in Eq.(3.10). Moreover, the range resolution is related to the phase resolution of the system, which is defined by the time resolution of the measurement electronics, in particular dt . The range resolution can be formalized as in Eq.(4.3), which is inherently related to the bandwidth of the lidar architecture.

$$\delta L = c \times dt \quad (4.3)$$

In terms of precision, the minimum standard deviation point can create an understanding of the measurement. For instance, in the experiment, the minimum σ_k is 0.15, where the minimum standard deviation should be zero in an ideal noiseless system. If the acquired phases are absolute, the common solution should converge to the same value, and thus should yield a 0 σ_k . It is expected to have a nonzero standard deviation due to the phase noise of the source and detector noises. In addition, the SNR of the system should be similar to FMCW as in Eq.(2.26) for high echo signal power cases, whereas the SNR should follow the AB-MTCW formalism as in Eq.(3.13) for low optical power levels due to the power adjustment requirements of the reference arm.

In terms of range accuracy, the main limitation arises from the laser phase noise as well as the jitter, RF tone frequency drifts, spurious-free dynamic range, potential cross-talks, etc. These parameters are related to the lidar system specifications as in the other lidar techniques.

4.5.2. Challenges

As mentioned in Section 3.5.2, the challenges for the AB-MTCW system persists for the PE-MTCW, except for the Doppler shift limitations. Similarly, the phases of the initial modulation frequencies should be known in the system. This can be realized by phase-locking of the RF tones and pre-calibration of the system before operation.

In contrast to the AB-MTCW, the minimum standard deviation point will repeat itself in every L_{rep} , which is defined by $L_{rep} = 2\pi c / \omega_{gcd}$. It is possible to extend the unambiguous range by introducing low-frequency RF modulations to the MZM along with the high-frequency components, or it is possible to introduce a quasi-CW pulsation on the modulated beam to employ time gating to acquire the limits of the n_i .

Chapter 5

Phase-Based Multi-Tone

Continuous-Wave Lidar

5. PHASE-BASED MULTI-TONE CONTINUOUS-WAVE LIDAR

5.1. Motivation

The limitations and challenges of the AB-MTCW lidar are described in the previous section. The fundamental limitation of the AB-MTCW lidar is the power balance requirement between the reference and measurement arms. Similarly, the maximum measurable distance is limited to the coherence length of the laser as in $L_{\max} = L_{\text{coh}} / 2 = c / 2\pi\Delta f_0$. In addition, achieving single-shot measurements without any kind of phase, frequency, or amplitude sweeping is always the primary objective. Therefore, to address the issues in the AB-MTCW and PE-MTCW lidar, the lidar architecture, as well as the post-processing algorithms, are modified to perform simultaneous single-shot ranging and velocimetry without any form of sweeping, which has the capability of yielding high-resolution results beyond the coherence length limitations of the CW laser.

To do so a fraction of the source laser before encoding the RF tones at the amplitude modulator is used, along with proper algorithms in a new experimental setup. Such a method paves the way to annihilate the requirement of power balance between signal and LO as in the AB-MTCW architecture. It is possible to come up with a solution that removes the common noise terms and impact of coherence length limitations. In this technique, which is called the Phase-Based Multi-Tone Continuous Wave lidar (PB-MTCW), instead of employing any form of frequency, phase, or amplitude sweeping, a CW laser is modulated with multiple phase-locked radio-frequency (RF) tones to generate stable sidebands using a Mach-Zehnder modulator (MZM) under a linear modulation configuration. Then the phases of individual tones are utilized that are encoded in the echo signal after heterodyning with the unmodulated local oscillator, similar to the PE-MTCW technique. Since the absolute value of the phase differences between the reference, i.e. local oscillator, and the echo signal are impaired due beyond the coherence length of the laser, the phase differences between RF tones are utilized which are free from common noise terms. The phase difference of the individual sidebands reveals the target distance, while the acquired Doppler shift produces the target velocity, simultaneously.

5.2. Working Principle

5.2.1. Concept

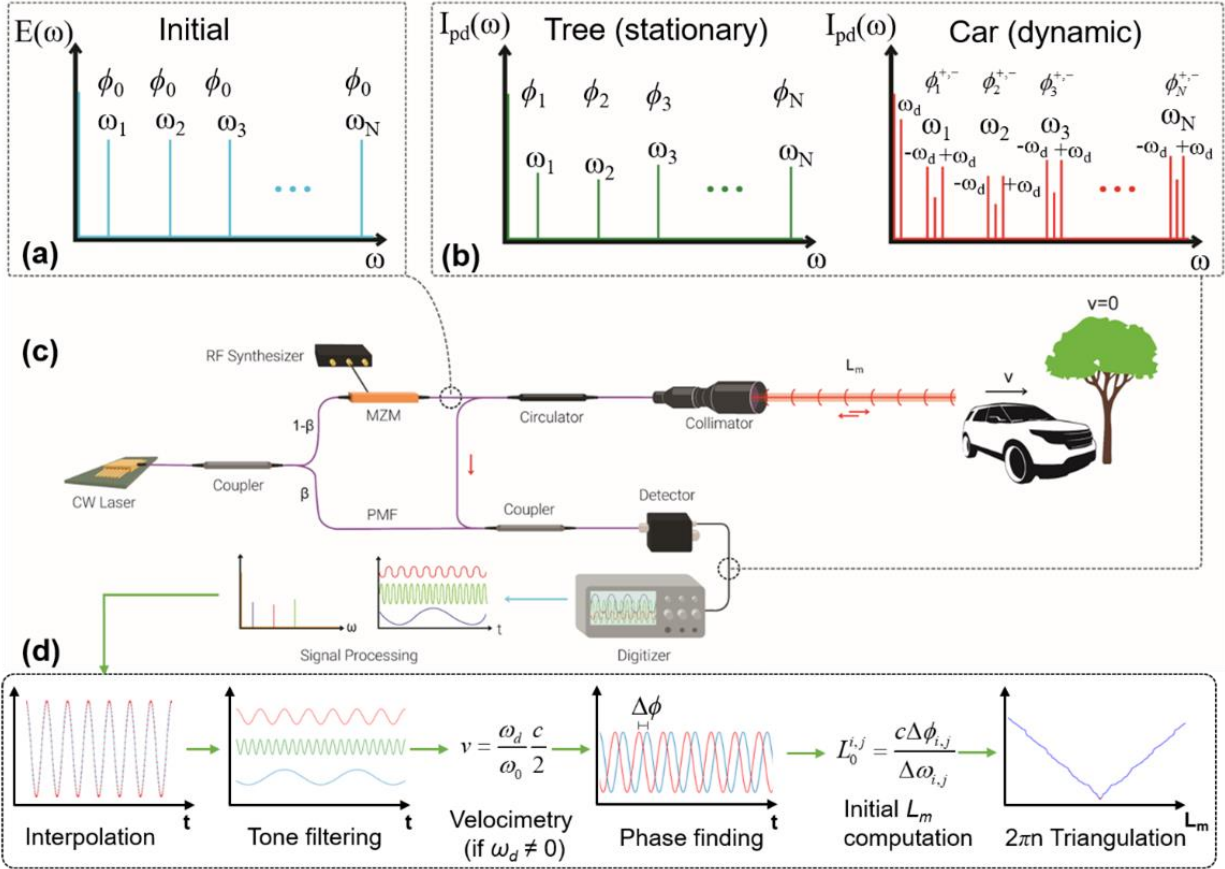


Fig. 24 | Working principle of the Phase-Based Multi-Tone Continuous Wave lidar. (a) The electric field spectrum of the laser after modulation with $\omega_1, \omega_2, \omega_3, \dots, \omega_N$ frequencies. (b) The resultant photocurrent (I_{pd}) spectra after acquiring the echoed signal from a stationary tree and a car in-motion with a velocity (v), respectively. (c) Schematic design of the PB-MTCW lidar. (d) The flowchart of the signal processing.

In PB-MTCW lidar configuration, a continuous-wave laser is split into two through a fused fiber coupler with a coupling coefficient of β as displayed in Fig. 24(c) [83,88,90]. All the fibers are polarization-maintaining (PMF) to inhibit potential polarization mismatches. The measurement branch of the system is further modulated by an MZM with multiple RF tones generated by phase-locked RF synthesizers operating with a common clock. The electric field spectrum of the laser after modulation with $\omega_1, \omega_2, \omega_3, \dots, \omega_N$ frequencies by a Mach-Zehnder modulator (MZM) before leaving the collimator. Each tone has an initial phase of ϕ_0 before ranging, which is shown in Fig. 24(a). The modulated light is then fed to a circulator that

is followed by a collimator for both transmission and reception. The collected light is sent to a second coupler for heterodyning with the local oscillator branch, which is further connected to a high-speed photodetector. The resultant photocurrent (I_{pd}) spectra after acquiring the echoed signal from a stationary tree and a car in motion with a velocity (v), respectively as depicted in Fig. 24(b). The tones accumulate different phases of $\phi_1, \phi_2, \phi_3, \dots, \phi_N$ with respect to the target distance L_m . In the case of the dynamic target, the optical carrier and the sidebands realize a Doppler frequency shift of ω_d . $\phi_t^{+, -}$ represents the acquired phases of each Doppler-shifted modulation. The flowchart of the signal processing is illustrated in Fig. 24(d), which starts with the interpolation of the time-domain data. Each modulation tone or shifted peak is filtered out for post-processing. If $\omega_d \neq 0$, the target speed is computed, then the individual tone phases are generated. Using the phase difference between the tones, the initial target distance ($L_0^{i,j}$) is computed, which is followed by the triangulation of the actual target distance with multiple $L_0^{i,j}$ to achieve ranging.

5.2.2. Theoretical model of a static target

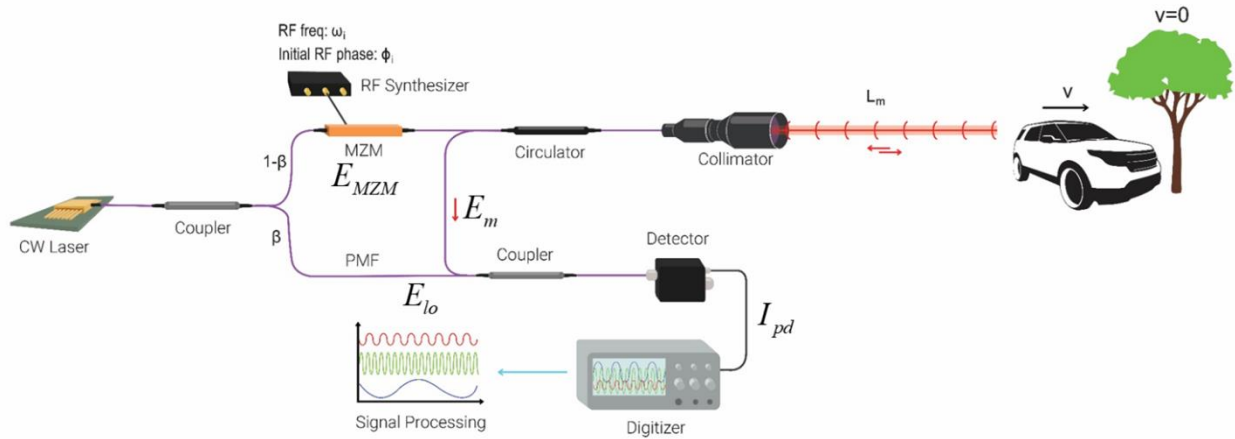


Fig. 25 | Theoretical model parameters on the PB-MTCW configuration. E_{MZM} is the electric field of the MZM output and E_m is the electric field of the echo signal. E_{LO} represents the electric field of the local oscillator. L_m is the measurement range and v is the speed of a dynamic target.

The electric fields of the local oscillator (E_{LO}) and the echo signal (E_m) are indicated on the PB-MTCW schematic in Fig. 25, as well as the transmission electric field after modulator (E_{MZM}) and the resultant photocurrent I_{pd} . The output of the CW laser is formulated as $E_{laser} = A_0 \exp(j\omega_0 t + j\phi_0)$, where $A_0 = \sqrt{P_{out}}$ is the amplitude, ω_0 is the angular frequency and ϕ_0 is the initial phase of the electric field generated by the

source laser. The laser is then split into two by a coupler with a $\beta/(1-\beta)$ power splitting ratio. The unmodulated local oscillator is formulated as in Eq.(5.1) by also considering fiber attenuation (α_f) and laser phase noise ($\phi_n(t - \tau_{LO})$), where τ_{LO} is the propagation time in the local oscillator branch.

$$E_{LO} = A_0 \alpha_f \sqrt{\beta} \exp(j\omega_0 t + j\phi_0 + j\phi_n(t - \tau_{LO})) \quad (5.1)$$

For simplicity, the phase induced to the optical carrier due to fiber path lengths is neglected. The light in the upper branch is modulated via a Mach-Zehnder electro-optic modulator (MZM). N number of phase-locked RF tones that have A_i^{RF} amplitude, ω_i angular frequency, and ϕ_i^{RF} initial phases generate the E-field as $E_{RF} = \sum_{i=1}^N A_i^{RF} \cos(\omega_i t + \phi_i^{RF})$ that is further fed to the MZM for modulation. Assuming a balanced MZM

under push-pull configuration, the field transfer function can be formalized as $\cos\left(\frac{0.5\pi V_{in}}{V_\pi}\right)$, and at the

quadrature bias, the resultant voltage will be $V_{in} = \frac{V_\pi}{2} + E_{RF}$. As a result, the modulation equation will have

the formalism of $\cos\left(\frac{\pi}{4} + \frac{\pi}{2V_\pi} E_{RF}\right) = \frac{1}{\sqrt{2}} \left[\cos\left(\frac{\pi}{2V_\pi} E_{RF}\right) - \sin\left(\frac{\pi}{2V_\pi} E_{RF}\right) \right]$. The modulation depth of the

MZM can be represented as $m = \frac{\pi A_i^{RF}}{V_\pi}$. Now, assuming a linear modulation with relatively low modulation

depth to achieve the E-field after MZM by using $E_{MZM} = \frac{E_{laser}}{\sqrt{2}} - \frac{E_{laser}}{\sqrt{2}} \frac{\pi}{V_\pi} E_{RF}$ that is shown in Eq.(5.2).

$$E_{MZM} = \frac{A_0}{\sqrt{2}} \alpha_f \sqrt{1-\beta} \exp(j\omega_0 t + j\phi_0) - \frac{mA_0}{4\sqrt{2}} \alpha_f \sqrt{1-\beta} \sum_{i=1}^N \left(\exp\left[j(\omega_0 + \omega_i)t + j(\phi_0 + \phi_i^{RF}) \right] + \exp\left[j(\omega_0 - \omega_i)t + j(\phi_0 - \phi_i^{RF}) \right] \right) \quad (5.2)$$

After the formation of the sidebands, one can include the fiber path length traveled by the light to the total propagation distance, L_m , i.e. $L_m = L_{free} + n_{PMF} L_{fiber}$, where L_{free} is the light propagation in free space, n_{PMF} is the refractive index of the polarization-maintaining fiber, and L_{fiber} is the total fiber path length after MZM. Each modulation tone will accumulate a phase based on the L_m and speed of light, c , as

$\phi_i^{range} = \frac{2L_m}{c} \omega_i$. The E-field of the echo signal is represented in Eq.(5.3) after defining the linear attenuation

coefficient (α_m) related to the potential scattering, collection, and/or back coupling losses.

$$E_m = \frac{A_0}{2\sqrt{2}} \alpha_m \alpha_f \sqrt{1-\beta} \exp \left[j\omega_0 t + j\phi_0 + j\omega_0 \frac{2L_m}{c} + j\phi_n(t-\tau) \right] - \frac{mA_0}{4\sqrt{2}} \alpha_m \alpha_f \sqrt{1-\beta} \sum_{i=1}^N \left(\begin{aligned} &\exp \left[j(\omega_0 + \omega_i)t + j\phi_0 + j\phi_i^{RF} + j(\omega_0 + \omega_i) \frac{2L_m}{c} + j\phi_n(t-\tau) \right] \\ &+ \exp \left[j(\omega_0 - \omega_i)t + j\phi_0 - j\phi_i^{RF} + j(\omega_0 - \omega_i) \frac{2L_m}{c} - j\phi_n(t-\tau) \right] \end{aligned} \right) \quad (5.3)$$

Here, $\tau = 2L_m / c$ is the time of propagation and $\phi_n(t-\tau)$ is the laser phase noise related with τ that is when the laser beam first left the MZM. Since the defined phase noise term is related to the carrier, the same noise term will be carried by every modulation frequency.

The E_m and E_{LO} are combined via a combiner and the photocurrent is achieved based on the square-law detector as $I_{pd} = R(E_m + E_{LO}) \cdot (E_m + E_{LO})^*$. The final I_{pd} after the interference of the local oscillator with the echo signal from a stationary target is shown in Eq.(5.4), where the laser phase noise difference of E_m and E_{LO} is represented as $\Phi(t, \tau, \tau_{LO}) = \phi_n(t - \tau_{LO}) - \phi_n(t - \tau)$ [91].

$$I_{pd} = RA_0^2 \alpha_f^2 \beta + \frac{3RA_0^2 \alpha_m^2 \alpha_f^2 (1-\beta)}{16} + \frac{RA_0^2 \alpha_m \alpha_f^2 \sqrt{\beta} \sqrt{1-\beta}}{\sqrt{2}} \cos \left(\omega_0 \frac{2L_m}{c} + \Phi(t, \tau, \tau_{LO}) \right) - \frac{RmA_0^2 \alpha_m \alpha_f^2 \sqrt{\beta} \sqrt{1-\beta}}{2\sqrt{2}} \left[\begin{aligned} &\sum_{i=1}^N \cos \left(\omega_i t + (\omega_0 + \omega_i) \frac{2L_m}{c} + \phi_i^{RF} + \Phi(t, \tau, \tau_{LO}) \right) \\ &+ \sum_{i=1}^N \cos \left(\omega_i t - (\omega_0 - \omega_i) \frac{2L_m}{c} - \phi_i^{RF} - \Phi(t, \tau, \tau_{LO}) \right) \end{aligned} \right] + \frac{RmA_0^2 \alpha_m^2 \alpha_f^2 (1-\beta)}{8} \left[\sum_{i=1}^N \cos \left(\omega_i t + \omega_i \frac{2L_m}{c} + \phi_i^{RF} \right) + \sum_{i=1}^N \cos \left(\omega_i t + \omega_i \frac{2L_m}{c} - \phi_i^{RF} \right) \right] + \frac{Rm^2 A_0^2 \alpha_m^2 \alpha_f^2 (1-\beta)}{8} \sum_{i=1}^N \cos \left(2\omega_i t + \omega_i \frac{4L_m}{c} \right) \quad (5.4)$$

5.2.3. Theoretical model of a dynamic target

In the case of a dynamic target, the backscattered light will realize a Doppler frequency shift of ω_d . The Doppler shift is related to the target speed as $\omega_d = (2v/c)\omega_0$, where v is the target velocity in the direction of laser propagation. Similarly, each modulation frequency realizes a Doppler shift ω_d^i , as well. The returned signal E-field after collection is shown in Eq.(5.5).

$$E_m = \frac{A_0}{2\sqrt{2}} \alpha_m \alpha_f \sqrt{1-\beta} \exp(j(\omega_0 + \omega_d)t + j\omega_0 \frac{L_m}{c} + j(\omega_0 + \omega_d) \frac{L_m}{c} + j\phi_0 + j\phi_n(t-\tau))$$

$$- \frac{mA_0}{4\sqrt{2}} \alpha_m \alpha_f \sqrt{1-\beta} \sum_{i=1}^N \left(\begin{array}{l} \exp \left[\begin{array}{l} j(\omega_0 + \omega_i + \omega_d + \omega_d^i)t + j(\omega_0 + \omega_i) \frac{L_m}{c} \\ + j(\omega_0 + \omega_i + \omega_d + \omega_d^i) \frac{L_m}{c} + j(\phi_0 + \phi_i^{RF}) + j\phi_n(t-\tau) \end{array} \right] \\ + \exp \left[\begin{array}{l} j(\omega_0 - \omega_i + \omega_d - \omega_d^i)t + j(\omega_0 - \omega_i) \frac{L_m}{c} \\ + j(\omega_0 - \omega_i + \omega_d - \omega_d^i) \frac{L_m}{c} + j(\phi_0 - \phi_i^{RF}) + j\phi_n(t-\tau) \end{array} \right] \end{array} \right) \quad (5.5)$$

The forward propagating and backscattered light acquire different phases during their propagation due to changes in the carrier and modulation frequencies. Since $\omega_0 \gg \omega_i$ it is possible to assume $\omega_d + \omega_d^i \approx \omega_d - \omega_d^i \approx \omega_d$. Unless the target is moving at extreme velocities, this assumption is always true for most practical applications. Therefore, the resultant I_{pd} of a moving target is given in Eq.(5.6).

$$I_{pd} = R\beta A_0^2 \alpha_f^2 + \frac{R(1-\beta)A_0^2 \alpha_m^2 \alpha_f^2}{8} + \frac{Rm(1-\beta)A_0^2 \alpha_m^2 \alpha_f^2}{16}$$

$$+ \frac{Rm\sqrt{\beta}\sqrt{(1-\beta)}A_0^2 \alpha_m^2 \alpha_f^2}{\sqrt{2}} \cos\left(\omega_d t + \frac{2L_m}{c}\omega_0 + \frac{L_m}{c}\omega_d + \Phi(t, \tau, \tau_{LO})\right)$$

$$- \frac{Rm(1-\beta)A_0^2 \alpha_m^2 \alpha_f^2}{8} \sum_{i=1}^N \cos\left(\omega_i t + \frac{2L_m}{c}\omega_i + \phi_i^{RF}\right) + \frac{Rm(1-\beta)A_0^2 \alpha_m^2 \alpha_f^2}{16} \sum_{i=1}^N \cos\left(2\omega_i t + \frac{4L_m}{c}\omega_i\right)$$

$$- \frac{Rm\sqrt{\beta}\sqrt{(1-\beta)}A_0^2 \alpha_m^2 \alpha_f^2}{2\sqrt{2}} \sum_{i=1}^N \cos\left((\omega_i + \omega_d)t + \frac{2L_m}{c}(\omega_0 + \omega_i) + \frac{L_m}{c}\omega_d + \phi_i^{RF} + \Phi(t, \tau, \tau_{LO})\right)$$

$$- \frac{Rm\sqrt{\beta}\sqrt{(1-\beta)}A_0^2 \alpha_m^2 \alpha_f^2}{2\sqrt{2}} \sum_{i=1}^N \cos\left((\omega_i - \omega_d)t - \frac{2L_m}{c}(\omega_0 - \omega_i) - \frac{L_m}{c}\omega_d - \phi_i^{RF} - \Phi(t, \tau, \tau_{LO})\right) \quad (5.6)$$

5.2.4. Post-processing

Here, the goal is to develop an algorithm that can calculate the phase and frequency information independent of common noise terms, and then extract the velocity and range of the target. In the case of dynamic targets, Eq.(5.7) can be used to define a single tone.

$$A_i \cos \left((\omega_i \pm \omega_d)t \pm \frac{2L_m}{c} (\omega \pm \omega_i) \pm \frac{L_m}{c} \omega_d \pm \phi_i^{RF} \pm \Phi(t, \tau, \tau_{LO}) \right) \quad (5.7)$$

As is clearly seen from this definition, a frequency shift in the carrier frequency or any tone frequency reveals the Doppler shift, and hence the velocity of the target [80,81]. However, range information is stored in the phase term and it is mixed with noise terms. To eliminate the common noise terms the two of these individual tones at ω_i and ω_j ($i \neq j$) are RF mixed, either electronically or in the digital domain, the resultant intermediate frequency (IF) tone will be $A_i A_j \cos(\Delta\omega_{i,j}t \pm \Delta\phi_{i,j})$, where $\Delta\phi_{i,j}$ and $\Delta\omega_{i,j}$ are the phase and frequency differences of i^{th} and j^{th} tones, respectively. As a result, the common phase and frequency terms related to the optical carrier and the Doppler shift are eliminated with inter-tonal mixing which also eliminates the impact of the coherence length of the laser. Similarly, RF mixing of modulation frequencies obtained from a static target can be defined as in Eq.(5.8), hence eliminating common noise terms.

$$2A_i \cos \left(\frac{2L_m}{c} \omega_0 + \phi_i^{RF} + \Phi(t, \tau, \tau_{LO}) \right) \cos(\omega_i t + \frac{2L_m}{c} \omega_i) \quad (5.8)$$

After the RF mixing, the phase of IF tones will be free from phase and the amplitude noise of the source and reveal only the range information of the target: $L_m = (2\pi n + \Delta\phi_{i,j})c / \Delta\omega_{i,j}$, where n is an integer. As a result, the PB-MTCW lidar methodology is immune to the phase variations induced by the laser phase noise, and hence it is possible to perform ranging beyond the coherence length of the laser.

The modulo- 2π cyclic behavior of the phase will lead to a periodic range estimation. Similar to global positioning systems that use multiple satellites to triangulate the exact position, the redundancy of multiple agents for accurate range information is needed. Here, multiple RF tones are utilized to pinpoint the value of L_m by using a triangulation algorithm as previously described in Section 4.2.2. In particular, for a given

$\Delta\phi_{i,j}$, which corresponds to $\Delta\omega_{i,j}$ the total length will be $L_m = n_i L^{i,j} + L_0^{i,j}$, where the spatial period is $L^{i,j} = 2\pi c / \Delta\omega_{i,j}$ and the residual length is $L_0^{i,j} = c\Delta\phi_{i,j} / \Delta\omega_{i,j}$ [81]. If the integer value of n_i is swept, the potential L_m values can be computed for each $\Delta\omega_{i,j}$. After concatenating all the possible combinations of L_m into a data matrix $M_{k,l}$, where k is equal to the predefined sweep limit (n_{max}) that is set according to the maximum expected range, and l is the number of available $\Delta\omega_{i,j}$ combinations. The standard deviation of each row is calculated as $\sigma_k = \sqrt{\sum_{r=1}^l (M_{k,r} - \bar{M}_k)^2 / l}$ [81,90], where \bar{M}_k , the mean of the k^{th} row, which yields the minimum σ_k corresponds to the actual target distance L_m as depicted in Fig. 24(d). However, the minimum σ repeats itself at every $L_{rep} = 2\pi c / \omega_{gcd}$, where ω_{gcd} stands for the greatest common divisor of the $\Delta\omega_{i,j}$, such phenomenon is called an unambiguity length in lidar systems [81]. One way of avoiding recursive solution or unambiguity length is the selection of the tones in a fashion to make sure L_{rep} is longer than the maximum expected range. For extremely long measurement lengths, instead of using very low-frequency modulation tones to increase L_{rep} , an introduction of a quasi-CW pulsation will be more advantageous. Not only that such a quasi-CW approach facilitates time gating to generate coarse range information without unambiguity length limitation, but also results in higher signal-to-noise ratio measurements compared to an equal power pure CW approach. This approach along with the post-processing in the PB-MTCW approach is illustrated as a block diagram in Fig. 26.

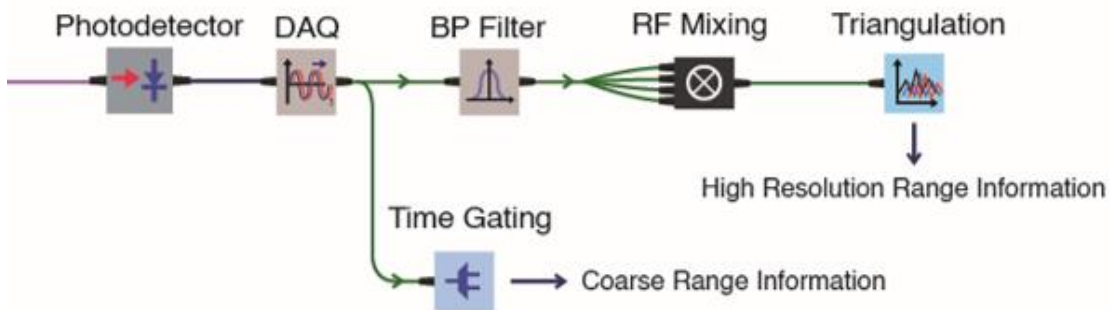


Fig. 26 | Block diagram representing the post-processing after data acquisition. The I_{pd} is first captured by a data acquisition board (DAQ). The coarse range information through quasi-CW pulses is computed via time gating. The data is processed by filtering out individual tones via bandpass (BP) filters. Each tone is RF mixed to yield the intermediate frequencies (IF). The phase and frequency of the final IF tones are used in the triangulation algorithm to generate the high-resolution range information.

5.3. Numerical Verification

5.3.1. Simulation parameters

To configure the PB-MTCW lidar in the simulation domain, a narrow linewidth CW laser is set to operate at a $1\mu\text{m}$ central wavelength. The laser is split into two by setting $\beta = 0.1$ for the local oscillator. The laser beam enters the MZM with a selected modulation depth of $m = 0.01$ to maintain the linearity of the modulator for the measurement branch. The MZM output is sent to the free space for propagation. At the detector, the local oscillator amplitude is set to be $\alpha_{ref} = 1$, while the signal from the target has an attenuation of $\alpha_m = 0.01$ pointing out a 20dB loss due to scattering.

An InGaAs PIN photodetector is assumed in the system with a 1GHz bandwidth based on the selected tone frequencies, and 0.9A/W responsivity in accordance with the commercially available detectors. The load impedance of the detector is set to 50Ω . For simplicity and proof of concept purposes, detector noises such as the shot noise and thermal noise, and laser phase noise are neglected. In the simulation, a $256\mu\text{s}$ time window with about ~ 24 ps temporal resolution (i.e. 2^{23} samples) is used. Eq.(5.1) and Eq.(5.3) are used by setting $\phi_o = \phi_i = 0$ to acquire the resultant I_{PD} . For simplicity, simulations only for static target ranging are performed to demonstrate the impact of the selection of the number of tones.

Two different scenarios are simulated. In the first case, the target is set to be at $L_m = 2\text{m}$ and the ranging is performed while the CW laser is modulated by two different sets of RF modulation tones. The first set of the modulation tones is 500, 700, and 950MHz, and the second set is 20, 500, 670, 700, 890, and 950MHz. The tones are selected in a fashion to prevent any overlaps caused by the second harmonics or cross-beatings. Here, the goal is to numerically demonstrate the impact of the number of tones in the triangulation algorithm.

In the second scenario, 6 modulation tones are used as in the previous case. This time, the measurement range is changed as $L_m = 1\text{m}$, 2m , and 3m to demonstrate the response of the triangulation algorithm for different measurement ranges.

5.3.2. Simulation results

Here, three modulation tones at 500, 700, and 950MHz are used in the first simulation. Then the number of tones is increased to 6 by introducing 20, 670, and 890MHz. As shown in Fig. 27(a), a limited number of tones yield local minima points together with the global minimum. However, increasing the number of tones and utilizing a low modulation tone such as 20MHz with larger L^{ij} will eliminate the potential local minima points due to increasing σ_k values, thus enhancing the triangulation algorithm as depicted in Fig. 27(b). It is important to note that all the frequency tones are harmonics of a 10MHz common source, and they are also all phase-locked to this source.

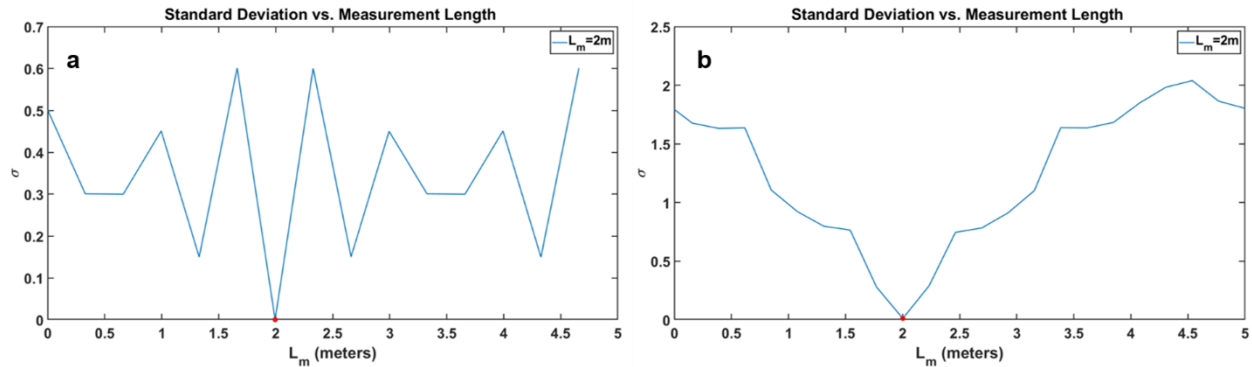


Fig. 27 | Simulation results of stationary target ranging at $L_m = 2m$. (a) Simulation result of ranging after triangulation algorithm using 3 modulation tones at 500, 700, and 950MHz. (b) Simulation result of ranging after triangulation algorithm using 6 modulation tones at 20, 500, 670, 700, 890, and 950MHz.

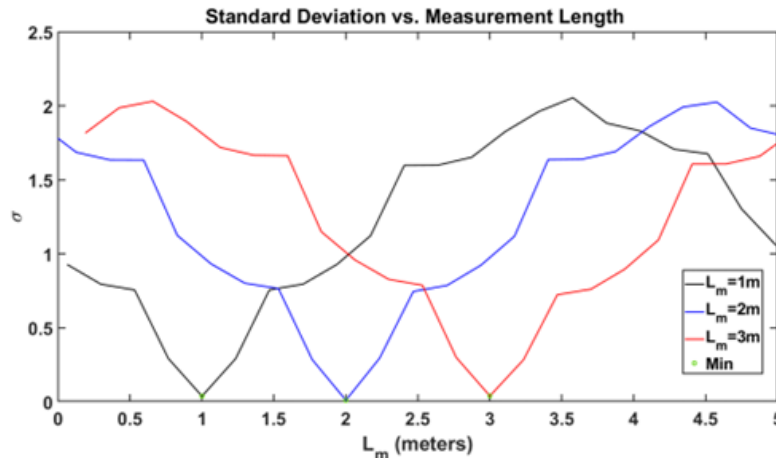


Fig. 28 | Numerical simulation results demonstrate the capability of the triangulation algorithm with 6 modulation tones. Triangulation results for three stationary target positions of $L_m = 1, 2,$ and $3m$ are represented with different colors as black, blue, and red, respectively. The x-axis values of the minimum standard deviation (σ) points correspond to the distances of the target that are indicated with green circles.

To demonstrate the ranging capability of PB-MTCW lidar, 6 RF tones are used and the target position is changed. As demonstrated in Fig. 28, the triangulation algorithm can yield the ranges of three targets at $L_m = 1, 2,$ and 3m . Similar to the first case, the multiple local minima points are eliminated by introducing a low-frequency tone.

5.4. Experimental Verification

5.4.1. Methodology

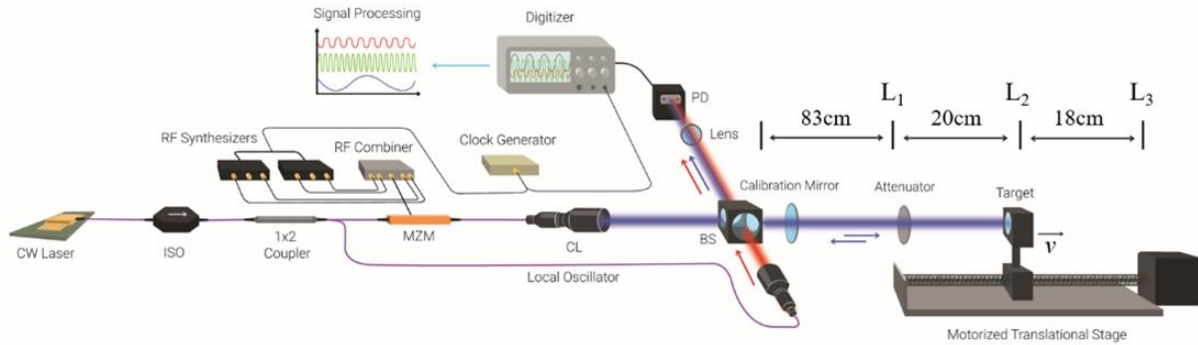


Fig. 29 | Schematic representation of the experimental test bench for PB-MTCW lidar. First, a 1064nm CW laser with $<100\text{kHz}$ linewidth ($L_{\text{coh}} \sim 1\text{km}$), then another 1064nm CW laser with 5.3GHz linewidth ($L_{\text{coh}} \sim 18\text{mm}$) is used to demonstrate ranging further than the laser coherence length. The source is followed by a fiber isolator (ISO), which is connected to a 1×2 fiber coupler to realize the unmodulated local oscillator. The measurement branch is modulated through an MZM with 3RF tones via phase-locked RF synthesizers that are triggered by a clock generator, which also triggers the digitizer. The outputs of both branches are connected to two separate collimators (CL). A free-space optical beamsplitter (BS) is placed in front of both CLs to realize beating after collection on the photodetector (PD). The motorized stage carrying the target reflector is anchored 83cm away from the output facet of the BS. Three measurement distances are $L_1 \sim 83\text{cm}$, $L_2 \sim 103\text{cm}$, and $L_3 \sim 121\text{cm}$ for stationary target ranging. v represents the target speed during dynamic target ranging.

The testbench in Fig. 29 is built by using two different lasers. The highly coherent 1064nm laser diode has $<100\text{kHz}$ linewidth (RPMC Lasers - R1064SB0300PA) and the output optical power is set to $\sim 50\text{mW}$. The low coherence 1064nm laser has a 5.3GHz linewidth (QPhotonics - QFBGLD-1060-100) and operates at the same output levels. All the fibers in the optical system are polarization-maintaining (PMF 980) to prevent polarization mismatching to achieve beating. The CW laser is followed by an isolator and then split into two branches. The local oscillator arm is pigtailed to a collimator. The measurement branch is connected to a high-speed Mach-Zehnder electro-optic modulator (iXblue – NIR-MX-LN series), which is

optimized for 1064nm and has a 30dB extinction ratio. The MZM is biased near the quadrature point that is 1.6V. The modulation tones are set through phase-locked RF synthesizers (Windfreak Technologies - SynthHD (v2)) and their phase matching is realized through a trigger clock of 10MHz provided by a stable frequency generator. The same clock triggered the oscilloscope (Tektronix - MDO34) with 1GHz bandwidth to achieve robust phase measurements. The oscilloscope is set to have a 200 μ s time window with a 5GSa/s sampling rate (10^6 data points). Phase-locked RF frequencies are transmitted to MZM after getting combined in a 4-way RF power splitter (Mini Circuit - ZN4PD1-63HP-S+). The modulated light inside the PMF is brought to free space through an additional collimator. The two collimators are placed in a fashion to form a cross-like configuration. A 1064nm 50/50 beamsplitter is placed at the intersection point of two light beams. Light coupling to the free space high-speed PIN photodetector (Thorlabs – DET08C) is optimized with a microscope lens. The stage carrying the target reflector is placed and aligned ~83cm away from the output facet of the BS. A free-space optical attenuator with a total of ~20dB attenuation is placed on the path of propagation to mimic the potential scattering losses.

Moreover, tone selection plays a vital role in PB-MTCW lidar. Here, a full frequency range from 0Hz to multi GHz (limited by the detection system) is available and there are no dictated carrier frequencies. The tones are selected in a fashion to prevent any second and third harmonic overlaps to maximize the spur-free dynamic range (SFDR). Similarly, intermodulation tones are calculated to forestall possible frequency matchings to preserve the tone phases. Operating close to the linear modulation regime of the MZM reduces the strength of the harmonics, as well. Each RF tone is set to have an amplitude of 90mV_{pp}, hence the corresponding m is 0.07 per tone indicating a close-to-linear operation. Similarly, intermodulation tones are selected to forestall possible frequency matchings to preserve the purity of tone phases and to improve crosstalk and SFDR. Even though a low modulation index is utilized in the experiment, this is not a hard limit for the PB-MTCW operation. Further optimization of the modulation index can be performed by considering the potential SFDR and signal-to-noise ratio (SNR) requirements. Moreover, the tones should be phase-locked, and to achieve this, the tones that are divisible by the trigger frequency of 10MHz are selected. In this experiment, tones are selected as 500, 700, and 950MHz, which satisfy the aforementioned

conditions. The greatest common divisor of these tones is 50MHz which indicates the unambiguity length of the resultant minimum standard deviation point is $\sim 3\text{m}$ to generate the target distance. Since the target is set to $< 3\text{m}$, the unambiguity length didn't alter the results.

After setting the system parameters, PB-MTCW lidar is calibrated before performing the measurements by placing a dummy mirror 6.5cm away from the BS. This calibration allows the system to acquire the initial tone phases due to the initial phase of the RF synthesizers and the fiber path length. The post-processing algorithm generates a pseudo measurement distance at the position of the dummy mirror based on the measured tone phases after averaging the results of 10 trials. This pseudo calibration range is set as the zero-point for the lidar and the ranging measurements are adjusted accordingly by considering the excess 6.5cm, as well.

Data acquisition is further followed by digital signal processing. The measurement data generated by the oscilloscope is interpolated to 2^{23} data points to improve the resolution that eliminates potential distortions during phase calculations since the phases are highly dependent on the time resolution. The time-domain data is converted to frequency domain through a fast Fourier transform to localize the modulation frequencies and get the Doppler frequency if the target is in motion. The algorithm scans the interval between the first tone and the baseband to obtain the Doppler shift. The signal is then further processed by a digital second-order bandpass Butterworth filter with a 1MHz bandwidth around each measured modulation tone. The phase of the filter is compensated by performing zero phase distortion filtering that is processing the input data in both the forward and reverse directions [92]. Reduction of the filter bandwidth per individual tone can further enhance the signal-to-noise ratio of the acquired RF signal based on the relationship between noise and electronic bandwidth. The refined tones are then compared with frequency-matched 0-phase digital cosine signals, which yield the phase of the individual tones. Then the triangulation is performed by setting the sweep length of the integer n_i to 20, which allows the system to span up to $\sim 15\text{m}$.

To prove the proposed concept two separate sets of experimental measurements on dynamic and static targets are performed. In particular, ranging and velocimetry measurements on the dynamic target are

conducted and only the ranging measurements on the static target are demonstrated. Both experiments are performed by using a highly coherent laser with 100kHz linewidth and about 1km corresponding coherence length, and a low coherence laser with 5.3GHz linewidth and about 1.8cm corresponding coherence length. In both cases, a reflector is used as a target that is placed on a motorized translational stage with a maximum speed of 11cm/s in motion. In each experiment, the effective optical path difference between the reference signal and the measurement arm is about 9m, where about 2m of this path difference is in free space and the rest is in the fiber. While this path difference is about 100× smaller than the coherence length of the first laser, it is about 500× larger than the coherence length of the second laser. In existing CW lidars, the second laser should not work at such path difference. 10 consecutive measurements are performed to verify results for each set.

5.4.2. Static target results

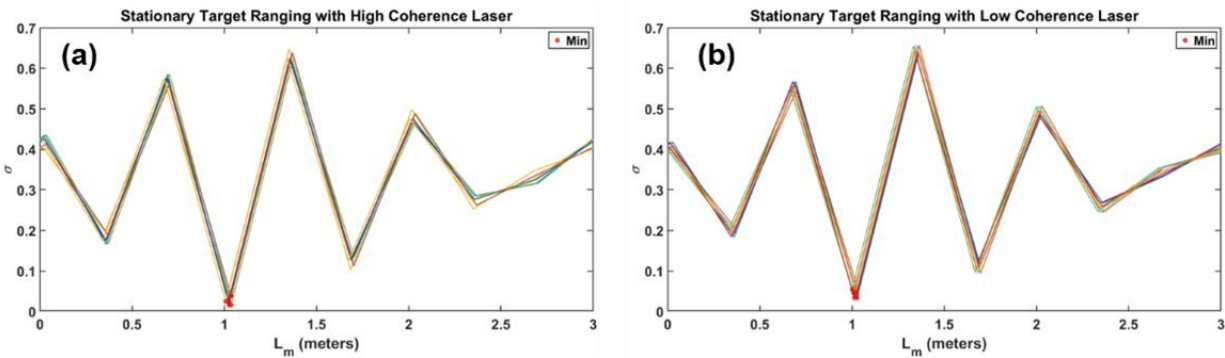


Fig. 30 | Stationary target ranging results with high and low coherence lasers via PB-MTCW technique. (a) Stationary target ranging results of 10 trials while the target is placed at L_2 (~1.03m) using the narrow linewidth laser. (b) Stationary target ranging results at the same position using the low coherence light source.

In the case of stationary target ranging, the reflector is placed at three different locations as L_1 ~83cm, L_2 ~103cm, and L_3 ~121cm as illustrated in Fig. 29. As a sanity check, the coarse measurements of the target distances from the output facet of the BS are performed by using a measuring tape with an estimated accuracy of ± 1 cm. The ranging measurements while the target is placed at L_2 with a high coherence laser source are presented in Fig. 30(a). The mean value of the measured target distance for L_1 , L_2 , and L_3 are 83.13cm, 102.64cm, and 120.44cm, respectively. Hence, the displacements between L_1 - L_2 and L_2 - L_3 are

measured as 19.51cm and 17.81cm. The complete results for stationary target ranging for all the positions and all trials are presented in Fig. 31, as well as in Table 2.

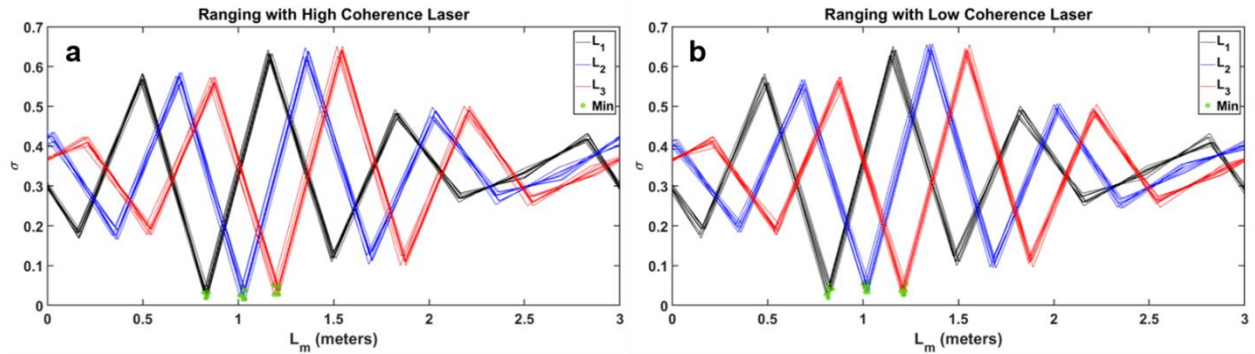


Fig. 31 | Complete stationary target ranging results with high and low coherence lasers via the PB-MTCW technique. Three measurement distances are $L_1 \sim 83\text{cm}$, $L_2 \sim 103\text{cm}$, and $L_3 \sim 121\text{cm}$ for stationary target ranging. (a) Stationary target ranging results of 10 trials for three different positions using the narrow linewidth laser. (b) Stationary target ranging results of 10 trials for three different positions using the temporally incoherent light source.

Table 2 | Ranging results of a stationary target with high and low coherence lasers.

	High Coherence Laser			Low Coherence Laser		
	Range @ L_1 (cm)	Range @ L_2 (cm)	Range @ L_3 (cm)	Range @ L_1 (cm)	Range @ L_2 (cm)	Range @ L_3 (cm)
	82.70	102.59	121.29	83.23	100.85	120.35
	82.31	102.19	118.79	83.94	103.07	122.17
	83.38	101.83	120.62	80.69	102.71	120.62
	83.06	103.66	121.33	82.16	102.67	121.34
	81.99	103.66	120.97	83.23	100.10	120.94
	84.49	103.30	118.43	82.47	101.64	122.45
	83.02	102.19	120.22	81.80	101.29	121.66
	83.06	102.55	120.22	81.80	102.71	119.83
	83.42	103.66	121.29	81.76	100.85	120.90
	83.82	100.76	121.29	81.80	102.04	122.17
Average	83.13	102.64	120.44	82.29	101.79	121.24
Standard deviation	0.72	0.95	1.06	0.95	1.00	0.87

Moreover, the ranging resolution, δL , achievable by an individual tone is defined by the minimum distinguishable phase of the i^{th} tone, $d\phi_i$, as $\delta L \sim \frac{d\phi_i}{\omega_i} c$. Here, $d\phi_i$ depends on various parameters such as sampling rate, jitter, total noises in the system, surface roughness under the spot size, etc. Nonetheless, it is possible to formalize the minimum theoretical resolution by considering a noise-free case, where

$d\phi_i = \omega_i \times dt$, and hence $\delta L = c \times dt$, where dt is the time resolution. After digitally interpolating the data, the final dt becomes $\sim 24\text{ps}$, while it was 200ps before interpolation. Based on $\delta L = c \times dt$, the theoretical minimum resolution is calculated as 0.72cm . The resultant standard deviations for each set of data are $< 1\text{cm}$, which verifies the ranging precision of the PB-MTCW methodology. The small changes during the stationary target measurements can be attributed to the sampling jitter and noise in the system that distorts the $d\phi_i$.

The same set of measurements are performed for the similar three positions using the low coherence laser and the results for L_2 are presented in Fig. 30(b). Here, the mean values of the trials per location are 82.29cm , 101.79cm , and 121.24cm , respectively. Similarly, the standard deviation of the acquired data is $< 1\text{cm}$ for all positions. As a result, this proves that the PB-MTCW lidar is capable of ranging a target placed at $> 500\times$ larger than the coherence length of the CW laser. It is important to note that $500\times$ is limited by the current measurement setup.

5.4.3. Dynamic target results

In the case of the dynamic target, FFT is performed after data acquisition and the resultant RF spectra were scanned with the algorithm to acquire the Doppler frequencies and the instantaneous target speed as demonstrated in Fig. 32(a) and Fig. 32(b) for high and low coherence lasers, respectively. In the case of the low coherence source, it is observed that the RF spikes placed on broadband background due to the linewidth of the laser that is measured to be $\sim 5.3\text{GHz}$. Phase measurements are performed by using narrowband RF filtering of these RF spikes. The measured instantaneous velocity for each trial along with the current position information is tabulated in Table 3.

The measured Doppler shifts vary between $177.5\text{kHz} - 212.5\text{kHz}$ which yields a target speed between $9.44\text{cm/s} - 11.3\text{cm/s}$ when the high coherence laser is employed. Similarly, with the low coherence source, the measured velocities are in the range of $9.18\text{cm/s} - 11.3\text{cm/s}$. Therefore, the measured velocities with high and low coherence lasers are in close agreement that matches the specifications of the motor operating on the stage. The difference is attributed to the fact that the electrical motor accelerates and decelerates very

rapidly due to the limited stage length, thus the reflector speed varies. The velocimetry resolution is associated with the frequency resolution ($d\omega$) of the RF spectrum, which can be formalized as $\delta v = (\pm d\omega / \omega_0) c$. In this experiment, the achieved velocity resolution is $\sim 0.53\text{cm/s}$ due to the 5kHz frequency resolution. In addition, it is possible to resolve the direction of the motion either by using a single-sideband (SSB) modulation instead of a standard dual-sideband modulation, where the direction of the Doppler-shifted modulation tones will yield the motion vector, or by comparing the multiple frames of the same dynamic target in the software domain.

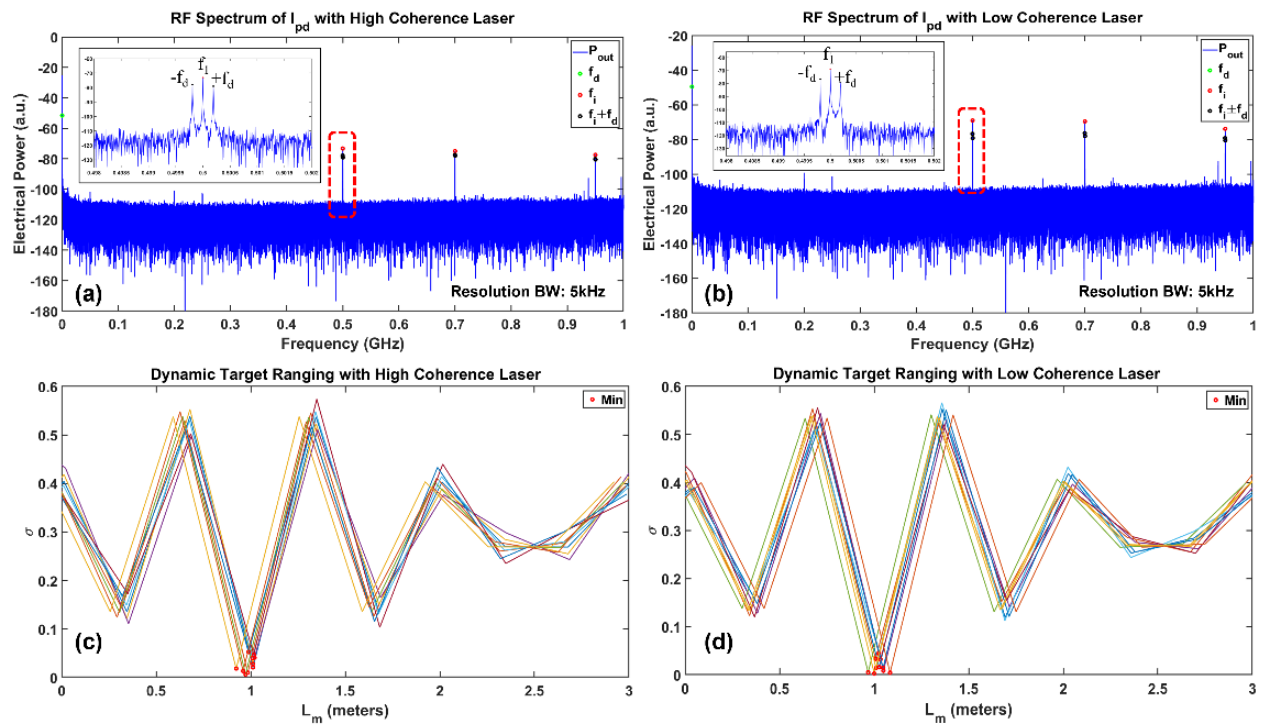


Fig. 32 | Dynamic target ranging results with high and low coherence lasers. (a) Acquired I_{pd} spectrum using the $<100\text{kHz}$ linewidth laser of one measurement with a dynamic target, where the tones and the Doppler-shifted frequencies are indicated. The inset magnifies the vicinity of 500MHz tone displaying the $f_l \pm f_d$ peaks. (b) Similar I_{pd} spectrum using the 5.3GHz linewidth laser. (d) Results of the triangulation algorithm using the highly coherent laser that represents the ranging of the moving target for 10 trials, where the L_m corresponding to the minimum σ yields the target distance. (e) Ranging results using the low coherence laser.

The range triangulations of the moving target by using high and low coherence lasers are illustrated in Fig. 32(c) and Fig. 32(d), respectively. The measurements are performed while the target is moving around a distance that is about 1m away from the beamsplitter, which is also indicated as L_2 (1.03m) in Fig. 29.

Data are captured by using a manual trigger, and hence there is a slight variation in the actual range of the target at each measurement. Among 10 trials with a high coherence laser, range measurements vary between 0.92m and 1.02m. Similar measurements with a low coherence laser yield a range measurement that changes between 0.97m to 1.08m. The ranging resolution is proportional to the time resolution of the system that is computed as ~ 1 cm after interpolation. On the other hand, along with the global minimum, several local minima points appear in the calculation. The response of the triangulation algorithm will be improved by increasing the number of phase-locked RF modulation frequencies, and hence these local minima will disappear.

Table 3 | Simultaneous ranging and velocimetry results of a dynamic target with high and low coherence lasers.

High Coherence Laser		Low Coherence Laser	
Range (cm)	Velocity (cm/s)	Range (cm)	Velocity (cm/s)
101.18	10.51	102.68	10.51
98.44	10.51	100.74	10.24
101.18	9.98	101.01	9.98
102.01	9.44	104.91	10.51
97.29	9.98	96.84	9.98
100.93	10.24	102.52	10.24
101.61	11.31	103.40	9.18
98.83	9.98	104.7	11.31
95.97	10.24	108.45	10.24
92.33	10.51	100.07	9.71

5.5. Quasi-CW integration

5.5.1. Concept

To mitigate the unambiguity range, it is suggested the careful selection of the modulation frequencies with a minimal greatest common divisor. In addition, it is possible to solve this issue by introducing a quasi-CW pulsation to the lidar architecture. The proposed quasi-CW pulse should have a time window that is larger than the period of the lowest frequency modulation tone to extract the phase information. Longer measurement windows are desired to average out the noise if it is feasible in the desired system. For long-range applications such as satellite-based altimetry, kHz level repetition rate can be assumed. With higher peak powers, it is possible to realize echo pulses with more power. Moreover, the duty cycle of the pulse

can be engineered based on the power requirements of the desired application to achieve a satisfactory signal-to-noise ratio (SNR). The utilization of such pulses will not only improve the SNR but also will provide a coarse distance measurement similar to the time-of-flight lidars. This information will provide the boundaries for the $M_{k,l}$ matrix during the scanning of n_i . Hence it will mitigate the potential problems regarding unambiguity range, particularly in long-range applications.

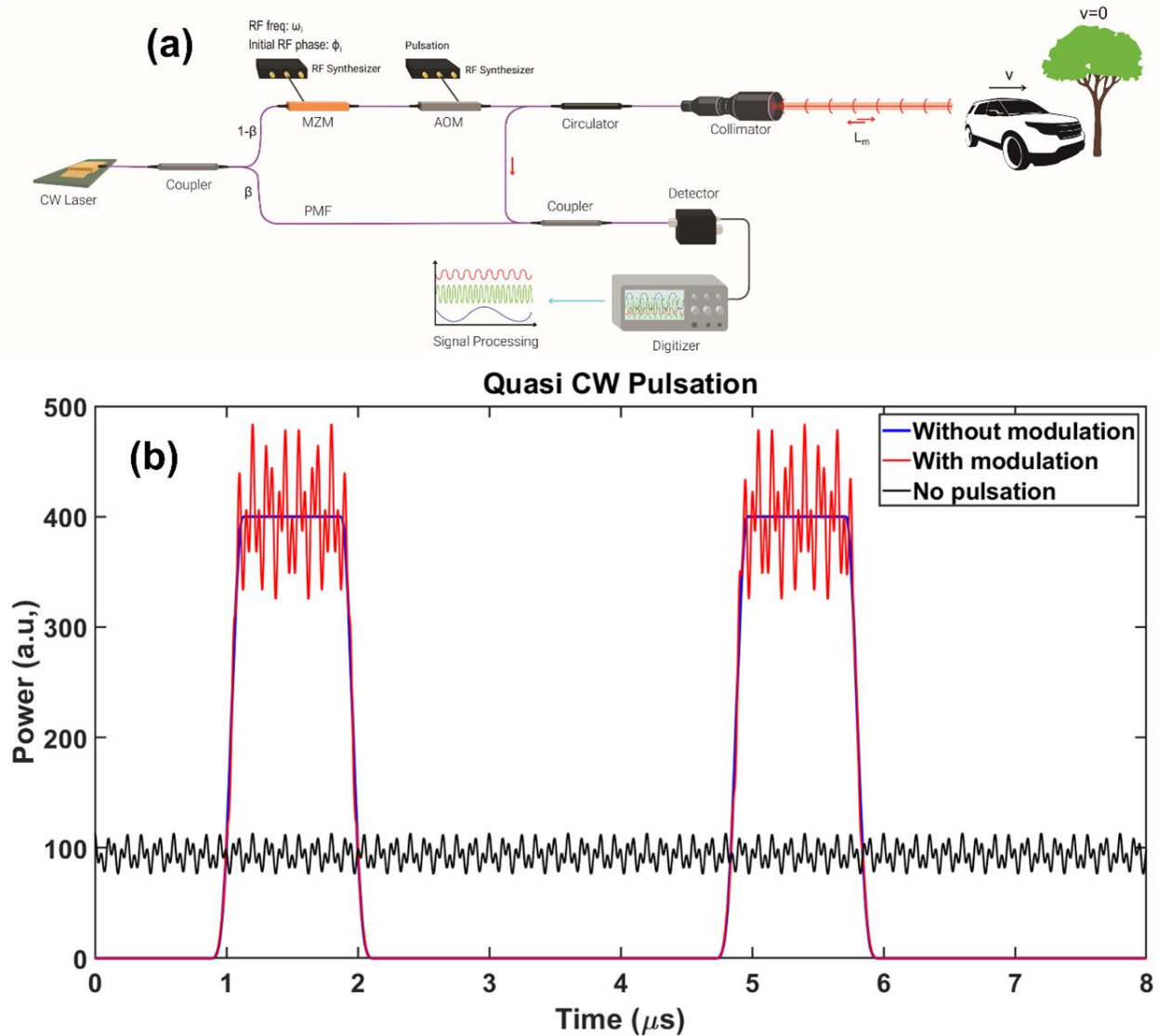


Fig. 33 | Concept of multi-tone quasi-CW pulsation. (a) Proposed PB-MTCW configuration to realize multi-tone modulated quasi-CW pulses. (b) Realization of quasi-CW pulsation with two-tone RF modulation. The blue curve represents the quasi-CW pulse without any modulation on it. The red curve indicates the quasi-CW pulsation with multi-tone CW modulation on it. The black curve represents the CW equivalent of the pulse with the same energy.

The quasi-CW pulsation of the multi-tone modulated light in the PB-MTCW architecture can be realized by introducing an additional modulator with a high extinction ratio such as an acousto-optic modulator (AOM) to the system. The suggested modification in the PB-MTCW architecture is presented in Fig. 33(a). The predefined pulse profile with the engineered repetition rate and the duty cycle can be fed through the RF-port of AOM to achieve the modulated quasi-CW multi-tone pulse. AOMs can also be useful to compensate part of static Doppler shifts due to the motion of the lidar system.

A numerical simulation is performed to show the quasi-CW pulsation as in Fig. 33(b). Here, two arbitrary RF modulation frequencies at 8MHz and 20MHz are fed to the electro-optic modulator to realize the multi-tone signal. The black curve indicates the CW multi-tone signal without pulsation. Here, the pulse duration is selected as $1\mu\text{s}$ and the repetition rate is set to be $\sim 250\text{kHz}$, which yields a duty cycle of $\sim 25\%$. These arbitrary parameters are selected for visualization purposes only. In Fig. 33(b) the red and blue curves indicate the pulse with and without the multi-tone modulation, respectively, which have the same amount of energy as the multi-tone CW signal (black curve).

5.5.2. Experimental setup

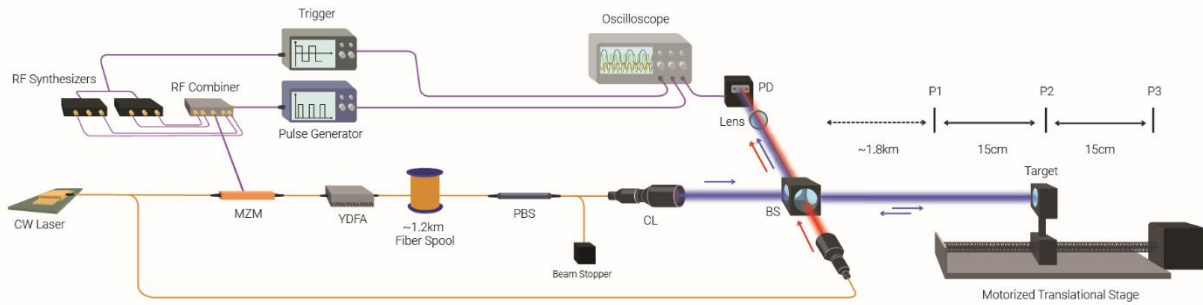


Fig. 34 | Experimental setup for testing the quasi-CW PB-MTCW lidar for long-range applications. The modulated CW beam is combined with a quasi-CW pulsation via RF combiner and MZM. A 1.2km fiber spool is added to the architecture to increase the target range to km level.

To test the capability of the PB-MTCW for long-range applications, a pulsation is integrated through the MZM along with the modulation frequencies. The experimental setup is presented in Fig. 34. A 20% duty cycle pulse with a $200\mu\text{s}$ period is generated via a pulse generator. A portion of the pulse is fed to a channel of the digital storage oscilloscope. The pulse is combined with 130, 510, 710, and 950MHz RF

tones that yield an unambiguous range of ~30m for the total propagation distance of the light. All the RF sources and the measurement oscilloscope is triggered by a 5kHz function generator. To have a strong peak power, the modulated beam is further amplified via a homemade ytterbium-doped fiber amplifier. Before going to the free space with a collimator, a ~1.2km long fiber spool (HI-1060) is introduced to mimic the long-range, which yields a coarse distance of ~1800m based on the refractive index of the fiber. Since there is the fiber, instead of checking the round trip distance, the total propagation distance of the light is measured. The fiber spool is followed by a polarization beam splitter to prevent any polarization-related mismatches. Then the laser is carried to the free space via a collimator. The target is placed ~2m away from the detector and the target is moved by 15cm increments on the stage to have in total of 3 measurement locations.

5.5.3. Experimental results

10 measurements are performed at each location using the quasi-CW modulated pulse and to measure the actual position of the target a single pulse is used with a 4ns pulse duration. By employing the pulse time-of-flight technique the actual distance is measured as 1862.3m with a ± 48 cm error range based on the average of 10 consecutive measurements with the short duration pulses. The time information from the pulses is acquired by cross-correlating two pulses.

The measurement results are presented in Fig. 35, where the reference measurement pulses are shown in the time domain as in Fig. 35(a). The 15cm differential in the position corresponds to a 30cm total light propagation difference. Based on the measurement results, the average of 10 trials is 1862.72m, 1863.01m, and 1863.30m, respectively. The results are displayed in Fig. 35(b). As can be seen from the results, the increments are measured as ~30cm at a ~1860m distance. Therefore, the unambiguous range limit is exceeded using the quasi-CW approach. In addition, the standard deviation of the measurements is <3cm, which indicates the precision of the measurement technique.

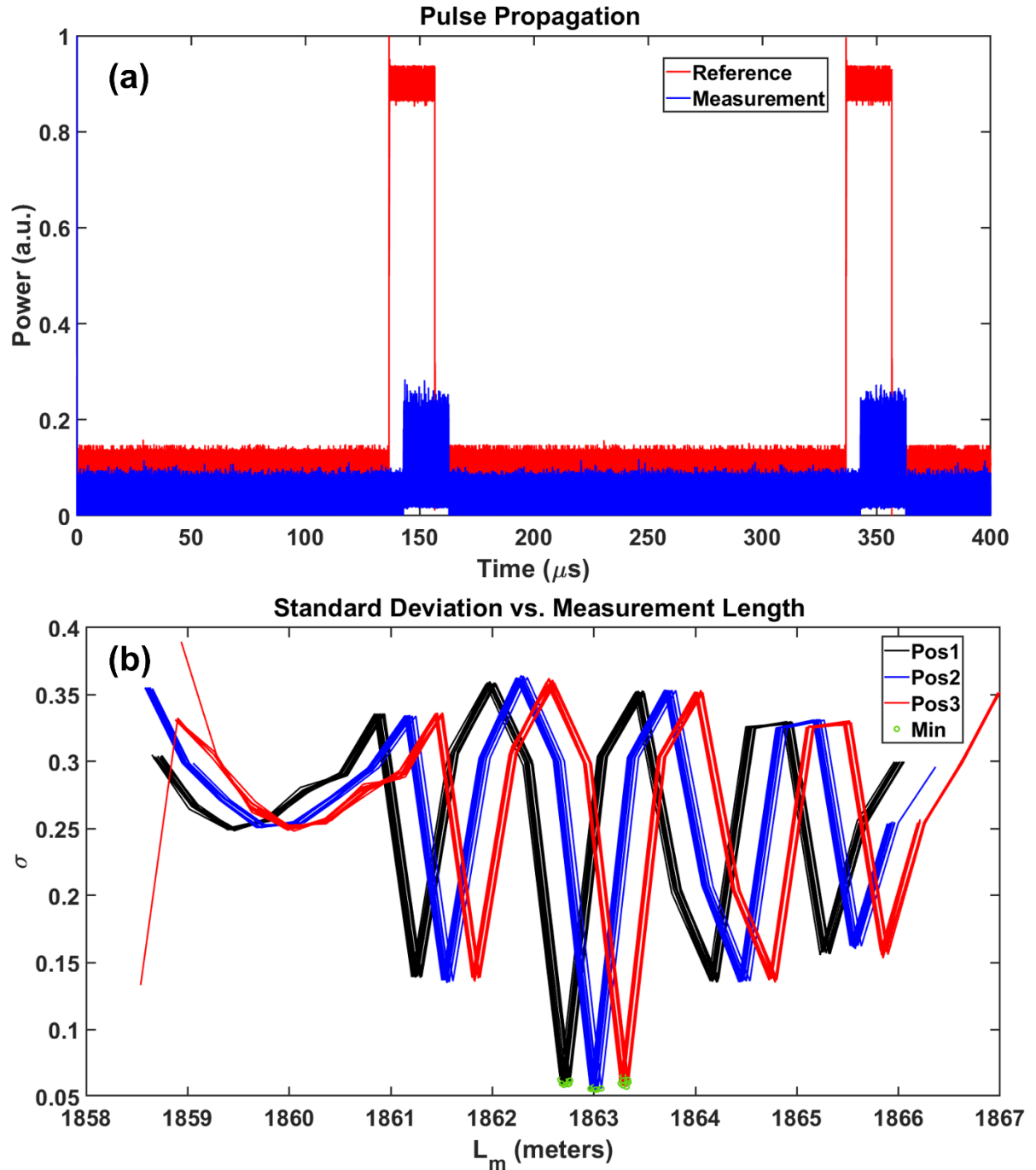


Fig. 35 | Experimental results for the long-range measurements with quasi-CW integration. (a) The quasi-CW measurement signal is acquired from the detector and the reference signal from the pulse generator. The time difference between two pulses generates the coarse range information. (b) The measurement results of the PB-MTCW technique after triangulation.

5.6. Analysis

5.6.1. Lidar parameters

Similar to the AB-MTCW and PE-MTCW lidar, the unambiguous range is related to the tone selection. However, it is important to distinguish between the repetition length of the minimum standard deviation point, L_{rep} , and the maximum ranging limit. If the PB-MTCW lidar is not integrated with the quasi-CW pulsation, then the maximum ranging limit and L_{rep} are identical, which also is the unambiguous range as indicated in Eq.(5.9). This value is determined by the greatest-common-divisor of the selected RF modulation frequencies. In the case of the experiment with CW operation, the ω_{gcd} is selected as 10MHz, which yields a ~15m unambiguous range. The division by 2 is due to the roundtrip of the light in the free space.

$$L_{unambiguous} = \frac{L_{rep}}{2} = \frac{2\pi c}{2\omega_{gcd}} \quad (5.9)$$

Nonetheless, as discussed in Section 5.5, introducing a quasi-CW pulsation along with the time gating of the pulses can enhance the PB-MTCW architecture to realize ranging beyond the unambiguous range. The coarse range information is provided by the time gating by yielding the value that n_i will span in the triangulation algorithm.

Moreover, the lidar techniques that employ coherent detection, i.e. FMCW lidar and AB-MTCW lidar, are limited by the coherence length of the laser in terms of the maximum detection range, L_{max} , as shown in Eq.(5.10). However, PB-MTCW lidar performs RF-mixing of the preselected tone frequencies that annihilates the common phase noise components. Therefore, it is possible to perform ranging beyond the coherence length of the CW laser utilized in the system [90].

$$L_{max} = \frac{L_{coh}}{2} = \frac{c}{2\pi\Delta f_0} \quad (5.10)$$

Considering the quasi-CW mode PB-MTCW lidar, it is possible to state that there is no hard limit for L_{max} in terms of unambiguous range or coherence length, while the system benefits from the coherent detection. On the other hand, the limit of the system can be analyzed via SNR analysis. If the collected

signal power is below the noise level of the architecture, the ranging will start to fail as in any kind of lidar system.

SNR in the PB-MTCW lidar can be formulated by considering several sources of noise in the system. Dominant noise sources are the detection electronics, sun noise, and booster-amplifier-related noises (if any). The SNR of the system is summarized as in Eq.(5.11) by assuming a balanced PIN photodetector. Here, R , P_{LO} , and P_{echo} represent the responsivity of the detector, optical local oscillator power, and optical signal power, respectively. In terms of detector noise, $\langle i_T^2 \rangle$ and $\langle i_{shot}^2 \rangle$ depict the thermal and shot noise, respectively. If there is a booster amplifier with an optical gain G that amplifies the echo signal (P_{echo}) after coupling with the local oscillator (P_{LO}), then one should also consider the amplified spontaneous emission (ASE) noise, as well. Hence, $\langle i_{sig-ase}^2 \rangle$ and $\langle i_{ase-ase}^2 \rangle$ indicate the noise caused by signal-ASE beating and ASE-ASE beating, respectively. Moreover, for outdoor operations during the daytime, there will be the impact of the solar background due to the emission spectra of the sun, especially for satellite-based lidar applications. The $\langle i_{sig-sun}^2 \rangle$ stands for the signal-sun noise beating, while the $\langle i_{sun-sun}^2 \rangle$ shows the sun-sun beating in the SNR calculation.

$$SNR = \frac{P_{signal}}{P_{noise}} = \frac{4R^2 G^2 P_{LO} P_{echo}}{\langle i_T^2 \rangle + \langle i_{shot}^2 \rangle + \langle i_{sig-ase}^2 \rangle + \langle i_{ase-ase}^2 \rangle + \langle i_{sig-sun}^2 \rangle + \langle i_{sun-sun}^2 \rangle} \quad (5.11)$$

The detector noises can be described as $\langle i_T^2 \rangle = 4(k_B T / R_L) \Delta f$ and $\langle i_{shot}^2 \rangle = 2qGRP_{LO} \Delta f$, where k_B is the Boltzmann constant, T the temperature, R_L is the load resistance, Δf the electronic bandwidth, and q the electron charge, respectively. Similarly, it is possible to formalize the ASE-related noises as $\langle i_{sig-ase}^2 \rangle = 4GR^2 P_{lo} S_{sp} \Delta f$ and $\langle i_{ase-ase}^2 \rangle = 4R^2 S_{sp}^2 \Delta f \Delta f_{opt}$, where Δf_{opt} is the optical bandwidth of the gain spectrum, and S_{sp} is the spectral density of spontaneous emission that can be formalized as $S_{sp} = (G - 1)\eta_{sp} h f_0$. In this equation, η_{sp} , h , and f_0 represent the spontaneous emission factor of the gain medium, Planck's constant, and central emission frequency of the amplifier, respectively. Finally, the sun-

related noise can be described as $\langle i_{sig-sun}^2 \rangle = 4G^2 R^2 P_{LO} S_{solar} \Delta f$ and $\langle i_{sun-sun}^2 \rangle = 4G^2 R^2 S_{solar}^2 \Delta f \Delta f_{opt}$, where S_{solar} is the spectral density of solar irradiation.

It is possible to reduce the impact of the solar background by utilizing proper filtering to reduce the optical bandwidth. Depending on the signal level, level of amplification, and selected local oscillator power, two noise terms that can be dominating are $\langle i_{shot}^2 \rangle$ and $\langle i_{sig-ase}^2 \rangle$. In most cases, it is more beneficial to increase the P_{LO} instead of increasing G to reduce the ASE impact, which can be significantly large for ultra-low P_{echo} . Therefore, by increasing P_{LO} the dominating term becomes the shot noise and the SNR can be simplified as in Eq.(5.12) with a constant depending on system parameters, K , and with the ratio of the echo-signal power and electronic bandwidth.

$$SNR \sim \frac{4R^2 G^2 P_{LO} P_{echo}}{2qRGP_{LO} \Delta f} = \frac{2RGP_{echo}}{q\Delta f} = K \frac{P_{echo}}{\Delta f} \quad (5.12)$$

Hence, in such a heterodyne system, the SNR will be dependent on the electronic bandwidth and the signal power. Since the information on each modulation frequency is needed, it is possible to filter out the modulation frequencies via narrow bandpass filters digitally or in the analog domain to reduce the impact of noise. The use of narrowband static tones allows us to utilize narrowband filters so that the SNR per tone can increase to yield more accurate ranging results. Numerical simulation results of the SNR with different Δf per tone are presented in Fig. 36. Here, the $P_{LO} = 5\text{mW}$, initial $P_{echo} = 10\text{mW}$, $T = 300\text{K}$, and the solar spectrum is assumed to be centered at $1\mu\text{m}$ with a $\pm 1\text{nm}$ bandwidth filter. A small 3dB gain is assumed to minimize the ASE noise contribution to SNR. The echo signal power is attenuated as much as 120dB and the computed SNR results for 1MHz, 10MHz, and 100MHz bandwidth filters around each tone are presented. As can be realized from the figure, tuning the bandwidth of the bandpass filter can significantly increase the SNR for each modulation frequency.

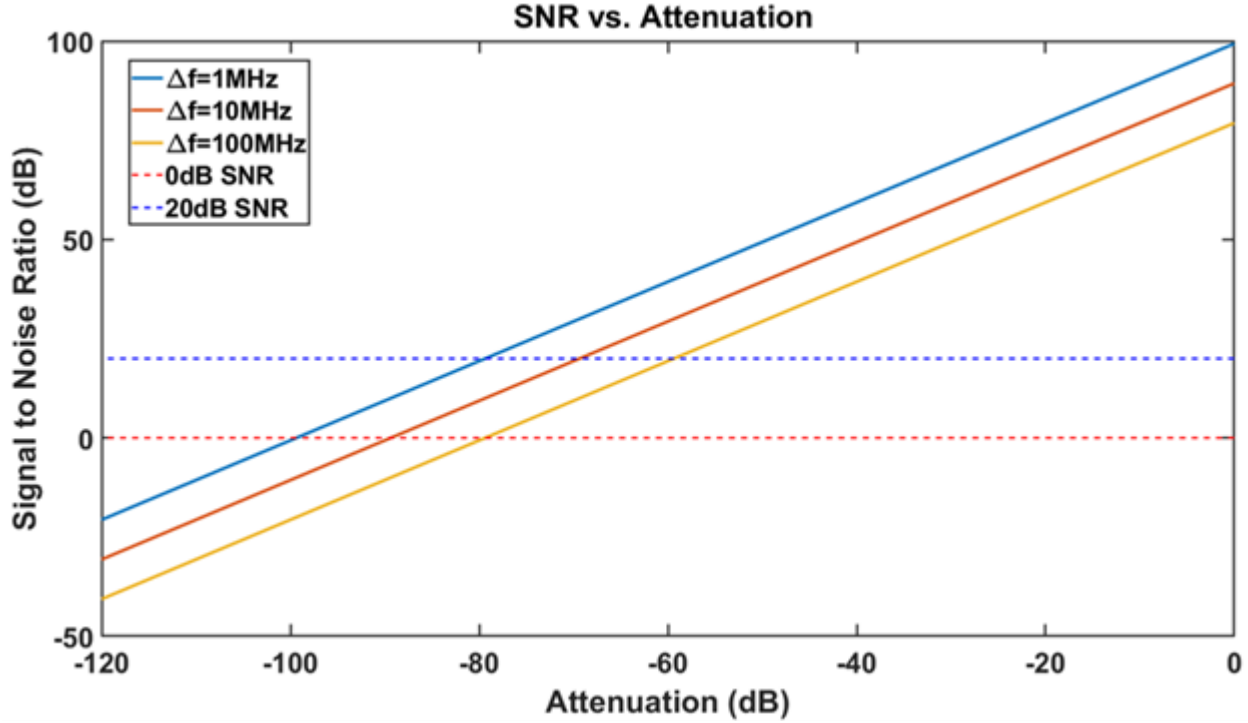


Fig. 36 | Numerical simulation results of the signal-to-noise ratio of a single modulation frequency with respect to the echo signal attenuation. The red dashed line indicates the 0 dB SNR (no signal) line and the blue dashed line shows the 20dB SNR level. The SNR results for 1MHz, 10MHz, and 100MHz filter around each modulation frequency is represented with blue, orange, and yellow solid lines, respectively.

On the other hand, the ranging resolution, δL , achievable by an individual tone is defined by the minimum distinguishable phase of the i^{th} tone, $d\phi_i$, as in Eq.(5.13) .

$$\delta L = \frac{d\phi_i}{\omega_i} c = c \times dt \quad (5.13)$$

Here, $d\phi_i$ depends on various parameters such as sampling rate, jitter, total noises in the system, surface roughness under the spot size, etc. Nonetheless, it is possible to formalize the minimum theoretical resolution by considering a noise-free case, where $d\phi_i = \omega_i \times dt$, and hence $\delta L = c \times dt$, where dt is the time resolution. In the case of the experiment, after digitally interpolating the data, the final dt becomes $\sim 24\text{ps}$, while it was 200ps before interpolation. Based on $\delta L = c \times dt$, the theoretical minimum resolution is calculated as 0.72cm .

In terms of precision, the resultant standard deviations for each set of measurement data for CW PB-MTCW are $<1\text{cm}$, also the quasi-CW PB-MTCW yields $<3\text{cm}$ standard deviation. Furthermore, the accuracy of the measurement can be verified via the value of the minimum σ_k after the triangulation algorithm. As can be seen in Fig. 31, Fig. 32, and Fig. 35 all the acquired minimum σ_k after triangulation are <0.1 and close to the ideal value of 0. Hence, this can be used as a metric to indicate the accuracy of the PB-MTCW lidar.

5.6.2. Challenges

The PB-MTCW lidar addresses the challenges that were previously discussed for AB-MTCW and PE-MTCW lidars, which include power balance requirements, limitations due to Doppler shifts, unambiguous range, and coherence length limits. The main constraint of the PB-MTCW lidar is due to the usage of the RF tones. The RF tones should be phase-locked by exploiting phase-locked loop (PLL) circuits by the RF synthesizers. Moreover, the initial phases of each RF modulation can yield results with a deviation from the true value. Therefore, the initial phase of each tone should be set to zero at the input port of the MZM. Similarly, the optical fiber path length should be known by the system to extract the actual value. To solve these issues, a pre-calibration can be performed as in the experiment by measuring the distance at the output facet of the MZM or collimator based on the lidar architecture. The calibration will generate the pseudo measurement distance right before the light is brought to the free space. Hence the deviation from the true value will be mitigated via the calibration.

Another critical factor is the selection of the RF tones. It is desired to have a spurious-free dynamic range for finer identification of the received modulation tones. In addition, increasing the number of modulation tones will enhance the system by eliminating potential local minimums during the triangulation of the target position as shown in Fig. 27. Therefore, the tones should be carefully selected by inhibiting potential overlaps due to cross beatings and second harmonics. The available bandwidth should be carefully engineered by utilizing high and low frequencies together. Similarly, tone separations should be wider than two times the expected Doppler shifts, to prevent the overlap of Doppler-shifted frequencies due to the speed of a dynamic target.

SUMMARY AND DISCUSSION

The purpose of establishing the Multi-Tone Continuous-Wave lidar technology is to create an alternative to the existing lidar technologies, which eliminates the need for phase, frequency, or amplitude sweeping and generates high resolution ranging and velocimetry measurements. To do so, first, the AB-MTCW methodology is constructed. In this technique, a CW laser is modulated via multiple RF tones, and a portion of the modulated beam is kept as the local oscillator. The phase accumulations on the echo signal are realized as amplitude variations on the preselected RF tones. A sine fitting algorithm is used as post-processing to generate the target distance, while the slight Doppler shifts in the RF spectrum yield the target speed. Furthermore, to improve the capability of the AB-MTCW lidar for high-speed targets, a phase triangulation approach is integrated into the AB-MTCW technique, which is called the PE-MTCW approach. In this technique, the phases of Doppler-shifted frequencies are measured and triangulation is performed via post-processing to measure the target's range. Finally, a phase-based ranging and velocimetry approach is established by employing coherent detection with an unmodulated local oscillator. In the PB-MTCW lidar, phases of each modulation frequency or the Doppler-shifted frequencies are utilized with the triangulation algorithm to compute the range of the object.

For AB-MTCW lidar, the theoretical model of simultaneous ranging and velocimetry is developed. The system is demonstrated in the experimental domain by utilizing a motorized translational stage and a target mirror under stationary and dynamic conditions. Application of the AB-MTCW method via sine fitting yields the range information, while the Doppler shift generates the speed of the target with the RF tone beatings. The AB-MTCW ranging results are in satisfactory correlation with the PToF measurements for stationary targets based on the R^2 analysis that yields an average deviation of $\sim 0.75\text{cm}$ which corresponds to the PToF ranging resolution. Simultaneous velocimetry produces precise results within $\pm 0.8\text{cm/s}$ speed resolution. The ranging accuracy is SNR-dependent, while the resolution of the velocimetry is governed by the time window and sampling rate. The results of the numerical simulation were presented to show the impact of noise over the detected RF tones. A minimum of -60dBm received signal power is essential to

resolve the detected tone powers. Similarly, a power balance between two branches up to 20dB is required to realize the amplitude variations over the static RF tones. Moreover, the linewidth of the CW laser will indicate the coherence length of the propagating beam. To realize coherent detection via interferometry, the linewidth should be selected according to the desired measurement range. In addition, the unambiguous range is defined by the greatest-common-divisor of the selected modulation frequencies.

In the case of PE-MTCW lidar, the enhancement of the AB-MTCW lidar system to perform simultaneous ranging and velocimetry of moving targets is theoretically developed and demonstrated via numerical analysis and experimental results. For a numerical verification and explanation of the concept, a dummy target is assumed with 108km/h speed and 50m distance during the simulations. The target velocity is measured by evaluating the side peaks near the frequency tones. The acquired Doppler shift corresponds to the target's speed. Then by using the phase and measurement length relation at the individual frequency-shifted tones, the potential values are determined. A triangulation algorithm is built and used to extract the range of a target by utilizing the possible solutions of L_m at each frequency. The resolution of the velocimetry depends on the frequency resolution of the spectrum, while the ranging accuracy is defined by the temporal resolution of detection electronics. In the presented simulations, the velocimetry and ranging resolution are found to be $\pm 0.4\text{cm/s}$ and $\pm 1\text{cm}$, respectively. Furthermore, the proposed concept is demonstrated in the experimental domain by using a dynamic target placed in a motorized translational stage. The target is measured to be at 111.9cm with 8.08cm/s speed by using the triangulation algorithm.

Finally, the PB-MTCW lidar enables simultaneous ranging and velocimetry beyond the coherence length of the CW laser. This new approach has the potential to overcome maximum-range limitations for coherent systems, particularly for long-range applications such as satellite-based systems or surface mapping with airborne lidars for oceanography and forestry. Here, the working principle of PB-MTCW lidar is described as well as the corresponding post-processing approach to extract the valuable ranging and velocimetry information. The stationary target ranging results are demonstrated using a high coherence laser with less than 100kHz linewidth and a low coherence laser with 5.3GHz linewidth, which corresponds to coherence lengths of more than 1km and about 1.8cm, respectively. The measurement variations were

found to be $<1\text{cm}$ for both experiments. Finally, the dynamic target velocimetry and ranging are demonstrated with a target moving at a maximum speed of 11cm/s . It is observed that the same methodology is applicable for moving targets even with a low coherence laser. A potential implementation of the proposed PB-MTCW lidar to long-range measurements, such as airborne lidar or satellite-based measurements, can utilize so-called quasi-CW lasers (pulsed lasers with very broad pulse width). Since the peak power of pulses will be much larger than its multi-tone modulated CW counterpart, it will generate a higher signal-to-noise ratio. Also, the time of flight measurement of such pulses can be used for coarse range measurements, and hence supports the triangulation algorithm. The quasi-CW integrated PB-MTCW lidar ranging results for long-range operations are demonstrated for a target that is placed $\sim 1850\text{m}$ away from the lidar by using a 1km fiber spool. The measurement precision for the quasi-CW approach is measured as $<3\text{cm}$. As a result, the quasi-CW approach combines the advantages of PToF lidars and CW lidars without using any frequency, phase, or amplitude scanning and provides precise measurements at ranges far beyond the coherence length of the laser. Overall, when the long-range operation, high point cloud density requirements, and narrow time window conditions are considered the PB-MTCW technique is a potential candidate that can satisfy these requirements, whether it is a ground-based application or an airborne lidar system.

BIBLIOGRAPHY

1. C. Urmson, J. Anhalt, D. Bagnell, C. Baker, R. Bittner, M. Clark, J. Dolan, D. Duggins, T. Galatali, and C. Geyer, "Autonomous driving in urban environments: Boss and the urban challenge," *Journal of Field Robotics* **25**, 425–466 (2008).
2. J. Hecht, "Lidar for self-driving cars," *Optics and Photonics News* **29**, 26–33 (2018).
3. L. Wallace, A. Lucieer, C. Watson, and D. Turner, "Development of a UAV-LiDAR system with application to forest inventory," *Remote Sensing* **4**, 1519–1543 (2012).
4. J. L. Bufton, J. B. Garvin, J. F. Cavanaugh, L. A. Ramos-Izquierdo, T. D. Clem, and W. B. Krabill, "Airborne lidar for profiling of surface topography," *Optical Engineering* **30**, 72–79 (1991).
5. B. L. Stann, W. C. Ruff, and Z. G. Sztankay, "Intensity-modulated diode laser radar using frequency-modulation/continuous-wave ranging techniques," *Optical Engineering* **35**, 3270–3279 (1996).
6. A. Ansmann, U. Wandinger, M. Riebesell, C. Weitkamp, and W. Michaelis, "Independent measurement of extinction and backscatter profiles in cirrus clouds by using a combined Raman elastic-backscatter lidar," *Applied Optics*, **31**, 7113–7131 (1992).
7. A. Braun, C. Y. Chien, S. Coe, and G. Mourou, "Long range, high resolution laser radar," *Optics Communications* **105**, 63–66 (1994).
8. A. Ansmann and D. Müller, "Lidar and Atmospheric Aerosol Particles," in *Lidar: Range-Resolved Optical Remote Sensing of the Atmosphere*, C. Weitkamp, ed., Springer Series in Optical Sciences (Springer New York, 2005), pp. 105–141.
9. R.-E. Mamouri and A. Ansmann, "Potential of polarization/Raman lidar to separate fine dust, coarse dust, maritime, and anthropogenic aerosol profiles," *Atmospheric Measurement Techniques* **10**, 3403–3427 (2017).
10. P. P. Sullivan, C.-H. Moeng, B. Stevens, D. H. Lenschow, and S. D. Mayor, "Structure of the Entrainment Zone Capping the Convective Atmospheric Boundary Layer," *Journal of the Atmospheric Science* **55**, 3042–3064 (1998).
11. J. Quan, Y. Gao, Q. Zhang, X. Tie, J. Cao, S. Han, J. Meng, P. Chen, and D. Zhao, "Evolution of planetary boundary layer under different weather conditions, and its impact on aerosol concentrations," *Particuology* **11**, 34–40 (2013).
12. T. Luettel, M. Himmelsbach, and H. Wuensche, "Autonomous Ground Vehicles—Concepts and a Path to the Future," *Proceedings of the IEEE* **100**, 1831–1839 (2012).
13. M. Himmelsbach, A. Müller, T. Luettel, and H. J. Wuensche, "LIDAR-based 3D Object Perception," in *Proceedings of 1st International Workshop on Cognition for Technical Systems* (2008).
14. S. Ramasamy, R. Sabatini, A. Gardi, and J. Liu, "LIDAR obstacle warning and avoidance system for unmanned aerial vehicle sense-and-avoid," *Aerospace Science and Technology* **55**, 344–358 (2016).
15. K. Kidono, T. Miyasaka, A. Watanabe, T. Naito, and J. Miura, "Pedestrian recognition using high-definition LIDAR," in *2011 IEEE Intelligent Vehicles Symposium (IV)* (2011), pp. 405–410.
16. R. Aufrere, J. Gowdy, C. Mertz, C. Thorpe, C. C. Wang, and T. Yata, "Perception for collision avoidance and autonomous driving," *Mechatronics* **13**, 1149–1161 (2003).
17. P. Y. Shinzato, D. F. Wolf, and C. Stiller, "Road terrain detection: Avoiding common obstacle detection assumptions using sensor fusion," in *2014 IEEE Intelligent Vehicles Symposium Proceedings* (2014), pp. 687–692.
18. Y. Jiang, S. Karpf, and B. Jalali, "Time-stretch LiDAR as a spectrally scanned time-of-flight ranging camera," *Nature Photonics* **14**, 14–18 (2020).
19. B. Behroozpour, P. A. Sandborn, M. C. Wu, and B. E. Boser, "Lidar system architectures and circuits," *IEEE Communications Magazine* **55**, 135–142 (2017).
20. D. J. Lum, S. H. Knarr, and J. C. Howell, "Frequency-modulated continuous-wave LiDAR compressive depth-mapping," *Optics Express* **26**, 15420–15435 (2018).

21. C. V. Poulton, A. Yaacobi, D. B. Cole, M. J. Byrd, M. Raval, D. Vermeulen, and M. R. Watts, "Coherent solid-state LIDAR with silicon photonic optical phased arrays," *Optics Letters* **42**, 4091–4094 (2017).
22. E. W. Mitchell, M. S. Hoehler, F. R. Giorgetta, T. Hayden, G. B. Rieker, N. R. Newbury, and E. Baumann, "Coherent laser ranging for precision imaging through flames," *Optica* **5**, 988–995 (2018).
23. K. Rainey, S. Gilbertson, D. Kalb, and T. Beery, "Modulation based ranging for direct displacement measurements of a dynamic surface," *Optics Express* **29**, 21174–21189 (2021).
24. R. D. Peters, O. P. Lay, S. Dubovitsky, J. P. Burger, and M. Jeganathan, "MSTAR: an absolute metrology sensor with sub-micron accuracy for space-based applications," *Proceedings of SPIE Vol. 10568*, 105682O (2004).
25. Z. Chen, R. Fan, X. Li, Z. Dong, Z. Zhou, G. Ye, and D. Chen, "Accuracy improvement of imaging lidar based on time-correlated single-photon counting using three laser beams," *Optics Communications* **429**, 175–179 (2018).
26. J. P. Godbaz, M. J. Cree, A. A. Dorrington, and A. D. Payne, "A fast Maximum Likelihood method for improving AMCW lidar precision using waveform shape," in *2009 IEEE SENSORS* (2009), pp. 735–738.
27. J. P. Godbaz, M. J. Cree, and A. A. Dorrington, "Understanding and Ameliorating Non-Linear Phase and Amplitude Responses in AMCW Lidar," *Remote Sensing* **4**, 21–42 (2011).
28. M.-C. Amann, T. M. Bosch, M. Lescure, R. A. Myllylae, and M. Rioux, "Laser ranging: a critical review of unusual techniques for distance measurement," *Optical Engineering* **40**, 10–20 (2001).
29. P. F. McManamon, *Field Guide to Lidar* (SPIE Press, Bellingham, WA, 2015).
30. R. Whyte, L. Streeter, M. J. Cree, and A. A. Dorrington, "Application of lidar techniques to time-of-flight range imaging," *Applied Optics*, **54**, 9654–9664 (2015).
31. A. D. Payne, A. A. Dorrington, M. J. Cree, and D. A. Carnegie, "Improved measurement linearity and precision for AMCW time-of-flight range imaging cameras," *Applied Optics* **49**, 4392–4403 (2010).
32. A. A. Dorrington, M. J. Cree, A. D. Payne, R. M. Conroy, and D. A. Carnegie, "Achieving sub-millimetre precision with a solid-state full-field heterodyning range imaging camera," *Measurement Science and Technology* **18**, 2809 (2007).
33. E. Yoshikawa and T. Ushio, "Wind ranging and velocimetry with low peak power and long-duration modulated laser," *Optics Express*, **25**, 8845–8859 (2017).
34. P. Feneyrou, L. Leviandier, J. Minet, G. Pillet, A. Martin, D. Dolfi, J.-P. Schlotterbeck, P. Rondeau, X. Lacondemine, A. Rieu, and T. Midavaine, "Frequency-modulated multifunction lidar for anemometry, range finding, and velocimetry-2. Experimental results," *Applied Optics* **56**, 9676–9685 (2017).
35. T. Hariyama, P. A. M. Sandborn, M. Watanabe, and M. C. Wu, "High-accuracy range-sensing system based on FMCW using low-cost VCSEL," *Optics Express* **26**, 9285–9297 (2018).
36. P. A. M. Sandborn, N. Kaneda, Y.-K. Chen, and M. C. Wu, "Dual-Sideband Linear FMCW Lidar with Homodyne Detection for Application in 3D Imaging," in *Conference on Lasers and Electro-Optics (2016), Paper STu4H.8* (Optical Society of America, 2016), p. STu4H.8.
37. P. A. M. Sandborn, T. Hariyama, and M.-C. Wu, "Resolution-Enhancement for Wide-Range Non-Linear FMCW Lidar using Quasi-Synchronous Resampling," in *Imaging and Applied Optics 2017 (3D, AIO, COSI, IS, MATH, PcAOP) (2017), Paper DW3F.3* (Optical Society of America, 2017), p. DW3F.3.
38. T. Kim, P. Bhargava, and V. Stojanovic, "Optimal Spectral Estimation and System Trade-Off in Long-Distance Frequency-Modulated Continuous-Wave Lidar," in *2018 IEEE International Conference on Acoustics, Speech and Signal Processing (ICASSP)* (2018), pp. 1583–1587.
39. T. W. D. Bosq and B. L. Preece, "Frequency modulated continuous wave lidar performance model for target detection," in *Infrared Imaging Systems: Design, Analysis, Modeling, and Testing XXVIII* (International Society for Optics and Photonics, 2017), Vol. 10178, p. 101780T.

40. O. Batet, F. Dios, A. Comeron, and R. Agishev, "Intensity-modulated linear-frequency-modulated continuous-wave lidar for distributed media: fundamentals of technique," *Applied Optics*, **49**, 3369–3379 (2010).
41. P. Trocha, M. Karpov, D. Ganin, M. H. P. Pfeiffer, A. Kordts, S. Wolf, J. Krockenberger, P. Marin-Palomo, C. Weimann, S. Randel, W. Freude, T. J. Kippenberg, and C. Koos, "Ultrafast optical ranging using microresonator soliton frequency combs," *Science* **359**, 887–891 (2018).
42. M. Gupta, A. Velten, S. K. Nayar, and E. Breitbach, "What are optimal coding functions for time-of-flight imaging?," *ACM Transactions on Graphics* **37**, 13 (2018).
43. F. Li, J. Yablon, A. Velten, M. Gupta, and O. Cossairt, "High-depth-resolution range imaging with multiple-wavelength superheterodyne interferometry using 1550-nm lasers," *Applied Optics* **56**, H51–H56 (2017).
44. R. Dändliker, R. Thalmann, and D. Prongué, "Two-wavelength laser interferometry using superheterodyne detection," *Optics Letters* **13**, 339–341 (1988).
45. C. S. Bamji, P. O'Connor, T. Elkhatib, S. Mehta, B. Thompson, L. A. Prather, D. Snow, O. C. Akkaya, A. Daniel, and A. D. Payne, "A 0.13 μm CMOS system-on-chip for a 512×424 time-of-flight image sensor with multi-frequency photo-demodulation up to 130 MHz and 2 GS/s ADC," *IEEE Journal of Solid-State Circuits* **50**, 303–319 (2014).
46. R. D. Peters, O. P. Lay, S. Dubovitsky, J. Burger, and M. Jeganathan, "Design considerations and validation of the MSTAR absolute metrology system," in *Interferometry XII: Techniques and Analysis* (International Society for Optics and Photonics, 2004), Vol. 5531, pp. 32–44.
47. R. Torun, M. M. Bayer, I. U. Zaman, J. E. Velazco, and O. Boyraz, "Realization of Multitone Continuous Wave Lidar," *IEEE Photonics Journal* **11**, 1–10 (2019).
48. R. Torun, M. M. Bayer, I. U. Zaman, and O. Boyraz, "Multi-tone modulated continuous-wave lidar," in (International Society for Optics and Photonics, 2019), Vol. 10925, p. 109250V.
49. O. Boyraz, M. M. Bayer, R. Torun, and I. Zaman, "TuD2.2 - Multi Tone Continuous Wave Lidar (Invited)," in *2019 IEEE Photonics Society Summer Topical Meeting Series (SUM)* (2019), pp. 1–2.
50. M. M. Bayer, R. Torun, I. U. Zaman, and O. Boyraz, "A Basic Approach for Speed Profiling of Alternating Targets with Photonic Doppler Velocimetry," in *Conference on Lasers and Electro-Optics*, OSA Technical Digest (Optical Society of America, 2019), p. AW4K.4.
51. P. F. McManamon, *LiDAR Technologies and Systems* (SPIE Press, Bellingham, WA, 2019).
52. M. Harris, G. Pearson, J. Vaughan, D. Letalick, and C. Karlsson, "The role of laser coherence length in continuous-wave coherent laser radar," *Journal of Modern Optics* **45**, 1567–1581 (1998).
53. P. A. M. Sandborn, *FMCW Lidar: Scaling to the Chip-Level and Improving Phase-Noise-Limited Performance* (University of California, Berkeley, 2017).
54. C. Yu, M. Shangguan, H. Xia, J. Zhang, X. Dou, and J.-W. Pan, "Fully integrated free-running InGaAs/InP single-photon detector for accurate lidar applications," *Optics Express* **25**, 14611–14620 (2017).
55. G. E. Stillman, V. M. Robbins, and N. Tabatabaie, "III-V compound semiconductor devices: Optical detectors," *IEEE Transactions on Electron Devices* **31**, 1643–1655 (1984).
56. P. Adany, C. Allen, and R. Hui, "Chirped lidar using simplified homodyne detection," *Journal of Lightwave Technology* **27**, 3351–3357 (2009).
57. R. Neuville, J. S. Bates, and F. Jonard, "Estimating forest structure from UAV-mounted LiDAR point cloud using machine learning," *Remote Sensing* **13**, 352 (2021).
58. NASA. 2022. Visible Light | Science Mission Directorate. [online] Available at: <https://science.nasa.gov/ems/09_visiblelight> [Accessed 15 June 2022].
59. Y. Li and J. Ibanez-Guzman, "Lidar for autonomous driving: The principles, challenges, and trends for automotive lidar and perception systems," *IEEE Signal Processing Magazine* **37**, 50–61 (2020).
60. R. H. Couch, C. W. Rowland, K. S. Ellis, M. P. Blythe, C. R. Regan, M. R. Koch, C. W. Antill, W. L. Kitchen, J. W. Cox, and J. F. DeLorme, "Lidar In-Space Technology Experiment (LITE): NASA's first in-space lidar system for atmospheric research," *Optical Engineering* **30**, 88–96 (1991).

61. NASA. 2022. Lidar In-space Technology Experiment (LITE), [online] Available at: <https://www.nasa.gov/centers/langley/news/factsheets/LITE.html> [Accessed 18 June 2022].
62. J. Liu, Q. Sun, Z. Fan, and Y. Jia, "TOF Lidar development in autonomous vehicle," in (IEEE, 2018), pp. 185–190.
63. Velodyne Lidar. 2022. What is lidar? Learn How Lidar Works," Velodyne Lidar, [online] Available at: <https://velodynelidar.com/what-is-lidar/#:~:text=Lidar%20sensors%20are%20a%20key,changing%20surroundings%20for%20safe%20navigation> [Accessed 20 June 2022].
64. K. Yoshioka, "A Tutorial and Review of Automobile Direct ToF LiDAR SoCs: Evolution of Next-Generation LiDARs," IEICE Transactions on Electronics 2021CTI0002 (2022).
65. R. Paschotta. 2002. Coherence, [online] Available at: <https://www.rp-photonics.com/coherence.html>. [Accessed 13 June 2022].
66. J. Riemensberger, A. Lukashchuk, M. Karpov, W. Weng, E. Lucas, J. Liu, and T. J. Kippenberg, "Massively parallel coherent laser ranging using a soliton microcomb," Nature **581**, 164–170 (2020).
67. R. D. Peters, O. P. Lay, S. Dubovitsky, J. Burger, and M. Jeganathan, "Design considerations and validation of the MSTAR absolute metrology system," in *Interferometry XII: Techniques and Analysis* (International Society for Optics and Photonics, 2004), Vol. 5531, pp. 32–44.
68. D. H. Dolan, "Accuracy and precision in photonic Doppler velocimetry," Review of Scientific Instruments **81**, 053905 (2010).
69. M. A. Itzler, M. Entwistle, S. Wilton, I. Kudryashov, J. Kotelnikov, X. Jiang, B. Piccione, M. Owens, and S. Rangwala, "Geiger-Mode LiDAR: from airborne platforms to driverless cars," in (Optical Society of America, 2017), pp. ATu3A-3.
70. R. Myllylä, J. Marszalec, J. Kostamovaara, A. Mäntyniemi, and G.-J. Ulbrich, "Imaging distance measurements using TOF lidar," Journal of optics **29**, 188 (1998).
71. Velodyne Lidar. 2022. Ultra Puck Surround View Lidar Sensor, [online] Available at: <https://velodynelidar.com/products/ultra-puck/> [Accessed 20 June 2022].
72. G. P. Agrawal, *Fiber-Optic Communication Systems*, 3rd ed. (John Wiley & Sons, 2012), Vol. 222.
73. W. He, B. Sima, Y. Chen, H. Dai, Q. Chen, and G. Gu, "A correction method for range walk error in photon counting 3D imaging LIDAR," Optics Communications **308**, 211–217 (2013).
74. L. Ye, G. Gu, W. He, H. Dai, and Q. Chen, "A real-time restraint method for range walk error in 3-D imaging lidar via dual detection," IEEE Photonics Journal **10**, 1–9 (2018).
75. S. A. Gudmundsson, H. Aanæs, and R. Larsen, "Environmental effects on measurement uncertainties of time-of-flight cameras," in *International Symposium on Signals, Circuits and Systems* (IEEE, 2007), Vol. 1, pp. 1–4.
76. B. Haylock, M. Baker, T. Stace, and M. Lobino, "Fast electro-optic switching for coherent laser ranging and velocimetry," Applied Physics Letters **115**, 181103 (2019).
77. J. M. Payne, D. Parker, and R. Bradley, "Rangefinder with fast multiple range capability," Review of Scientific Instruments **63**, 3311–3316 (1992).
78. X. Zhang, J. Pouls, and M. C. Wu, "Laser frequency sweep linearization by iterative learning pre-distortion for FMCW LiDAR," Optics Express **27**, 9965–9974 (2019).
79. T. Hariyama, P. A. Sandborn, M. Watanabe, and M. C. Wu, "High-accuracy range-sensing system based on FMCW using low-cost VCSEL," Optics Express **26**, 9285–9297 (2018).
80. M. M. Bayer, R. Torun, X. Li, J. E. Velazco, and O. Boyraz, "Simultaneous ranging and velocimetry with multi-tone continuous wave lidar," Optics Express **28**, 17241–17252 (2020).
81. M. M. Bayer and O. Boyraz, "Ranging and velocimetry measurements by phase-based MTCW lidar," Optics Express **29**, 13552–13562 (2021).
82. M. M. Bayer and O. Boyraz, "Multi-tone continuous wave detection and ranging," US patent US20210382164A1 (Dec. 9, 2021).
83. M. M. Bayer, R. Torun, I. U. Zaman, and O. Boyraz, "Multi-Tone Continuous Wave Lidar in Simultaneous Ranging and Velocimetry," in *Conference on Lasers and Electro-Optics* (Optical Society of America, 2020), pp. SM1O-6.

84. O. T. Strand, D. R. Goosman, C. Martinez, T. L. Whitworth, and W. W. Kuhlow, "Compact system for high-speed velocimetry using heterodyne techniques," *Review of Scientific Instruments* **77**, 083108 (2006).
85. C. Li, X. Cao, K. Wu, G. Qiu, M. Cai, G. Zhang, X. Li, and J. Chen, "Blind zone-suppressed hybrid beam steering for solid-state Lidar," *Photonics Research* **9**, 1871–1880 (2021).
86. Thorlabs. 2022. DET08C 5 GHz InGaAs Free-Space Photodetector with Window, 800 - 1700 nm, 8-32," [online]. Available at: <https://www.thorlabs.com/thorproduct.cfm?partnumber=DET08C#ad-image-0>. [Accessed 25 June 2022].
87. Q. Chen, "Airborne lidar data processing and information extraction," *Photogrammetric Engineering and Remote Sensing* **73**, 109 (2007).
88. M. M. Bayer, G. N. Guentchev, X. Li, J. E. Velazco, and O. Boyraz, "Enhancing the multi-tone continuous-wave lidar with phase detection," in (International Society for Optics and Photonics, 2021), Vol. 11828, p. 1182807.
89. Z. Xu, L. Tang, H. Zhang, and S. Pan, "Simultaneous real-time ranging and velocimetry via a dual-sideband chirped lidar," *IEEE Photonics Technology Letters* **29**, 2254–2257 (2017).
90. M. M. Bayer, X. Li, G. N. Guentchev, R. Torun, J. E. Velazco, and O. Boyraz, "Single-shot ranging and velocimetry with a CW lidar far beyond the coherence length of the CW laser," *Optics Express* **29**, 42343–42354 (2021).
91. A. Dieckmann, "FMCW-LIDAR with tunable twin-guide laser diode," *Electronics Letters* **30**, 308–309 (1994).
92. F. Gustafsson, "Determining the initial states in forward-backward filtering," *IEEE Transactions on signal processing* **44**, 988–992 (1996).